Upscaling Elastic Parameters on Complex Geometry Grids

Andreas B Lindblad

Problem description

Seismic inversion plays a critical role in quantitative usage of seismic data for improved hydrocarbon recovery. Seismic data in itself carries limited information until it is combined with additional sources of data. The most prominent data type in this respect is acoustic well measurements. As inverted seismic data provides a description of the reservoir's properties, it should ideally be able to distinguish quality sand from poor.

The aim of the project is to demonstrate how elastic upscaling can be used to differentiate reservoir facies, accounting for the 3D geometry of the reservoir rock. A key topic for the project is presenting the homogenization problem for elastic properties in the static limit. In particular, understanding the elastic tensor and how rotation affects both pressure and shear wave velocities is necessary. Moreover, Statoil will provide rock models and software for numerical homogenization with periodic boundary conditions. This will allow one to make a comparison between inverted seismic data and computed, homogenized data.

Assignment given: January 14, 2013

Supervisor: Egil Tjåland, IPT

Co-Supervisor: Alf Birger Rustad, Statoil

Co-Supervisor: Olivier Lopez, Statoil

Abstract

Statoil and collaborating partners have recently been able to develop a general upscaling technique that takes into account the complex geology and geometry of rocks. Accordingly, it has now become possible to predict accurate and valid reservoir properties at the seismic scale. The main objective of this study was to utilize the latter opportunity to determine whether inverted seismic data is capable of capturing information on the 3D geometry of reservoir rocks. In principle, this will give an indication of the inverted seismic data's ability to differentiate facies. A secondary goal was to examine the anisotropy at the seismic scale. The largest part of the thesis, however, aimed to give a general description on how to predict seismic properties.

In order to achieve the above targets, a set of facies models seeking to represent channel belts in an actual reservoir were adopted. Although the cells in each model were associated with upscaled lithofacies, they did not contain elastic properties. Consequently, an extensive survey devoted to finding representative elastic input was carried out. Several different ways of providing cell data were considered, but eventually the choice fell on using a combination of empirically generated properties and well-measurements. Before the completed models could be upscaled, the general method had to be verified. To do this, various test models with distinct characteristics were upscaled, and their results evaluated. As the accuracy proved to be satisfying, the upscaling technique was assumed both functional and trustworthy. With that clarified, the models were finally upscaled to provide predictive and representative channel belt properties at the seismic scale. The degree of expected seismic anisotropy could then be assessed on the basis of the upscaled elastic properties' directionality. To find out whether inverted seismic data contains geometrical rock information, the predicted channel belt properties were compared with corresponding measured ones.

From the upscaling results, it was found that the anisotropy is expected to be weak, but nevertheless considerable at the seismic scale. Additionally, the conformity between estimated and inverted channel belt properties turned out to be great. The latter strongly suggests that inverted seismic data in fact are able to register geometrical information on reservoir rocks, and that this information can be predicted using elastic upscaling.

Abstrakt

Statoil, med samarbeidspartnere, har nylig utviklet en generell oppskaleringsmetode som er i stand til å ta hensyn til bergarters komplekse geologi og geometri. På den måten har det nå blitt mulig å estimere gyldige og nøyaktige reservoaregenskaper på seismisk skala. Hovedmålet til dette studiet var derfor å utnytte den sistnevnte muligheten til å avgjøre om invertert seismikk er i stand til å fange opp informasjon om 3D-geometrien til reservoarbergarter. I prinsippet vil dette kunne gi en pekepinn på evnen invertert seismikk har til å skille facies. Et annet delmål var å undersøke anisotropien på seismisk skala. Den største delen av oppgaven tok derimot sikte på å gi en generell beskrivelse av hvordan man faktisk skal estimere seismiske egenskaper.

For å oppnå disse målene ble en mengde facies-modeller, som alle forsøker å forestille kanalbelter i et virkelig reservoar, tatt i bruk. Selv om cellene til hver modell allerede var knyttet til oppskalerte litofacies, så hadde de ikke blitt tildelt elastiske egenskaper. En omfattende undersøkelse ble derfor gjennomført for å finne representativ, elastisk input. Flere ulike alternativer ble vurdert, men til slutt falt valget på å bruke en kombinasjon av empirisk genererte egenskaper og brønnmålinger. Før de ferdigstilte modellene kunne bli oppskalert måtte den generelle metoden valideres. Dette ble gjort ved at ulike testmodeller med forskjellig særpreg ble oppskalert, og deres resultater evaluert. Ettersom nøyaktigheten til metoden viste seg å være tilfredsstillende, ble den formodet å være både funksjonell og pålitelig. Med dette avklart, kunne modellene endelig bli oppskalert for å fremskaffe forutsigende og representative kanalbelteegenskaper på seismisk skala. Graden av forventet seismisk anisotropi ble så vurdert på grunnlag av retningsavhengigheten til de oppskalerte, elastiske egenskapene. For å finne ut om invertert seismikk faktisk inneholder informasjon om bergartsgeometri, ble de estimerte kanalbelteegenskapene sammenlignet med tilsvarende *målte* egenskaper.

Resultatene fra oppskaleringen viste at anisotropien er forventet å være svak, men likevel betydningsfull, på seismisk skala. I tillegg var overensstemmelsen stor mellom estimerte og inverterte kanalbelteegenskaper. Mye tyder derfor på at invertert seismikk faktisk er i stand til å registrere geometrisk informasjon om reservoarbergarter, og at denne informasjonen kan spås ved hjelp av elastisk oppskalering.

Preface

This thesis concludes my Master's degree in geophysics. It was written during the spring of 2013 at the Department of Petroleum Engineering and Applied Geophysics, Norwegian University of Science and Technology. The work was done in collaboration with Statoil Research Center, Trondheim.

Since the subject of this thesis has (to my knowledge) previously not been addressed, it was hard to tell exactly what was going to be the outcome of the research. Accordingly, the workflow was made up along the way. The thesis will probably show signs of this in some places. The main topic of the study was proposed to me by Alf Birger Rustad (Statoil) during a summer internship in 2012.

First of all I would like to thank my supervisor at the department, Egil Tjåland, for both his time and guidance, keeping the work on the right track. Huge thanks should also go to Olivier Lopez at Statoil. He has truly been a great mentor, and has helped me solving practical and theoretical problems from day one. In addition, my co-supervisor Alf Birger Rustad should get a lot of credit for his splendid advising and aid. Finally, I want to mention Kari Børset (Statoil), who has provided excellent explanations and assistance whenever it has been needed. I am also grateful to everyone else at Statoil Research Center, Trondheim who has answered questions and provided help in any other way.

Trondheim, June 2013   Andreas Baldishol Lindblad

Contents

Chapter 1

Introduction

In order to enhance recovery of hydrocarbons in a producing reservoir, it is very often crucial to locate and fetch residual pockets of oil and gas. Accordingly, one should, if possible, exploit information from every source that provides insight into the quality and the properties of the reservoir target. When dealing with tertiary recovery, the amount of data on hand is vast. In most cases, a large number of seismic surveys, well logs, laboratory measurements and geological interpretations is made accessible through months and years of production. Consequently, at this stage, there is plenty of information that can be stitched together to improve our understanding of the reservoir. Seismic inversion [3], with its quality and capacity, plays a leading role in the latter process. The objective of this method is to turn reflection data into quantitative measures of rock and fluid properties by integrating seismology and borehole-related knowledge. Since seismic surveys provide the only approved way of mapping the subsurface without actually drilling, lots of time, money and resources are spent to make them as valuable as possible. It is hence of key interest to utilize their full potentials. Although seismic data is capable of outlining major geological structures, and can be examined and interpreted alone, it often constitutes images of the subsurface with low quality. If one disregards the noise, this is mainly caused by two factors. First and foremost, the resolution of the seismic data is low both vertically and horizontally due to frequency band-limitations. Secondly, the seismic data provides little knowledge about the characteristics of the rocks, as it maps layer *interface* properties, not layer properties. By calibrating the seismic signal with well log data (seismic inversion), the frequency band is extended and the imaged ground saturated with properties like velocity, density and porosity. As a result, the description of the reservoir is left more intuitive and detailed, making it easier to interpret.

Since the ultimate goal is to locate volumes of oil present in the reservoir, the inverted seismic data set should ideally be able to differentiate facies in all spatial directions. Principally, this would allow one to accurately point out regions associated with high quality sand. For the latter to be realized, however, the inverted seismic data must be capable of capturing the three-dimensional geometry of the reservoir rocks. Up until now, it has not been possible to demonstrate that this actually is true, due to the for-

mer lack of adequate tools. Consequently, there might be very useful information still hidden in the inverted seismic data. To try to unlock these additional details about the geology, predictive facies modeling and elastic upscaling is employed in this thesis. The main idea is to generate reliable models of the reservoir facies and compare their properties with the corresponding ones found in the inverted seismic data. However, before one can do this legitimately, each model's elastic behavior has to be upscaled. Upscaling is basically the process of transferring information from a smaller to a larger scale, utilizing homogenization techniques [8]. As the wavelengths in seismic surveys are long, the inverted seismic data will only be able to detect effective facies properties, and not minor features. Geological information incorporated in the models must hence be passed on to the seismic scale in order for the comparison to be meaningful. Earlier, the upscaling were performed using so-called volume weighted averages. The problem with these is that they all have a limited ability to handle complex geology and geometry. To resolve this, Statoil and collaborating partners have recently developed a more general method for upscaling, which correctly takes into consideration the geometry and the anisotropy of the mediums. Accordingly, it is now possible for the first time to predict the effects three-dimensional geometry in reservoir rocks have on seismic data. As long as the models are representative, one should be able to establish whether inverted seismic data actually contains information on 3D geometry or not, by directly comparing predicted and measured facies properties. If the correspondence between the two is large, the various reservoir facies are likely to be separable on inverted seismic data. The latter comparison can naturally also be used as a tool to validate facies models.

In addition, there is another aspect of seismic inversion that has to be improved. Presently, seismic inversion methods are incapable of handling directionality in elastic properties. Since seismic data is given in vertical time or depth to form a natural view of the ground, the data used to calibrate it must be given in vertical time or depth too in order for the integration to be valid. Consequently, all deviated wells are excluded from the seismic inversion process. Owing to the fact that most wells are somehow deviated, this must be regarded as major weakness. Now that the general upscaling method allows one to responsibly bring geological information to the seismic domain, it will be possible to predict the degree of anisotropy at the seismic scale. In principle, this will enable us to tell how much elastic properties are supposed to vary with the angle of measurement. If the seismic anisotropy is significant, logs belonging to deviated wells have to be corrected before they can be used in seismic inversion. If not, deviated well data can be incorporated as is. A secondary target of the current study is hence to address the anticipated directionality of seismic properties, so that one can get an idea on what to do with deviated wells. This is simply carried out by evaluating the upscaling results of realistic facies models.

The validity of the reservoir facies' predicted elastic properties depends only on two things - the reliability of the facies models, and the accuracy of the upscaling method. Consequently, the main focus of this report is geared towards making sure that the mod-

els and the method actually are applicable. Since the general upscaling code is fairly new, it has to be properly tested and analyzed before it safely can be employed. This is thoroughly done in chapter 5. Different models with different characteristics are upscaled, and their results evaluated based on either analytical solutions [7] or restricting bounds [9]. The latter two is provided by traditional homogenization theories that are presented in chapter 3, together with the newly developed upscaling method. The output from an upscaling is a single elastic tensor that describes the effective elastic behavior of the medium in question. As elastic tensors have 36 elements and up to 21 independent coefficients [2], they are very hard to interpret. Hence, to increase the comprehensibility of tensors, chapter 4 provides three ways of visualizing them. Because the size and number of models to upscale often are large in reservoir modeling, it would be nice to have a way of reducing the total upscaling duration when time is an issue. Chapter 6 shows how one can, if necessary, divide full reservoir models into smaller pieces to do this.

The various facies models examined in the current thesis attempt to describe channel belts that are believed to be present in an actual fluvial reservoir. To take into account the variations in channel belt geology and properties throughout the reservoir, there are 62 of them - each built on the basis of geological interpretations. In the spirit of keeping reservoir modeling consistent, the cells constituting the facies models correspond to homogenized lithofacies ones. Unfortunately, due to the former inability to accurately upscale elasticity, the cells lack elastic properties. As laboratory data is not available for the reservoir of interest, reliable model input has to be found elsewhere. Chapter 7 introduces three empirical velocity relations [16, 17, 18] that can be utilized. In order to examine their suitability and finally settle on realistic elastic input, synthetic velocity logs are generated and compared with sonic well measurements in chapter 9. Preferably, the elastic input should also be corrected for pore fluid properties [22, 23, 24]. However, since the models are not placed in depth in this thesis, a fluid substitution is meaningless. The formula for doing it is nevertheless discussed in chapter 8 for future reference. After populating the cells with elastic parameters, the various facies models are upscaled to provide predictive channel belt properties at the seismic scale. In chapter 10, these are inspected - also in terms of directionality. The comparison with inverted seismic data, on the other hand, is performed in chapter 11.

The scope of the project is confined to the problem of bringing predictive facies properties to the seismic scale, and determining whether inverted seismic data are able to capture information on the 3D geometry of reservoir rocks.

Chapter 2

Background theory

Since the current study is based on the same theory as the one carried out in [1], the content of this chapter is mainly extracted from the latter.

2.1 Seismology, borehole logs and rock physics

Reflection seismology is by far the most powerful tool we have available for visualizing geological structures in the subsurface. Short and simply told, the concept of reflection seismology involves emitting seismic waves into the ground, wait for them to reflect at geological interfaces, and record their arrivals at the surface with an array of receivers. This is possible due to the fact that waves both reflect and refract at locations where abrupt contrasts in acoustic impedance (=velocity·density) occur. During acquisition, the amplitude of the waves and the travel times are measured. Later, when a decent velocity model of the ground has been acquired through processing, the measured signals can be sorted and reflectors placed in time or depth to form crude images of the subsurface.

Acoustic well logs, also known as sonic logs, provide complementary information about the earth's properties, and are hence used to calibrate seismic data (e.g. in seismic inversion). The acoustic logs contain measurements on the time taken for elastic waves to propagate through formations. From this dataset, the velocities of elastic waves can be derived in depth. The logging itself, is done by a tool mounted on the drill string. A transmitter generates sharp pulses of sound, and after travelling through an interval of surrounding rock, a receiver records their arrivals as amplitudes occurring in time. The length between a transmitter and a receiver is typically half a meter, a meter, or some other number close to that. Energy created by the transmitter splits up into several waves, which propagate through the earth with different polarizations and velocities, due to elastic phenomena. In addition, an endless number of raypaths can be followed from the transmitter to the receiver. The recorded energy is consequently dispersed in time. By logging the first arrivals of the first and second wave, average pressure and shear wave velocities, respectively, is found for the rock interval. Both pressure and

shear wave velocities enter into seismic inversion. Since the first arrivals correspond to the shortest pathways, the velocities are measured parallel to the well and drilling direction. In most cases, rocks are anisotropic, meaning that their elastic properties vary with the angle of measurement. As wave velocities are determined by elastic parameters and density, they will too depend on a wave's propagation direction. In theory, deviated and vertical wells will therefore produce different acoustic logs, even though they penetrate the same material.

To be able to describe the behavior of waves emitted by seismic sources, the world is assumed continuous and elastic. Like all physical objects, rocks consist of atoms. The atoms form molecules, the molecules form minerals, the minerals form grains and the grains finally form rocks. At each scale, building blocks are separated by empty space. This means that earth in reality is discontinuous. However, at a macroscopic level, rocks and rock properties can be modeled as continuums and continuous functions, respectively. A continuum is medium where matter fills the entire region of occupied space. The rocks can hence be continuously divided into infinitesimal elements, each having properties equal to the bulk material. In the upcoming sections, the term "particle" corresponds to such an element. Owing to the assumption above, a seismic wave can be regarded as a continuous disturbance, distributed throughout the earth. In addition, one would like rocks to respond to external forces in a linear elastic way. This simply assumes small, non-permanent deformations, related linearly to force. The deformations generated by seismic sources are usually both small and temporal, so linear elasticity is assumed valid in seismic wave propagation.

In this thesis, and generally in geophysics, the words heterogeneity, homogeneity, isotropy and anisotropy appear frequently in discussions. Since these are all easily mixed qualities of a medium, short definitions are provided in the list below:

- A **homogeneous** material is uniform in structure or properties

- A **heterogeneous** material is non-uniform in structure or properties

- An **isotropic** material has identical properties in all direction

- An **anisotropic** material has properties depending on the angle of measurement

Hence, a medium is typically homogeneous isotropic, or some other combination of the two concepts. Isotropy is explained further in section 2.3.

2.2 Elasticity

A wave is a time-varying disturbance or oscillation that travels through space, due to a transfer of energy. The wave motion transfers energy from one point to another, disrupting the original equilibrium of the particles and dislocating them. This displacement, however, is usually not permanent. Instead the particles vibrate about almost fixed

positions, and will return after the wave has passed and no new energy is transmitted. The deformation reverses itself owing to internal restoring forces that emerge as the particles are displaced. It is these elastic restoring forces between particles, combined with inertia, which lead to vibration of the medium, allowing waves to propagate. To be able to formulate a mathematical description of the oscillations, the concepts of strain and stress, related to the deformations and restoring forces respectively, must be introduced. The following subsections will hopefully illuminate the two key concepts.

2.2.1 Strain

Travelling seismic waves apply forces to the medium in which they propagate. These forces will move the particles relative to each other, changing both volume and shape of the material. During strain all points in the medium are in general shifted. The displacement of one particular point is characterized by a displacement vector defined as

$$\boldsymbol{u} = \boldsymbol{r}' - \boldsymbol{r} \ , \tag{2.1}$$

where $\boldsymbol{r}$ and $\boldsymbol{r}'$ are the positions of a given point before and after displacement, respectively, with the first having components x_1, x_2, x_3 and the second having components x_1', x_2', x_3'. To get a true measure of deformation, only dilatation and distortion should be accounted for. Rigid rotation and translation will not enter into the dynamics of the vibration problem.

Whenever the material deforms, the distances between points change. Take for example two points infinitely close to each other. In component form the distance between the points before deformation is dx_i. After deformation it becomes

$$dx_i' = dx_i + du_i \ . \tag{2.2}$$

The vector length from one point to the other, before strain, is then

$$dl = \sqrt{dx_1^2 + dx_2^2 + dx_3^2} \tag{2.3}$$

and after strain

$$dl' = \sqrt{dx_1'^2 + dx_2'^2 + dx_3'^2} \ . \tag{2.4}$$

Substituting the expression for dx_i' (2.2) into equation (2.4) gives

$$dl'^2 = dl^2 + 2\frac{\partial u_i}{\partial x_j}dx_i dx_j + \frac{\partial u_i}{\partial x_j}\frac{\partial u_i}{\partial x_k}dx_j dx_k \ . \tag{2.5}$$

By changing the indices in (2.5), the expression for dl'^2 can be rearranged, and will fall out as

$$dl'^2 = dl^2 + 2e_{ij}dx_i dx_j \ , \tag{2.6}$$

where the strain tensor of second order, e_{ij}, is introduced:

$$e_{ij} = \frac{1}{2}\left(\frac{\partial u_i}{\partial x_j} + \frac{\partial u_j}{\partial x_i} + \frac{\partial u_k}{\partial x_i}\frac{\partial u_k}{\partial x_j}\right) . \tag{2.7}$$

Solids vary plenty in their deformability. Some materials have large elastic zones, while others have small. For most rigid materials the displacement gradient must be kept below the range of 10^{-4} to 10^{-3} [2], in order to avoid permanent deformation. By assuming very small displacement derivatives, the quadratic terms in (2.7) can be neglected. The strain tensor finally becomes

$$e_{ij} = \frac{1}{2}\left(\frac{\partial u_i}{\partial x_j} + \frac{\partial u_j}{\partial x_i}\right) , \tag{2.8}$$

or in matrix form:

$$\boldsymbol{e} = \begin{pmatrix} e_{xx} & e_{xy} & e_{xz} \\ e_{yx} & e_{yy} & e_{yz} \\ e_{zx} & e_{zy} & e_{zz} \end{pmatrix} .$$

The strain tensor, consisting of nine components, fully describes the deformation of the material. As one clearly sees from figure 2.1 and the above equation, strain is displacement per unit of length, and thus has no dimension. Due to the symmetry of the strain tensor ($e_{ij} = e_{ji} \; \forall \; i, j = x, y, z$), it turns out that only six independent strain components are sufficient in order to describe the deformation. The strain may therefore be written as a six-element vector. In abbreviated subscript notation it becomes

$$\boldsymbol{\epsilon} = \begin{pmatrix} e_{xx} \\ e_{yy} \\ e_{zz} \\ 2e_{yz} \\ 2e_{xz} \\ 2e_{xy} \end{pmatrix} = \begin{pmatrix} \epsilon_1 \\ \epsilon_2 \\ \epsilon_3 \\ \epsilon_4 \\ \epsilon_5 \\ \epsilon_6 \end{pmatrix} . \tag{2.9}$$

The factor 2 is introduced to simplify some of the key elastic equations, including (2.11).

2.2.2 Stress

Stress is simply the intensity of the internal forces acting between particles in a body across imaginary internal surfaces [4]. Elastic restoring forces, as mentioned, develop between neighboring particles during vibration. These forces act upon particle surfaces rather than volumes, and may thus be described as stresses or internal surface forces. Both have the denomination N/m^2.

The stress state of a point within a body can be represented by an infinitesimal cube with three stress components acting on each of the six sides, applied by the contiguous material. Owing to the fact that each point of the body is in static equilibrium, only
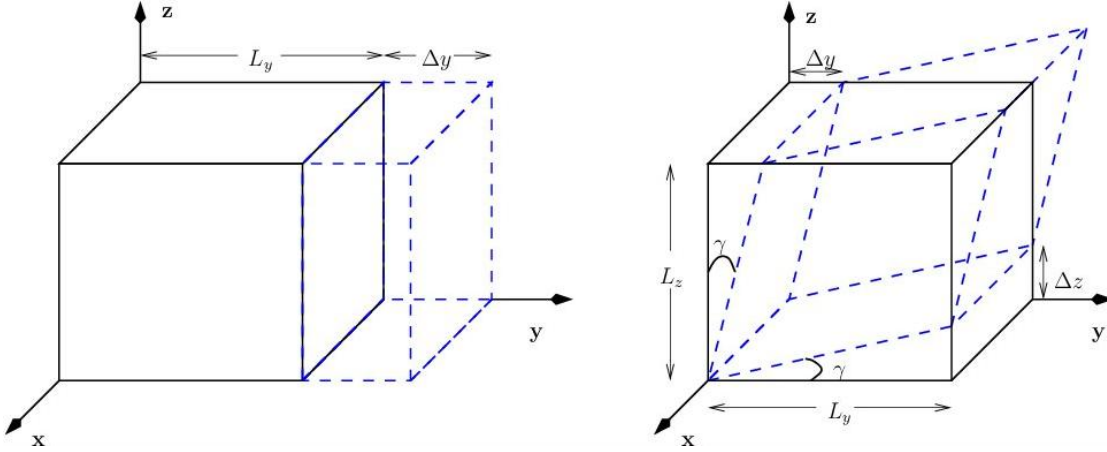
Figure 2.1: Normal strain (left) and shear strain (right). The strain component e_{yy} is given by $\frac{\Delta y}{L_y}$ and the strain component e_{yz} is given by $\frac{1}{2}\left(\frac{\Delta y}{L_z} + \frac{\Delta z}{L_y}\right)$.

nine stress components from three perpendicular planes are needed to describe the stress at each point. Of the nine components three are orthogonal normal stresses and six are orthogonal shear stresses. The different components can be seen in figure 2.2. The stress at a given point can hence be expressed by the matrix

$$\boldsymbol{\tau} = \begin{pmatrix} \tau_{xx} & \tau_{xy} & \tau_{xz} \\ \tau_{yx} & \tau_{yy} & \tau_{yz} \\ \tau_{zx} & \tau_{zy} & \tau_{zz} \end{pmatrix} ,$$

which is a second order tensor known as the stress tensor, or the stress matrix. According to the definition, τ_{ij} is the ith component of force density acting on the face perpendicular to the j-axis [2].

Since the medium of interest is stationary, and hence is in static equilibrium (no net momentum), also the stress tensor is symmetric,

$$\tau_{ij} = \tau_{ji} .$$

The symmetry will again minimize the number of independent components to six. A representation of stress in abbreviated subscript notation, and in vector form, yields

$$\boldsymbol{\sigma} = \begin{pmatrix} \tau_{xx} \\ \tau_{yy} \\ \tau_{zz} \\ \tau_{yz} \\ \tau_{xz} \\ \tau_{xy} \end{pmatrix} = \begin{pmatrix} \sigma_1 \\ \sigma_2 \\ \sigma_3 \\ \sigma_4 \\ \sigma_5 \\ \sigma_6 \end{pmatrix} . \tag{2.10}$$
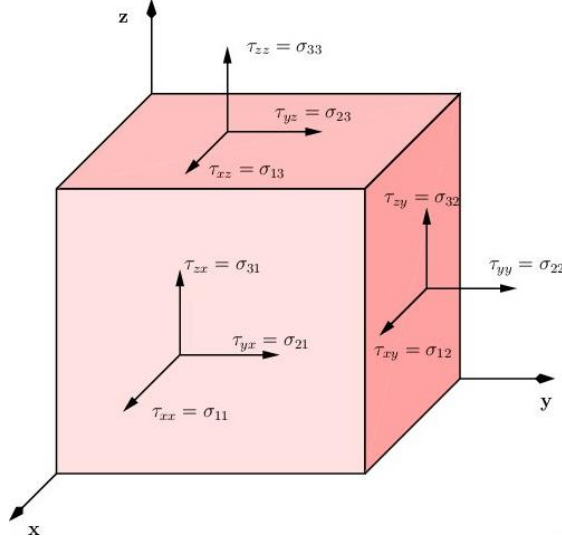
9

Figure 2.2: Stress components acting on an infinitesimal cube

2.2.3 Hooke's Law and the elastic modulus

In 1678, the British physicist Robert Hooke gave birth to elasticity theory by publishing "Ut tensio, sic vis," meaning "As the extension, so the force" [15]. His results, which relate tension and extension in elastic springs, are vitally important to understand and describe acoustic wave propagation. More generally, Hooke's Law (or the law of elasticity) states that the applied stress to a deformed body is linearly proportional to the strain, or vice versa. Mathematically, this can be expressed by writing each component of stress as a linear function of all the strain components. Take for example the normal stress component, τ_{xx}. It is related to the strain components by

$$
\begin{aligned}
\tau_{xx} = {} & c_{xxxx}e_{xx} & + \quad & c_{xxxy}e_{xy} & + \quad & c_{xxxz}e_{xz} \\
& + \quad c_{xxyx}e_{yx} & + \quad & c_{xxyy}e_{yy} & + \quad & c_{xxyz}e_{yz} \\
& + \quad c_{xxzx}e_{zx} & + \quad & c_{xxzy}e_{zy} & + \quad & c_{xxzz}e_{zz} \quad .
\end{aligned}
$$

In general, Hooke's law can be written as

$$ \boldsymbol{\tau} = \boldsymbol{C}\boldsymbol{e} \,, \tag{2.11} $$

or

$$ \tau_{ij} = c_{ijkl}e_{kl} \,. \tag{2.12} $$

where $\boldsymbol{\tau}$ and $\boldsymbol{e}$ are the familiar stress and strain tensors having components τ_{ij} and e_{kl} respectively, and $\boldsymbol{C}$ is the so-called stiffness tensor (or elastic modulus) having components c_{ijkl}. The notation used in (2.12) is called Einstein notation. According to this convention, whenever an index appears twice in a term, that term should be summed over all values of the index.

The elastic stiffness components can be seen as microscopic spring constants describing a system of tiny springs representing the elastic restoring forces within a body. Small values imply easily deformed materials, while large values imply rigid materials. It may be worth noticing that C contains information about the physical medium. Together with density, it will determine the speed of a travelling wave. Since both the stress and strain tensors are of second order, the stiffness tensor naturally becomes a fourth order tensor. Equation (2.11) implies that the stiffness coefficients must be measured in units N/m^2, owing to the fact that strain is dimensionless.

The relationship above gives an elastic modulus containing a total of 81 components. Luckily, not all are independent. Owing to symmetries in strain and stress, it can be shown that

$$c_{ijkl} = c_{jikl} = c_{ijlk} = c_{jilk} \ ,$$

giving 36 independent constants. A further reduction can be done using the symmetry

$$c_{ijkl} = c_{klij} \ ,$$

which is equivalent to assuming only positive wave velocities [8]. Consequently, in the most general and anisotropic case, the stiffness tensor contains 21 independent components. Usually the number is much less than this, due to material properties at the microscopic level.

To avoid difficulties associated with the application of Hooke's Law in full subscript notation, abbreviated subscripts are once again introduced. The resulting stiffness matrix becomes

$$C = \begin{pmatrix} c_{11} & c_{12} & c_{13} & c_{14} & c_{15} & c_{16} \\ c_{12} & c_{22} & c_{23} & c_{24} & c_{25} & c_{26} \\ c_{13} & c_{23} & c_{33} & c_{34} & c_{35} & c_{36} \\ c_{14} & c_{24} & c_{34} & c_{44} & c_{55} & c_{66} \\ c_{15} & c_{25} & c_{35} & c_{45} & c_{55} & c_{56} \\ c_{16} & c_{26} & c_{36} & c_{46} & c_{56} & c_{66} \end{pmatrix} \ ,$$

where

$$\begin{aligned} 1 &= xx \\ 2 &= yy \\ 3 &= zz \\ 4 &= yz, zy \\ 5 &= xz, zx \\ 6 &= xy, yx \ . \end{aligned}$$

11

Hence it follows that Hooke's Law can be expressed as the much more convenient matrix equation

$$
\begin{pmatrix} \sigma_1 \\ \sigma_2 \\ \sigma_3 \\ \sigma_4 \\ \sigma_5 \\ \sigma_6 \end{pmatrix} = \begin{pmatrix} c_{11} & c_{12} & c_{13} & c_{14} & c_{15} & c_{16} \\ c_{12} & c_{22} & c_{23} & c_{24} & c_{25} & c_{26} \\ c_{13} & c_{23} & c_{33} & c_{34} & c_{35} & c_{36} \\ c_{14} & c_{24} & c_{34} & c_{44} & c_{55} & c_{66} \\ c_{15} & c_{25} & c_{35} & c_{45} & c_{55} & c_{56} \\ c_{16} & c_{26} & c_{36} & c_{46} & c_{56} & c_{66} \end{pmatrix} \begin{pmatrix} \epsilon_1 \\ \epsilon_2 \\ \epsilon_3 \\ \epsilon_4 \\ \epsilon_5 \\ \epsilon_6 \end{pmatrix} , \tag{2.13}
$$

or in Einstein notation

$$
\sigma_i = c_{ij} \epsilon_j . \tag{2.14}
$$

2.3 Material symmetries

When materials have additional symmetries beyond the ones introduced in the previous section, the number of independent elastic components can progressively be brought down. The symmetry of a tensor is determined by the material's microscopic crystal structure. Table 2.1 gives an overview of possible symmetries/structures with the corresponding number of independent elastic constants. Since isotropic and transverse isotropic symmetries are of most interest in this paper, they will be further investigated in the next two subsection.

Symmetry	Independent components
Triclinic	21
Monoclinic	13
Orthorhombic	9
Tetragonal/Rhombohedral	6-7
Hexagonal/Transverse isotropy	5
Cubic	3
Isotropic	2

Table 2.1: Numbers of independent elastic components associated with various crystal symmetries.

2.3.1 Isotropy

In the most extreme case, having the absolute highest crystal symmetry, the number of independent components in C is reduced to only two. This kind of symmetry is called isotropy, and is reserved for materials with properties not depending on orientation. Through the years, many scientists have introduced their own parameters for describing isotropic materials. As an obvious result, there are today a lot of related parameters to choose from when an isotropic description of a medium is needed.

Among the most common and recognized parameters are Young's modulus, E, Lamé's

	(K,μ)	(λ,μ)	(E,ν)
λ	$K - \frac{2\mu}{3}$	λ	$\frac{E\nu}{(1+\nu)(1-2\nu)}$
μ	μ	μ	$\frac{E}{2+2\nu}$
K	K	$\lambda + \frac{2\mu}{3}$	$\frac{E}{3(1-2\nu)}$
E	$\frac{9K\mu}{3K+\mu}$	$\frac{\mu(3\lambda+2\mu)}{\lambda+\mu}$	E
ν	$\frac{3K-2\mu}{2(3K+\mu)}$	$\frac{\lambda}{2(\lambda+\mu)}$	ν

Table 2.2: Elastic parameters for isotropic materials

first parameter, λ, shear modulus (or Lamé's second parameter), μ, bulk modulus, K, and Poisson's ratio, ν. Their relationships to each other are given in table 2.2 [26]. By using the two Lamé parameters, λ and μ, the stiffness matrix simplifies to

$$
\boldsymbol{C} = \begin{pmatrix}
\lambda + 2\mu & \lambda & \lambda & 0 & 0 & 0 \\
\lambda & \lambda + 2\mu & \lambda & 0 & 0 & 0 \\
\lambda & \lambda & \lambda + 2\mu & 0 & 0 & 0 \\
0 & 0 & 0 & \mu & 0 & 0 \\
0 & 0 & 0 & 0 & \mu & 0 \\
0 & 0 & 0 & 0 & 0 & \mu
\end{pmatrix} .
$$

Naturally occurring isotropic materials are very hard to find at a microscopic level. However, since sedimentary rocks often are composed of anisotropic grains deposited in random orientation before diageneses, the different properties tend to average out, leading to isotropy at a larger scale. The isotropy assumption is therefore widely used by geophysicists dealing with sedimentary rocks (sandstones in particular) having some volume. Isotropy can also be applied for the sake of simplicity. Rarely does one have enough information to determine many of the elastic components. An elastic tensor estimated directly from well logs, for example, must have isotropic symmetry due to the fact that they only have enough information to determine two elastic parameters.

2.3.2 Transverse isotropy

The transverse isotropic symmetry, abbreviated TI, is another common symmetry well used in earth science. It applies to materials which are isotropic in planes perpendicular to a given axis of symmetry. This means that the physical properties in a particular direction only depend on the angle between the direction and the symmetry axis. A body made up by different layers of isotropic materials is therefore typically transverse isotropic. The elasticity of such a medium can be described by five independent con-

stants, a, b, c, d and e, which are put together to form the elastic modulus

$$C = \begin{pmatrix} a & a-2e & b & 0 & 0 & 0 \\ a-2e & a & b & 0 & 0 & 0 \\ b & b & c & 0 & 0 & 0 \\ 0 & 0 & 0 & d & 0 & 0 \\ 0 & 0 & 0 & 0 & d & 0 \\ 0 & 0 & 0 & 0 & 0 & e \end{pmatrix},$$

in the case of a symmetry axis parallel to the z-direction.

One of the key scientific laws in geology is the Principle of Original Horizontality, proposed by Nicholas Steno in 1669. This principle states that all layers of sedimentary rocks are originally deposited horizontally, or as Steno himself said it, "strata either perpendicular to the horizon or inclined toward it, were at one time parallel with the horizon" [5]. earth particles, created by weathering of old rocks, are transported by wind, water, ice and gravity to accumulation areas. The particles are deposited, and with time, pressure and heat, the particles eventually consolidate, building layers of sedimentary rock. It is the depositional environment, describing the physical, chemical and biological processes associated with the deposition, that determines the material composition and the thickness of layers. Through thousands and millions of years, these environments naturally change, and different rock types with different properties get stacked on top of each other. Today we know that Steno's principle is not true for all geological structures (for example dunes of sand), but it is still valid for most of the subsurface. Consequently, as blocks of sedimentary rock consist of close to isotropic layers aligned perpendicular to the vertical axis, they are frequently assumed transverse isotropic at large wavelengths.

At the microscopic level, shales are often assumed transverse isotropic due to their configuration. Shales basically consist of layers alternating between matter and air. Hence, they will have properties depending on the angle between the wave propagation direction and the direction normal to the orientation of the layers, making them TI symmetric.

2.4 Wave velocities

Combining three basic relations - the strain-displacement relation (2.8), relating strain and displacement, Hooke's Law (2.11), relating stress, strain and stiffness, and Newton's Law, relating displacement and stress - yields the elastic wave equation. Newton's Second Law of Motion can written as

$$\rho \frac{\partial^2 u_i}{\partial t^2} = \frac{\partial \tau_{ij}}{\partial x_j} + f_i \,, \tag{2.15}$$

where ρ is the density and f_i is the ith component of the external body force. By substituting Hooke's Law (2.12) into (2.15), and expressing strain in terms of displacement

$(e_{ij} = \frac{\partial u_i}{\partial x_j})$, one get the most general form of the elastodynamic equation

$$\rho \frac{\partial^2 u_i}{\partial t^2} = \frac{\partial}{\partial x_j}(c_{ijkl}\frac{\partial u_k}{\partial x_l}) + f_i \ . \tag{2.16}$$

In a region not directly affected by the source, the external force field, $\boldsymbol{f}$, is neglected. Moreover, if the medium of interest is homogeneous, where the density, ρ, and the elastic constants, c_{ijkl}, are all space-invariant, equation (2.16) reduces to

$$\rho \frac{\partial^2 u_i}{\partial t^2} = C_{ij}\frac{\partial^2 u_k}{\partial x_j \partial x_l} \ , \tag{2.17}$$

where $\boldsymbol{C}$ now is the abbreviated subscript version of the stiffness matrix [12]. For a plane wave propagating through anisotropic homogeneous material, the solution is found to be

$$\boldsymbol{u} = \boldsymbol{U}e^{-i(\omega t - k\boldsymbol{n}\boldsymbol{r})} \ \Leftrightarrow \ u_j = U_j e^{-i(\omega t - kn_j x_j)} \ . \tag{2.18}$$

Here $\boldsymbol{n}$ is a unit vector in the direction of propagation ($\boldsymbol{n} = n_x\hat{\boldsymbol{i}} + n_y\hat{\boldsymbol{j}} + n_z\hat{\boldsymbol{k}}$), ω is the angular frequency, k is the wave number and $\boldsymbol{U}$ is the polarization vector. Substituting (2.18) into (2.17), and taking the Fourier transform, one obtains

$$N_{ij}C_{jk}N_{kl}U_i = \rho(\frac{\omega}{k})^2 U_l \ ,$$

which may be rewritten to form the Christoffel equation [12],

$$(\Gamma_{ik} - \rho V^2 \delta_{ik})U_k = 0 \ , \tag{2.19}$$

where

$$\begin{aligned} \Gamma_{ik} &= N_{ij}C_{jk}N_{kl} \\ \boldsymbol{\Gamma} &= \boldsymbol{N}\boldsymbol{C}\boldsymbol{N}^T \end{aligned} \tag{2.20}$$

is the Christoffel matrix, δ_{ik} is the Kronecker delta and V is the phase velocity ($=\omega/k$). Abbreviated subscripts are again used on the stiffness tensor. For practical reasons, the matrix, $\boldsymbol{N}$, describing the propagation direction, has to be defined as

$$\boldsymbol{N} = \begin{pmatrix} n_x & 0 & 0 \\ 0 & n_y & 0 \\ 0 & 0 & n_z \\ 0 & n_z & n_y \\ n_z & 0 & n_x \\ n_y & n_x & 0 \end{pmatrix} = \frac{1}{k}\begin{pmatrix} k_x & 0 & 0 \\ 0 & k_y & 0 \\ 0 & 0 & k_z \\ 0 & k_z & k_y \\ k_z & 0 & k_x \\ k_y & k_x & 0 \end{pmatrix} \ .$$

From equation (2.19), one can clearly see that solving the Christoffel equation is equivalent to finding the eigenvalues and the eigenvectors of the Christoffel matrix. Knowing the direction of the travelling wave and the elastic modulus, the eigenvalues, ρV^2, and hence the velocities, V, can be found setting

$$det(\boldsymbol{\Gamma} - \rho V^2 \boldsymbol{I}) = 0 \ . \tag{2.21}$$

By solving the linear system of equations,

$$(\mathbf{\Gamma} - \rho V^2 \boldsymbol{I})\boldsymbol{U} = \boldsymbol{0} \;, \tag{2.22}$$

with the above eigenvalues, the eigenvectors, $\boldsymbol{U}$ is found. Each eigenvector describes the particle motion of a $\boldsymbol{n}$-directed wave, travelling with a velocity deduced from the corresponding eigenvalue. Since the Christoffel matrix is 3×3, and the number of eigenvalues is determined by the number of rows/columns in the matrix, there will be exactly three waves propagating along the direction $\boldsymbol{n}$ with different velocities. A closer look at (2.20) will in addition reveal the symmetry of the Christoffel matrix. Owing to this property, the eigenvectors must be reciprocally orthogonal. One polarization vector is parallel to the wave propagation direction and two are perpendicular. Waves that have the first type of polarization are called pressure waves, or P-waves, while waves that have one of the two latter are called shear waves, or S-waves. The two wave forms are illustrated in figure 2.3. S-waves can either be horizontally polarized or vertically polarized, and are named SH-waves and SV-waves respectively.

Solving the Christoffel equation for an **isotropic** medium yields P-wave and S-wave velocities

$$
\begin{aligned}
V_P &= \sqrt{\frac{\lambda + 2\mu}{\rho}} \\
V_S &= \sqrt{\frac{\mu}{\rho}} \; .
\end{aligned}
\tag{2.23}
$$

Since the medium has constant physical properties in all directions, the two S-waves must necessarily have the same speed (the particles vibrate just as "easy" in all directions normal to the propagation), and only two wave velocities are found. The velocities are of course also independent of propagation direction, and from (2.23) one can see that P-waves always move faster than the S-waves. The latter statement can be justified by the factor 2 in front of the shear modulus term in the P-wave velocity formula. Actually, the P in P-wave and S in S-wave refer to the sequence in which they arrive, and were originally shortenings for primary and secondary, respectively.
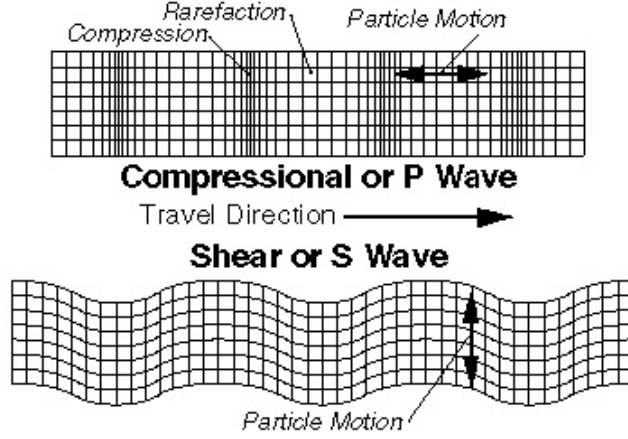
Figure 2.3: P-wave (upper) and S-wave (lower) propagation. Source: U.S. Geological Survey

The same equation solved for **transverse isotropic** materials gives

$$
\begin{aligned}
V_P(\theta) &= \frac{C_{11}sin^2(\theta) + C_{33}cos^2(\theta) + C_{44} + \sqrt{M(\theta)}}{2\rho} \\[2ex]
V_{SV}(\theta) &= \frac{C_{11}sin^2(\theta) + C_{33}cos^2(\theta) + C_{44} - \sqrt{M(\theta)}}{2\rho} \\[2ex]
V_{SH}(\theta) &= \frac{C_{66}sin^2(\theta) + C_{44}cos^2(\theta)}{\rho} \\[2ex]
M(\theta) &= \left[(C_{11}-C_{44})sin^2(\theta) - (C_{33}-C_{44})cos^2(\theta)\right]^2 \\
&\quad + (C_{13}+C_{44})sin^2(2\theta) \ ,
\end{aligned}
$$

(2.24)

where θ is the angle between the wave propagation direction and the symmetry axis.

2.5 Rotation of elastic tensors

In agreement with previous background theory, a transverse isotropic material, or a material with even lower symmetry, has an elastic modulus depending on basis orientation. It also has three velocities depending on the direction of the wave propagation. Owing to the fact that a change in a wave's travel direction is equivalent to a rotation of the medium itself while the propagation is kept constant, velocities at different angles can be found using orthogonal tensor rotation according to a change in coordinate axes. Consequently, if the elastic modulus is known for a volume of horizontally layered rock, the elastic modulus for the same volume, only tilted, can be found using coordinate transformation. In this thesis, however, tensor rotation is primarily put into practice to

check whether deviated well logs have to be corrected or not, in order for them to be allowed to participate in the seismic inversion routine.

Since coordinate transformations may seem a little tricky, a fairly thorough examination of the topic is given. Most of the theory and derivation comes from [2], where additional and helpful examples can be found.

Consider a vector, $\boldsymbol{v}$, having components v_x, v_y, v_z in the original basis, and the components v'_x, v'_y, v'_z in the new basis after rotation. The relative change in coordinate axes is then represented by direction cosines, a_{ij}, which make it possible to express the new components as functions of the old components and the angle of rotation. Both the direction cosines and the relationships between the new and old components are defined in figure 2.4. The formula for a general vector transformation is therefor

$$v'_i = a_{ij} v_j \; , \tag{2.25}$$

where $i, j = x, y, z$ and a_{ij} is an element of the transformation matrix $\boldsymbol{a}$, which for a clockwise rotation about the y-axis becomes

$$\boldsymbol{a} = \begin{pmatrix} \cos\left(\gamma\right) & 0 & \sin\left(\gamma\right) \\ 0 & 1 & 0 \\ -\sin\left(\gamma\right) & 0 & \cos\left(\gamma\right) \end{pmatrix} \; .$$

A transformation changes in reality only the way of describing a vector, not the length of it. As a consequence, it can be shown that $\boldsymbol{a}$ has the property

$$\begin{aligned} \boldsymbol{a}\boldsymbol{a}^{-1} &= \boldsymbol{I} \\ \Rightarrow \quad \boldsymbol{a}^{-1} &= \boldsymbol{a}^T \; , \end{aligned}$$

which states that an inverse transformation matrix is identical to a transposed one. All matrices that have this particular property are called orthogonal.

The product of a second order tensor, $\boldsymbol{\Psi}$, and a first order tensor (vector), $\boldsymbol{\omega}$, becomes a first order tensor (vector), $\boldsymbol{\alpha}$, expressed mathematically as

$$\boldsymbol{\alpha} = \boldsymbol{\Psi}\boldsymbol{\omega} \; . \tag{2.26}$$

Since equation (2.25) applies to all vectors, it obviously applies to $\boldsymbol{\omega}$ and $\boldsymbol{\alpha}$ too. The formula gives the relations

$$\begin{aligned} \boldsymbol{\omega}' &= \boldsymbol{a}\boldsymbol{\omega} \\ \Rightarrow \quad \boldsymbol{\omega} &= \boldsymbol{\omega}'\boldsymbol{a}^T \end{aligned} \tag{2.27}$$

and

$$\begin{aligned} \boldsymbol{\alpha}' &= \boldsymbol{a}\boldsymbol{\alpha} \\ \Rightarrow \quad \boldsymbol{\alpha} &= \boldsymbol{\alpha}'\boldsymbol{a}^T \end{aligned} \tag{2.28}$$
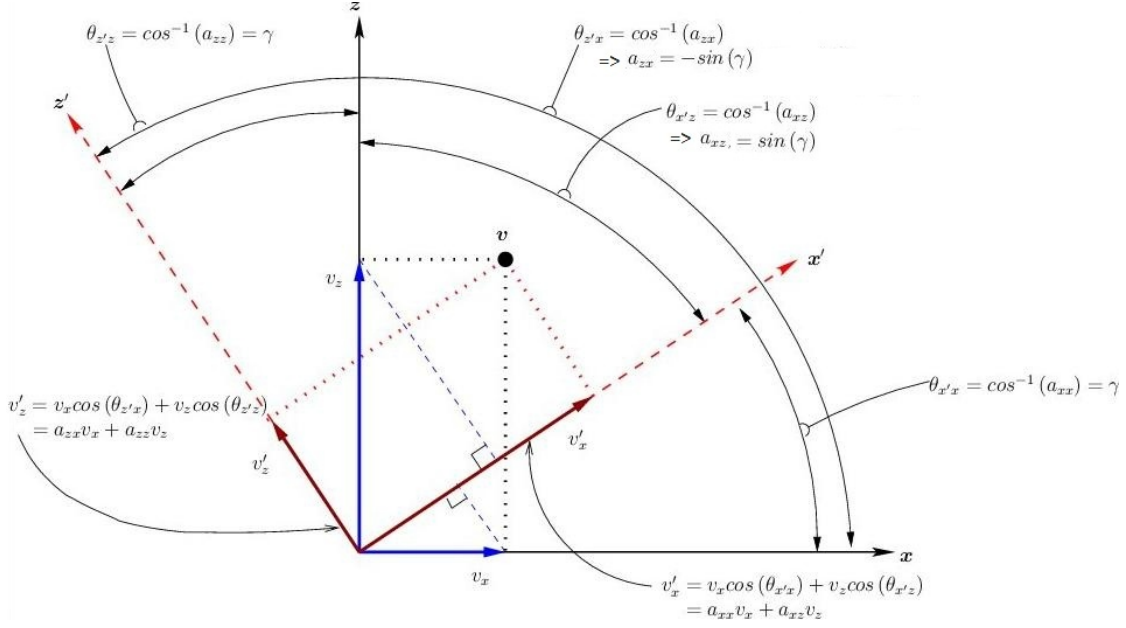
Figure 2.4: Coordinate transformation corresponding to a clockwise rotation, γ, about the y-axis.

Substituting (2.27) and (2.28) into tensor equation (2.26) yields

$$
\begin{aligned}
\boldsymbol{\alpha}'\boldsymbol{a}^T &= \boldsymbol{\Psi}\boldsymbol{a}^T\boldsymbol{\omega}' \\
\Rightarrow \quad \boldsymbol{\alpha}' &= \boldsymbol{a}\boldsymbol{\Psi}\boldsymbol{a}^T\boldsymbol{\omega}',
\end{aligned}
$$

implying that the transformed second order tensor, in new coordinates, is given by

$$
\boldsymbol{\Psi}' = \boldsymbol{a}\boldsymbol{\Psi}\boldsymbol{a}^T , \tag{2.29}
$$

or in element form

$$
\Psi'_{ij} = a_{ik}\Psi_{kl}a_{jl} .
$$

Since the strain and stress tensors are second order tensors, they can both be transformed using the formula above. By rearranging and inserting

$$
\boldsymbol{\tau}' = \boldsymbol{a}\boldsymbol{\tau}\boldsymbol{a}^T
$$

and

$$
\boldsymbol{\epsilon}' = \boldsymbol{a}\boldsymbol{\epsilon}\boldsymbol{a}^T
$$

into Hooke's Law (2.11), a transformed version, in a new coordinate system, is obtained. This is given by

$$
\boldsymbol{\tau}' = \boldsymbol{a}\boldsymbol{a}^T\boldsymbol{C}\boldsymbol{a}^T\boldsymbol{a}\boldsymbol{\epsilon}' .
$$

By following the same procedure as before, comparing the new and transformed equation with the original, the fourth order rotated stiffness tensor is found to be

$$\boldsymbol{C'} = \boldsymbol{a}\boldsymbol{a}^T\boldsymbol{C}\boldsymbol{a}^T\boldsymbol{a} \tag{2.30}$$

in matrix form, and

$$C'_{mnop} = a_{mi}a_{nj}C_{ijkl}a_{ok}a_{pl} \tag{2.31}$$

in component form. This result applies to all fourth order tensors.

To enhance the workability of Hooke's Law, abbreviated subscript notation is always used. A stiffness tensor will for example hardly ever be represented by anything other than a 6×6 matrix. It is therefore very important to find a way of rotating stress, strain and stiffness tensors in abbreviated subscript notation directly, without having to go back and forth between notations.

Take for example the stress element, τ_{xx}. The transformation of this element using equation (2.5) yields

$$\tau'_{xx} = a^2_{xx}\tau_{xx} + a^2_{xy}\tau_{yy} + a^2_{xz}\tau_{zz} + 2a_{xy}a_{xz}\tau_{yz} + 2a_{xx}a_{xz}\tau_{xz} + 2a_{xx}a_{xy}\tau_{xy} \ ,$$

after applying the stress symmetries. Then, after swapping the stress elements with the proper abbreviated elements, the transformed stress component in abbreviated subscripts becomes

$$\sigma'_1 = a^2_{xx}\sigma_1 + a^2_{xy}\sigma_2 + a^2_{xz}\sigma_3 + 2a_{xy}a_{xz}\sigma_4 + 2a_{xx}a_{xz}\sigma_5 + 2a_{xx}a_{xy}\sigma_6 \ .$$

Exactly the same can be done for all components in the stress tensor, resulting in a new transformation formula for the second order tensor in abbreviated subscripts;

$$\sigma'_i = M_{ij}\sigma_j \ , \tag{2.32}$$

where $i, j = 1, 2, .., 6$ and M_{ij} is an element of the transformation matrix

$\boldsymbol{M} =$

$$\begin{pmatrix} a^2_{xx} & a^2_{xy} & a^2_{xz} & \vdots & 2a_{xy}a_{xz} & 2a_{xz}a_{xx} & 2a_{xx}a_{xy} \\ a^2_{yx} & a^2_{yy} & a^2_{yz} & \vdots & 2a_{yy}a_{yz} & 2a_{yz}a_{yx} & 2a_{yx}a_{yy} \\ a^2_{zx} & a^2_{zy} & a^2_{zz} & \vdots & 2a_{zy}a_{zz} & 2a_{zz}a_{zx} & 2a_{zz}a_{zy} \\ \cdots & \cdots & \cdots & \cdots & \cdots & \cdots & \cdots \\ a_{yx}a_{zx} & a_{yy}a_{zy} & a_{yz}a_{zz} & \vdots & a_{yy}a_{zz} + a_{yz}a_{zy} & a_{yx}a_{zz} + a_{yz}a_{zx} & a_{yy}a_{zx} + a_{yx}zy \\ a_{zx}a_{xx} & a_{zy}a_{xy} & a_{zz}a_{xz} & \vdots & a_{xy}a_{zz} + a_{xz}a_{zy} & a_{xz}a_{zx} + a_{xx}a_{zz} & a_{xx}a_{zy} + a_{xy}zx \\ a_{xx}a_{yx} & a_{xy}a_{yy} & a_{xz}a_{yz} & \vdots & a_{xy}a_{yz} + a_{xz}a_{yy} & a_{xz}a_{yx} + a_{xx}a_{yz} & a_{xx}a_{yy} + a_{xy}yx \end{pmatrix} \ .$$

Similar simplifications can naturally also be done to strain, giving a slightly different transformation matrix, $\boldsymbol{N}$, used to relate strain before rotation to strain after rotation. In fact, $\boldsymbol{M}$ and $\boldsymbol{N}$ are equal, except that the factors 2 appearing in $\boldsymbol{M}$ are moved from the upper right-hand corner to the lower left-hand corner in $\boldsymbol{N}$. It can thus be shown that

$$\boldsymbol{N}^{-1} = \boldsymbol{M}^T \ ,$$

which finally gives

$$\boldsymbol{\sigma}' = \boldsymbol{M}\boldsymbol{C}\boldsymbol{M}^T\boldsymbol{\epsilon}' \tag{2.33}$$

after a substitution of (2.32) and the equivalent equation for strain transformation into Hooke's Law. Consequently, a general rotated elastic modulus in three dimensions (and in abbreviated subscript notation) is given mathematically by

$$\boldsymbol{C}' = \boldsymbol{M}\boldsymbol{C}\boldsymbol{M}^T \ . \tag{2.34}$$

One should keep in mind that a positive angle in the transformation matrix, $\boldsymbol{M}$, corresponds to a *counter-clockwise* rotation of the coordinate system. This is again equivalent to a *clockwise* rotation of the medium itself. All general rotations can be performed by three sequential rotations, each about one single axis.

Chapter 3

Elastic upscaling

The earth must be investigated at many different scales in order to get an accurate picture of what lies beneath the surface, and how it behaves. Seismic data, well data, core sample data and pore scale data all give essential information about the properties of a reservoir. Consequently, in order to incorporate as much knowledge into the reservoir description as possible, models portraying geological features at different scales are created. The extents of these models range typically from a millimeter to a kilometer, at the pore scale and simulation scale, respectively. In between, information is stored at the lithofacies/core scale (centimeter) and the facies scale (meter). In a perfect world, a reservoir model would represent the entire reservoir, and have a resolution so good that the tiniest features in the ground would be accounted for. This however, is impossible. Imagine a reservoir being thousand meters wide, thousand meters long and hundred meters thick. Populating such a model with cells small enough to describe pores would have made it useless in practice. With today's computational power, simulations on a dataset of that typical size cannot be performed. Although the progress trend in computer technology clearly predicts that a reservoir one day can be represented by a single model having cells with almost no volume, it presently has to be described with several. Accordingly, there is a need to upscale physical properties in order to pass information from a smaller to a larger scale and preserve connectivity between sources of information. Since the geological features at the pore scale contribute to the properties at the lithofacies scale, and so on, a reservoir modeling workflow should ideally look like the one seen in figure 3.1. By following this process step by step, even the smallest geological features in the reservoir are accounted for. In this study, however, the first upscaling-stage has been skipped due to lack of elastic lamina data.

Rocks are heterogeneous at all scales, with properties varying in three dimensions. Some rocks are certainly more homogeneous than others, but heterogeneities will always be present in the earth. Two waves that travel through a formation following different paths will for example travel at different speeds. If a block consists of different layers of rock, some being harder than others, a wave will obviously alternate between propagating slow and fast depending on the layer it is in. This, however, is only true for waves
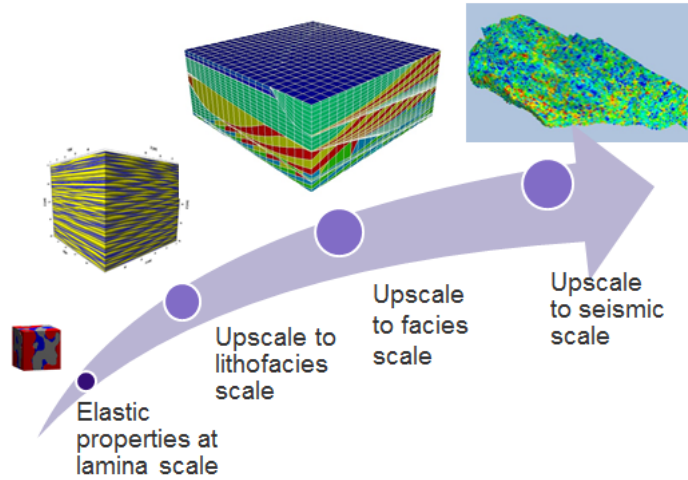
Figure 3.1: Reservoir modeling workflow. To catch geological reservoir features at all scales, elastic properties should be upscaled and passed on as input to the larger model.

with short wavelengths. Whenever wavelengths are longer than the heterogeneities (e.g. layer thicknesses) they run into, the waves will move at velocities being somewhat the average of the velocities of the different rocks [8]. Due to this fact, reflection seismology will not be able to visualize layers that are thinner than the applicable wavelengths in seismic surveys. It is therefore fully valid and necessary to upscale information from the core and well log scale to the seismic scale whenever data from the different sources of information are to be combined or compared. Since seismology provides one of the few ways of "looking" into the ground without having to drill, coupling of well and core data with seismic data is extensively done.

The concept of upscaling is fairly simple. One has a volume of heterogeneous material, and one wants to represent that as a volume of homogeneous material yielding identical properties. A wave should for example travel just as fast through an ideally upscaled formation as the original one containing different types of rock. Mathematical and statistical homogenization is often stated to be equivalent to upscaling when representative elementary volumes (REVs) exist in the medium of interest [6]. A REV is defined as the smallest volume of a material in which the properties represent the entire volume as a whole. When properties are measured in samples smaller than REVs, the results tend to vary. As the sample size gets larger, the variations gradually extinguish until the REV is reached. The properties will still remain the same after further expansion until samples are so large that new layers are introduced. Upscaling is assumed to be valid in the static limit, which implies infinitely long wavelengths or, in other words, wavelengths much larger than the heterogeneities. The concept of homogenization is illustrated in figure 3.2.
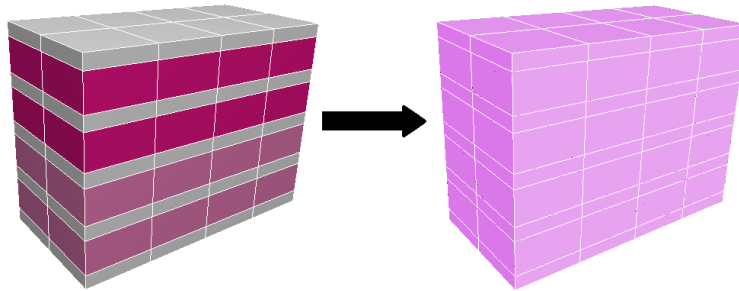
Figure 3.2: The concept of upscaling and homogenization. Want to find a homogeneous body (right) equivalent to a heterogeneous one (left). Both should yield the same properties at the scale of the model.

Effective Medium Theories (EMTs) have been constructed to predict effective properties of mediums composed of more than one material, based on the properties of the various constituents and their volume fractions. Geological formations with small degrees of heterogeneity can thus easily, with little computation time, be upscaled using the latter methods. One EMT of particular interest is called Backus Averaging. This provides analytical upscaling-solutions to certain geological structures. In case of complex formations with advanced geometries and material symmetries, the effective properties depend on volume weights, elastic parameters *and* configurations. No analytical solution exists for complex geometries.

3.1 Backus Averaging

Backus Averaging is a simple upscaling method used in the case of simple geology. The theory states that a horizontal, perfect layered medium, composed of isotropic or transverse isotropic material, behaves like a homogeneous transverse isotropic medium when wavelengths exceed the layer thicknesses. This implies that a homogenized medium should yield exactly the same properties, including velocities, as the original heterogeneous one. The homogeneous medium, said to be "long-wave equivalent" to the original medium [7], is obviously described by five transverse isotropic elastic parameters. These are derived from algebraic combinations of volume weighted averages of the various elastic coefficients in the heterogeneous medium. The density of the homogeneous medium is the average density.

As previously stated, much of the subsurface consists of nearly perfect layers, either aligned horizontally or with a given angle due to some kind of geological rotation. Assuming that the layers have a common, vertical symmetry axis and consist of isotropic and/or transverse isotropic material, Backus Averaging can be employed on earth models directly. However, for rotated layers with a common symmetry axis, the effective elastic

modulus is obtained using both Backus Averaging and tensor rotation (see section 2.5). First the elastic modulus is found in a coordinate system having a z-axis perpendicular to the bedding, and then a tensor rotation is applied to give an effective modulus represented in natural coordinates. This, of course, will be the case when the z-axis is aligned vertically. The resulting tensor still has five independent components, but will not have the same form.

The ith horizontally oriented layer with vertical symmetry axis is described by the TI isotropic tensor

$$
C_i = \begin{pmatrix} a_i & a_i - 2e_i & b_i & 0 & 0 & 0 \\ a_i - 2e_i & a_i & b_i & 0 & 0 & 0 \\ b_i & b_i & c_i & 0 & 0 & 0 \\ 0 & 0 & 0 & d_i & 0 & 0 \\ 0 & 0 & 0 & 0 & d_i & 0 \\ 0 & 0 & 0 & 0 & 0 & e_i \end{pmatrix},
$$

where a, b, c, d and e are the five independent elastic parameters. The effective elastic modulus generated by Backus Averaging then becomes

$$
C_{eff} = \begin{pmatrix} A & A - 2E & B & 0 & 0 & 0 \\ A - 2E & A & B & 0 & 0 & 0 \\ B & B & C & 0 & 0 & 0 \\ 0 & 0 & 0 & D & 0 & 0 \\ 0 & 0 & 0 & 0 & D & 0 \\ 0 & 0 & 0 & 0 & 0 & E \end{pmatrix},
$$

where

$$
\begin{aligned}
A &= \langle a - b^2 c^{-1} \rangle + \langle c^{-1} \rangle^{-1} \langle bc^{-1} \rangle^2 \\
B &= \langle c^{-1} \rangle^{-1} \langle bc^{-1} \rangle \\
C &= \langle c^{-1} \rangle^{-1} \\
D &= \langle d^{-1} \rangle^{-1} \\
E &= \langle e \rangle
\end{aligned}
$$

$\langle \cdot \rangle$ denotes the volume weighted average over all layers. For a medium containing only isotropic layers, the equations above turn into

$$
\begin{aligned}
A &= \langle \tfrac{4\mu(\lambda+\mu)}{\lambda+2\mu} \rangle + \langle \tfrac{1}{\lambda+2\mu} \rangle^{-1} \langle \tfrac{\lambda}{\lambda+2\mu} \rangle^2 \\
B &= \langle \tfrac{1}{\lambda+2\mu} \rangle^{-1} \langle \tfrac{\lambda}{\lambda+2\mu} \rangle \\
C &= \langle \tfrac{1}{\lambda+2\mu} \rangle^{-1} \\
D &= \langle \tfrac{1}{\mu} \rangle^{-1} \\
E &= \langle \mu \rangle
\end{aligned}
\tag{3.1}
$$

where λ is Lamé's first parameter and μ is the shear modulus.

The effective elastic modulus obtained from Backus' formula is the analytical solution to the homogenization problem, provided that the medium of interest meets the given

requirements. Backus Averaging is also usable when the layers are *approximately* flat. Since it is a fairly simple method that occupies computer power for very short times, it is often the preferred choice. Obviously the correctness of the method depends on the flatness of the layers. Hence, Backus Averaging should not be applied to complex geometries. In that case, a general method should rather be employed.

3.2 Voigt and Reuss bounds

Up until now, geometrical details in rocks and sediments have not been adequately incorporated into homogenization theory. Many methods do indeed address this problem, but assumptions and simplifications always seem to take away a lot of their generality. Backus Averaging is a good example - very useful, but applicable only in limited studies. By disregarding the geometrical effects in rock compositions, and exclusively focus on the volume weights of the constituents and their elastic properties, only upper and lower *bounds* can be predicted for the effective elastic moduli and velocities [9]. Clearly, calculated bounds do not provide true solutions to rock homogenization. They do, however, work as strong indicators. Since the true elastic tensors are restricted by the bounds and must fall between them, and since bounds can be calculated for any geometry, they must be considered both powerful and valuable tools in rock physics. Bounds suffer little from the assumptions made in many geometry-specific upscaling techniques, and are hence very robust and reliable.

The Voigt and Reuss bounds, named after their inventors, are one set of many existing bounds. They are not necessarily the best ones, but due to their simplicity, they are the preferred choice in this thesis. Both bounds were originally derived to resolve the problem of homogenization. While Voigt assumed uniform stress throughout the composite and averaged the expressions for strain, Reuss assumed uniform strain averaged over stress. However, stress and strain are expected to be non-uniform, and later a mathematician named Wiener was able to show that Voigt and Reuss actually had found the upper and lower bounds on the effective elastic modulus, respectively. The proof is provided in [10]. For a composite with N different constituents, the Voigt upper bound, M_V, and the Reuss lower bound, M_R, are given as

$$M_V = \sum_{i=1}^{N} f_i M_i \tag{3.2}$$

$$M_R = \frac{1}{\sum_{i=1}^{N} f_i \frac{1}{M_i}} \tag{3.3}$$

where f_i is the volume fraction ($\frac{V_i}{V_{tot}}$) of the ith material with elastic modulus M_i. As stated in [9]; the arithmetic average of the constituent moduli given in (3.2) is elastically the "stiffest" possible mixture that can be put together by nature, and the harmonic average of the moduli given in (3.3) is the "softest". It is also worth mentioning that

the difference between bounds is dependent on the constituents. A model with small contrasts in material properties that is close to isotropic at the model length-scale, will give almost identical upper and lower bounds. The smaller the difference, the closer the bounds are to the real effective moduli. One can also quite simply take the average of the two. This is called the Voigt-Reuss-Hill average, and will statistically yield a more accurate solution compared to the bounds, if the effective modulus is completely unknown.

Methods that consider not only volume fractions and elastic properties, but also the arrangement of the constituents in a composite, are often time consuming and computationally heavy. In many cases, it is unnecessary to do these accurate calculations. Upper and lower bounds can easily be obtained, and, as mentioned above, they can be very close to the true solution. A good strategy might therefor be to find the bounds and then, based on their distance, evaluate whether a general upscaling is needed or not. In this respect, it would be useful to have bounds for both materials that are isotropic and anisotropic at the microscopic scale. This means that bounds should be available for models that are either isotropic or anisotropic at cell level. Since materials are assumed either isotropic or transverse isotropic in this study (due to lack of elastic data), they will be the only symmetries accounted for. Much of the upcoming theory is taken from [8].

The Voigt and Reuss averages, given in equations (3.2) and (3.3), can be applied to isotropic materials directly. M_i can be substituted by any isotropic elastic moduli, such as μ, K, E and so on. However it makes most sense to calculate the effective material's upper and lower bounds for the bulk modulus, K, and shear modulus, μ, and then find the other parameters through the relations given in table 2.2. Furthermore, equation (2.23) can be utilized to express the bounds as velocities. By inserting $\mu = \rho V_S^2$ and $K = \rho \left(V_P^2 - \frac{4}{3} V_S^2 \right)$ into the equations derived by Voigt and Reuss, upper and lower bounds will yield:

$$\mu_V = \sum_{i=1}^{N} f_i \mu_i = \sum_{i=1}^{N} f_i \rho_i V_{S_i}^2$$

$$K_V = \sum_{i=1}^{N} f_i K_i = \sum_{i=1}^{N} f_i \rho_i \left(V_{P_i}^2 - \frac{4}{3} V_{S_i}^2 \right)$$

$$\mu_R = \frac{1}{\sum_{i=1}^{N} f_i \frac{1}{\mu_i}} = \frac{1}{\sum_{i=1}^{N} f_i \frac{1}{\rho_i V_{S_i}}}$$

$$K_R = \frac{1}{\sum_{i=1}^{N} f_i \frac{1}{K_i}} = \frac{1}{\sum_{i=1}^{N} f_i \frac{1}{\rho_i \left(V_{P_i}^2 - \frac{4}{3} V_{S_i}^2 \right)}}$$

The Voigt upper bound described by μ_V and K_V and the Reuss lower bound described by μ_R and K_R will give the maximum possible and minimum possible velocities of the effective medium, which is microscopically isotropic.

These bounds, however, are not true for composites that consist of transverse isotropic materials. As discussed in section 2.4, symmetry of this kind will give three wave velocities - V_P, V_{SH} and V_{SV}. These are all dependent on the direction of the wave propagation. To get the upper and lower bounds on the effective tensor, one must therefore consider velocities at all possible angles. The upper and lower bounds for composites with non-isotropic constituents can then be given as

$$\mu_{Upper} = \sum_{i=1}^{N} f_i \rho_i max \left(V_{S_i}^2 \right)$$

$$K_{Upper} = \sum_{i=1}^{N} f_i \rho_i max \left(V_{P_i}^2 - \frac{4}{3} V_{S_i}^2 \right)$$

$$\mu_{Lower} = \frac{1}{\sum_{i=1}^{N} f_i \frac{1}{\rho_i min \left(V_{S_i}^2 \right)}}$$

$$K_{Lower} = \frac{1}{\sum_{i=1}^{N} f_i \frac{1}{\rho_i min \left(V_{P_i}^2 - \frac{4}{3} V_{S_i}^2 \right)}}$$

(3.4)

where the *min* and *max* functions are over all directions and over both shear waves. Since these operations bring the number of velocities and elastic parameters down to two, the upper and lower bounds must be describing the velocity limits of an *imaginary* isotropic material.

In order to find boundaries on the upscaled elastic tensor of a body composed of transverse isotropic material, the transverse isotropic wave velocities in equation (2.24) are put to use in $max \left(V_{S_i}^2 \right)$, $max \left(V_{P_i}^2 - \frac{4}{3} V_{S_i}^2 \right)$, $min \left(V_{S_i}^2 \right)$ and $min \left(V_{P_i}^2 - \frac{4}{3} V_{S_i}^2 \right)$. Next, the extremal points are computed in the usual way by differentiating the expressions with respect to direction, θ, and set them equal to zero. The terms to solve are

$$\frac{\partial}{\partial \theta} V_{SV}^2 (\theta) = 0$$

$$\frac{\partial}{\partial \theta} V_{SH}^2 (\theta) = 0$$

$$\frac{\partial}{\partial \theta} \left[V_P^2 (\theta) - \frac{4}{3} V_{SV}^2 (\theta) \right] = 0$$

$$\frac{\partial}{\partial \theta} \left[V_P^2 (\theta) - \frac{4}{3} V_{SH}^2 (\theta) \right] = 0$$

where θ is the angle from the transverse isotropic symmetry axis. The equalities above are true for $\theta = n\frac{\pi}{2}$, with n being a natural number ($n \in \mathbb{N}$). Other additional solutions do also exist, but they are much harder to find. For transverse isotropic materials that are not too far from isotropic, Thomsen's weak anisotropy approximation can be utilized

to simplify the process. The transverse isotropic velocities can be approximated by

$$V_P(\theta) \approx \alpha_0 \left[1 + \delta sin^2(\theta) cos^2(\theta) + \epsilon sin^4(\theta) \right]$$

$$V_{SV}(\theta) \approx \beta_0 \left[1 + \frac{\alpha_0^2}{\beta_0^2}(\epsilon - \delta) sin^2(\theta) cos^2(\theta) \right] \tag{3.5}$$

$$V_{SH}(\theta) \approx \beta_0 \left[1 + \gamma sin^2(\theta) \right]$$

where

$$\epsilon = \frac{C_{11} - C_{33}}{2C_{33}}$$

$$\gamma = \frac{C_{66} - C_{44}}{2C_{44}}$$

$$\delta = \frac{(C_{13} + C_{44})^2 - (C_{33} - C_{44})^2}{2C_{33}(C_{33} - C_{44})}$$

and

$$\alpha_0 = \sqrt{C_{33}/\rho} \quad \beta_0 = \sqrt{C_{44}/\rho} \qquad .$$

The three first parameters, ϵ, γ and δ, are called the Thomsen parameters [11], and are measures of anisotropy. As long as the values of these parameters are small, that is $|\epsilon| \leq 0.1$, $|\gamma| \leq 0.1$ and $|\delta| \leq 0.1$, the approximations are assumed satisfactory.

Because the derivatives of Thomsen's expressions given in (3.5) are easier obtained compared to the derivatives of the exact transverse isotropic velocities in (2.24), the remaining extrema are found using the weak anisotropy approximation. The extremal points for $V_P^2 - \frac{4}{3}V_{SV}^2$, $V_P^2 - \frac{4}{3}V_{SH}^2$ and V_{SV}^2 turn out to be

$$\theta \approx sin^{-1}\left(\pm \sqrt{\frac{\frac{4}{3}\frac{\alpha_0}{\beta_0}(\epsilon - \delta) - \delta}{2\left(\frac{4}{3}\frac{\alpha_0}{\beta_0} + 1\right)(\epsilon - \delta)}} \right)$$

$$\theta \approx sin^{-1}\left(\pm \sqrt{\frac{4}{3}\frac{\beta_0}{\alpha_0}\frac{\gamma}{(\delta + 2(\epsilon - \delta))}} \right)$$

$$\theta \approx \frac{\pi}{4}$$

,

respectively. Thus, in order to get the maximum shear wave velocity, $max\left(V_{S_i}^2\right)$, in equation (3.4), one has to solve:

$$max\left(V_{S_i}^2\right) = max\left(V_{SH_i}, V_{SV_i}\right)^2$$

with the two maximum shear wave velocities being

$$
max\left(V_{SV_i}\right) = max \begin{cases} V_{SV_i}(0) \\ V_{SV_i}\left(\frac{\pi}{2}\right) \\ V_{SV_i}\left(sin^{-1}\left[\sqrt{\frac{\frac{4}{3}\frac{\alpha_0}{\beta_0}(\epsilon-\delta)-\delta}{2\left(\frac{4}{3}\frac{\alpha_0}{\beta_0}+1\right)(\epsilon-\delta)}}\right]\right) \\ V_{SV_i}\left(sin^{-1}\left[-\sqrt{\frac{\frac{4}{3}\frac{\alpha_0}{\beta_0}(\epsilon-\delta)-\delta}{2\left(\frac{4}{3}\frac{\alpha_0}{\beta_0}+1\right)(\epsilon-\delta)}}\right]\right) \end{cases} \tag{3.6}
$$

$$
max\left(V_{SH_i}\right) = max \begin{cases} V_{SH_i}(0) \\ V_{SH_i}\left(\frac{\pi}{2}\right) \\ V_{SH_i}\left(sin^{-1}\left[\sqrt{\frac{4}{3}\frac{\beta_0}{\alpha_0}\frac{\gamma}{(\delta+2(\epsilon-\delta))}}\right]\right) \\ V_{SH_i}\left(sin^{-1}\left[-\sqrt{\frac{4}{3}\frac{\beta_0}{\alpha_0}\frac{\gamma}{(\delta+2(\epsilon-\delta))}}\right]\right) \end{cases} \quad .
$$

The same calculations must also be done for $min\left(V_{S_i}^2\right)$, $max\left(V_{P_i}^2 - \frac{4}{3}V_{S_i}^2\right)$ and $min\left(V_{P_i}^2 - \frac{4}{3}V_{S_i}^2\right)$. If the goal is to get as accurate bounds as possible, the exact velocities in equation (2.24) can be utilized in (3.6) instead of Thomsen's velocity approximations. In that way the approximations only lie in the process of finding angles, and not in the speeds. Due to the approximations, it is no longer guaranteed that the true effective moduli fall between the bounds. However, they will typically still predict the range in which the effective velocities of a given material composition must reside - even if not completely accurate.

3.3 OPM-upscaling - the general method

As mentioned earlier, there will always be advanced heterogeneities and anisotropies in the earth. Reservoir models, aiming to describe a certain reservoir feature in detail, will consequently never fully satisfy the requirements demanded by Backus Averaging or similar homogenization theories. To solve the upscaling problem for complex models, a more general method is needed. As a first of its kind, a method taking into account the geometry of the models is provided in the Open Porous Media (OPM) software package. OPM is an open-source codebase which provides tools centered around simulation of transport and flow of fluids in porous media, applicable, inter alia, in reservoir and enhanced oil recovery engineering. The project started in 2009 at the Statoil Research Center in Trondheim, and today six research groups and several partners contribute. The code, consisting of a mix between old and newly developed tools, is constantly evolving. To fetch the newest version of the source code, one can go to [27]. It is the module called OPM-Upscaling which implements the general upscaling method utilized in this master thesis. The method upscales any model, and is independent of scale. This means that a model can be upscaled from $1mm$ to $1cm$ just as well as from $100m$ to $1km$. The accuracy of the method is analyzed in chapter 5.

To upscale the elastic properties of a medium using OPM-Upscaling, the following Linux command is executed:

`upscale_elasticity gridfilename=`*gridfile.grdecl* `rock_list=`*rocklist.txt* `output=`*output.txt*

The *gridfile.grdecl* is an Eclipse grid file containing the model to be upscaled. The *rocklist.txt* is a simple book-keeping file pointing to other text files containing elastic properties of rocks, which the model is saturated with. The *output.txt* is the name of the generated output containing the upscaled elastic tensor. Several other flags can also be added to the line above. Among the most relevant ones are `method`, `linsolver_type` and `ltol` which determine what kind of boundary couplings are used, the type of linear solver, and the relative error tolerance in the iteration solvers, respectively. The default values are *Mortar*, *cg* and *1e-08*. For large systems/models with $5 \cdot 10^4 - 5 \cdot 10^5$ unknowns, these are the prefered choices. However, for smaller systems, the linear solver should be changed to *direct*. For systems that are extremely large, the linear solver should be set to the default value, and the boundary couplings to *MPC*. The Direct Sparse LU (*direct*) solver gives better accuracy than the Conjugate Gradient (*cg*) solver, and the Mortar couplings are more accurate than the MPC couplings. They are also more memory intensive. One should therefore always try to optimize the balance between memory usage and accuracy. A full list of command line options can be found in [28].

If a model consists of three different rocks, a *rocklist.txt*-file would have four lines and typically look like

rocklist.txt
3
rock1.txt
rock2.txt
rock3.txt

Let *rock1* have isotropic symmetry, *rock2* have transverse isotropic symmetry and *rock3* have any other symmetry other than the two. The text file *rock1.txt* should then have the structure

rock1.txt
`km`
value1 value2
`density`
density

where `km` can be substituted with `vpvs`, `lm` and `en`. This line allows the user to specify either bulk modulus (K) and shear modulus (μ), P-velocity (V_P) and S-velocity (V_S), Lamé's first parameter (λ) and shear modulus (μ), or Young's modulus (E) and Poissons ratio (ν). The structure of the *rock2.txt*-file would be:

rock2.txt
`ti`
a b c d e
`density`
density

where a, b, c, d and e are the five independent elastic coefficients describing a transverse isotropic material. Finally, *rock3.txt* should look like:

rock3.txt
`C`
c_{11} c_{12} c_{13} ... c_{16} c_{22} c_{23} ... c_{66}
`density`
density

Elastic moduli for each input cell can also be specified on a per-cell basis in the *.grdecl*-file by assigning a pair of elastic parameters to each grid-cell. In this thesis, both ways of providing input are employed.

The general upscaling method provided by OPM is based on a Finite Element Method, which solves the differential equation for displacement. First, the method applies a convenient external force that purely strains the entire body of interest, giving only one non-zero strain component. The displacement, strain and stress can then be calculated for every single cell in the model. Having the fine-scaled stress in each cell, the program easily computes the effective stress of the model as a whole. Hence, both the coarse-scale strain and stress is known, and one column in the elastic modulus corresponding to the applied boundary condition can be obtained by the application of Hooke's Law. Since a general deformation can be described by three normal strains and three shear strains (see figure (2.2)), the procedure must be performed six times to get a complete upscaled stiffness matrix. It should also be mentioned that a lot of the implemented homogenization theory (such as the relationships used to get small-scale displacement and large-scale stress) assumes periodicity of the medium. The accuracy of the general method and the periodicity of the model should therefore be positively correlated. Further readings about the general upscaling method can be found in [13].

Chapter 4

Pictorial representation of elastic tensors

An elastic tensor is not exactly easy to interpret or understand. With 36 elements and up to 21 independent elastic coefficients, it is almost impossible to envision a medium's behavior when exposed to some arbitrary force. However, since the elastic modulus is closely related to the wave velocities in a material, one can simply exploit these to visualize the tensor. There are, as discussed, only three types of velocities, all exclusively depending on elastic parameters, density and propagation direction. As a consequence, wave velocities are much easier to keep track of, and naturally also perfect for elastic modulus representation. On top of this, it is conveniently the corresponding velocities which are of interest in this context, not the tensor itself. The velocities are found by employing the Christoffel equation, which was thoroughly reviewed in section 2.4. The main idea behind elastic tensor visualization, and some of the methods, are taken from [8].

In this chapter, it is provided three ways of visualizing elastic moduli. Even though they are all based on the same principle, they each have distinct characteristics that offer advantages over one another in different situations. As one method can visualize a particular feature better than the others, their areas of application are somewhat separated. This makes them all quite interesting to introduce. The first two methods represent tensors in two dimensions, while the last one does it in three. Regardless of dimension, the subsequent plots are all produced by rotating the stiffness matrices iteratively, and solving the Christoffel equation for vertical waves at each step. This process can be done due to the fact that a change in propagation direction is equivalent to rotating the body itself while keeping the propagation direction constant. One can also get the exact same speeds directly from the Christoffel formula, by applying different N-matrices (see section 2.4).

35

4.1   Velocity as radius

Figure 4.1 illustrates how one can picture elastic tensors with corresponding wave veloc-
ities as radii. The blue and utmost line is obviously the P-wave velocity, while the green
and red ones are the two S-wave velocities. In the plot, the two S-wave velocity curves
appear to only touch each other, while they in reality should cross. This is simply an
artifact produced during plotting. Given an angle of wave propagation, the magnitude
of each velocity type is determined by the distance from the origin to the associated line.
To get vertical V_P, for example, one must find the intersection between the blue line and
the y-axis. As illustrated by plot 4.1, it is very intuitive to interpret a material's elastic
behavior, and hence its tensor, when velocities are represented as radii. According to
the shape of the curves in figure 4.1, the corresponding material is stiffer laterally than
vertically. This is typical for a transverse isotropic tensor with vertical symmetry axis.
A fully isotropic medium, on the other hand, would have given constant wave velocities
in all directions, as well as only one S-wave value. Hence, the degree of isotropy in a
tensor can roughly be estimated by the roundness of the curves, complemented by the
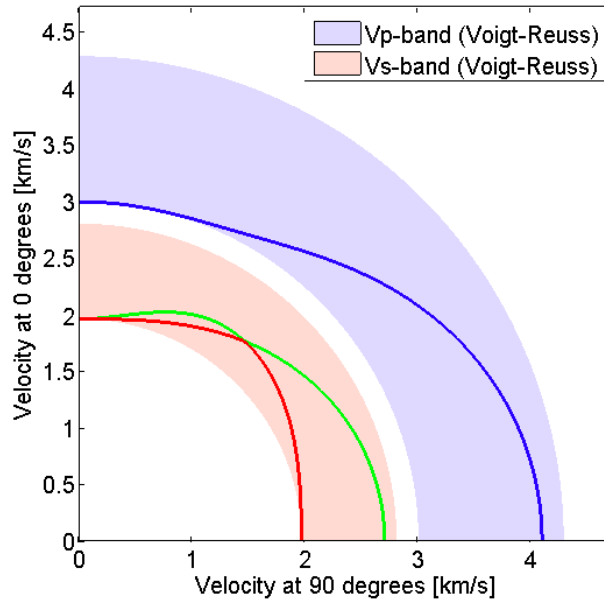discrepancy between the SV- and SH-wave.

Figure 4.1: Example of how to visualize elastic tensors with wave velocities as radii.
The blue, green and red curves represent V_P, V_{SV} and V_{SH}, respectively. For a given
angle, the velocities are determined by the distance from the origin to the curves. The
blue and pink bands, associated with Voigt and Reuss averages, limit the velocities.

Since figure 4.1 is in 2D, it cannot be used as a mean to describe a full anisotropic tensor
that has varying qualities with azimuthal (horizontal) angle. In fact, the best one can

do is to produce several vertical cross-sections at different horizontal angles and examine them in sequence. Additionally, it is not sufficient to plot velocities only in one quadrant $(0-90°)$, if the section is taken from a tensor with low symmetry. The speeds must then at least be displayed in two $(0-180°)$. However, extending figure 4.1 to show a greater range of angles can be done easily. In order to entirely represent an elastic modulus with a plot like 4.1, it must either be isotropic or transverse isotropic with vertical symmetry axis. Only then will the velocities be completely independent of lateral propagation direction. Furthermore, one also has the possibility to average the anisotropic velocities over the azimuthal angles. This is basically equivalent to projecting the tensor into a transverse isotropic symmetry.

If it is desirable, one can easily supplement the tensor plots with Voigt and Reuss bounds (section 3.2), as shown in figure 4.1. Since these bounds provide limits to the effective moduli, they can be extremely valuable in terms of evaluating upscaled elastic properties. Irrespective of geometry, but given a set of constituting volume fractions and isotropic parameters, a medium's effective P-wave and S-wave velocities should never exceed the pale blue and red bands added to figure 4.1. Consequently, with a pictorial representation similar to the one above, one will be able to tell whether a homogenization is far off its true solution, or not. The thickness of the constraining bands grows with increasing material contrasts, which by no means should be confused with anisotropy. Although these two characteristics usually go hand in hand, a material is not necessarily anisotropic whenever the bands are wide. However, as the Voigt and Reuss bounds describe imaginary isotropic mediums, providing perfectly circular velocity curves as radii, it must be true that an effective tensor is close to isotropic when the Voigt and Reuss bounds lie near each other. Due to the broad bands in figure 4.1 and the shape of the velocity curves, the visualized medium is this time certainly composed of materials with large differences in elastic properties that together form an anisotropic tensor after upscaling. The tensor representation, as seen above, is utilized in chapter 5 to validate output from the general upscaling method.

4.2 Velocity vs angle

The second provided way of visualizing elastic tensors can probably be employed with a greater success than the first, if the goal is to investigate the magnitude of the wave velocities, i.e. the stiffness, at different propagation angles. With the tensor representation given in figure 4.1, it is difficult to tell the exact size of the various velocities in any direction other than ones pointed out by the axes. This, however, is not the case when one plots corresponding wave velocities *against* propagation angles, as displayed in figure 4.2. One will then be able to pick an angle at the x-axis and immediately find the magnitude of the velocities at the y-axis. In addition, it is much easier to quantify a material's stiffness variation, and hence anisotropy, with plot 4.2.

Similar to the one presented in the previous section, the pictorial tensor representa-

tion exemplified by figure 4.2 shows only one vertical cross-section at the time. The latter plot displays, however, velocities at a wider range of propagation angles. As the horizontal axis extends from 0 to 180 degrees, any zenithal change in elasticity that may occur within the given section is accounted for. In figure 4.2, the red curve represent the P-wave velocity, while the green and blue curves designate horizontally and vertically polarized S-waves, respectively. Again, the angles are measured from the vertical axis.
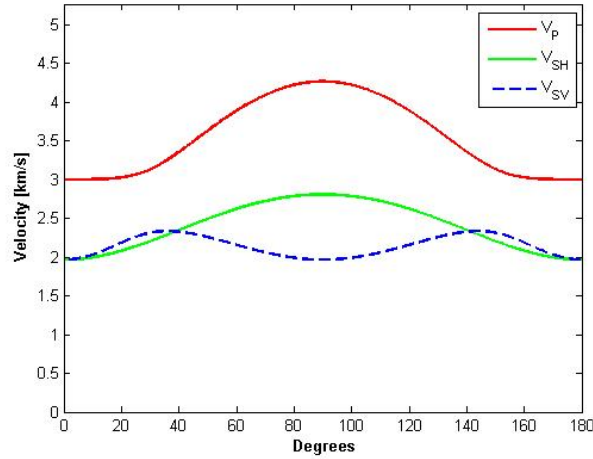
Figure 4.2: Example of how to visualize elastic tensors by plotting velocities against propagation angle. The red, green and blue curves represent V_P, V_{SH} and V_{SV}, respectively. The angles are measured from the vertical z-axis.

The tensor visualized in the above figure, and also in figure 4.1, has in fact a transverse isotropic symmetry that originates from a material composition with periodic and horizontally oriented layers (figure 5.2). Since the method merely displays velocities in one vertical plane, one will not be able to discover this fully with a single plot. However, from the shape of the curves, and the maximum (90 degrees) and minimum (0 and 180 degrees) V_P-values, one can to a great extent indicate a transverse isotropic tensor that has to be symmetric about the vertical axis. Due to the fact that P-waves travel faster along layers than across them, it is only natural that the velocity extrema occur at vertical and horizontal directions. Additionally, the velocity variations in plot 4.2 appear to very large. As isotropic moduli provide constant elastic properties in all directions, and thus generate lateral lines in figure 4.2, the large fluctuations must consequently reflect a high degree of anisotropy. To put it in other words, the pictorial method described in this section brings a superb way of indicating anisotropy.

4.3 Velocity as surface

The visualization technique shown in figure 4.3 stands out from the others by the fact that it represents tensors in three dimensions, not two. With an extra dimension, it is possible to draw velocities as surfaces or shells instead of curves. This means that an elastic tensor can be inspected fully with the use of only one plot. The obvious benefits of the method is, however, far more visible on a computer than on paper. As demonstrated by figure 4.3, it is really hard to envision a material's elastic response to force in every conceivable azimuthal and zenithal direction when the 3D-plot is stamped onto a flat surface. On a computer one can zoom, rotate and pan the image in any possible way to get exactly the information one needs. Besides visualizing the entire tensor at once, the method described here is identical to the one introduced in section 4.1. In fact, plot 4.1 shows only one of an infinite number of cross-sections that can be extracted from a figure like 4.3. As the velocities are represented by radii again, an isotropic tensor should yield two perfectly spherical surfaces - one for P-velocity and one for S-velocity. The elastic moduli displayed in figure 4.3 is, however, transverse isotropic like the others, and provides two separate S-waves. This time V_P is associated with the turquoise surface, while V_{SV} and V_{SH} are associated with the dark and light greens.
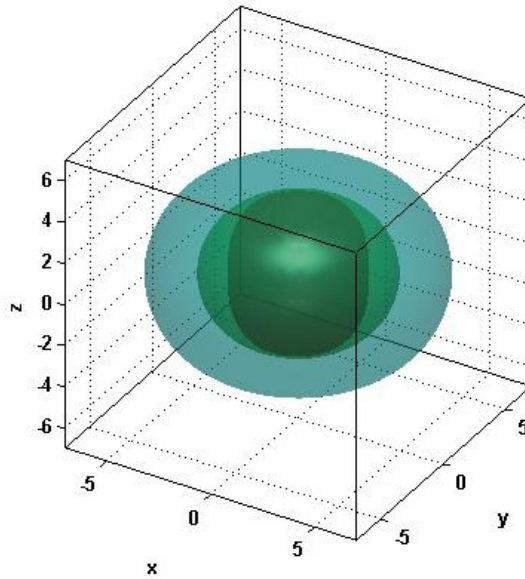

Figure 4.3: Example of how to visualize elastic tensors as velocity surfaces. The turquoise, light green and dark green shells represent V_P, V_{SH} and V_{SV}, respectively. The velocity in a given direction is defined by the distance from the origin to the rightful shell.

Chapter 5

Verification of the OPM-Upscaling (elasticity) code

A fairly extensive analysis of the general upscaling method has previously been performed in [1]. To monitor the behavior of the code with respect to different input features, several models with various distinctive characteristics, such as geometry, symmetry and grid design, were upscaled and evaluated. Since analytical upscaling solutions are non-existent for general geometries and symmetries, all test models in [1] were chosen to consist of isotropic or transverse isotropic materials, arranged in periodic layers. In agreement with the theory presented in section 3.1, exact solutions were hence attainable for each and every model by the utilization of Backus' formula. With analytical solutions on hand, the accuracy and dependencies of the general upscaling method could be studied thoroughly. As a result, it was shown in [1] that the accuracy of the upscaling code is influenced by both model geometry and grid design, in addition to the model's periodicity. The latter property affects the result simply because the implemented homogenization theory based on Backus Averaging works best for periodic models. However, despite these prominent dependencies, it was perhaps the correlation between accuracy and total number of grid cells which captured the widest attention. Plot 5.1, which is taken from [1], reveals a drastic error increase with the number of grid cells. Further analysis discovered that the implemented linear solver did not converge at all for very large grids, giving substantial deviation between true and OPM-upscaled effective moduli. Consequently, the code was revised shortly after the publication of [1], and should now have been improved. Before confidently employing it on general models, however, the method's validity must be determined once more. This is done through yet another upscaling test.

The various test models, of which there are nine in total, are divided into four groups. The first group is reserved for models that are perfectly periodic and have horizontal layering. Similar to all models described in this chapter, the models in group one consist of isotropic material. Of this reason, effective elastic moduli can be found analytically with Backus averages alone. The second group also consists of models with perfect layering, but in this particular group the layers are rotated. This means that a tensor rotation
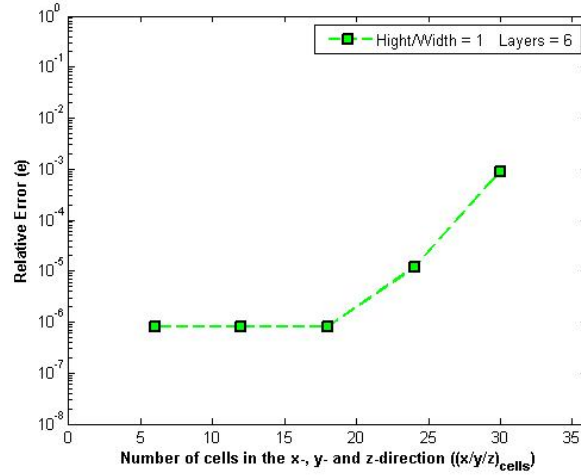
Figure 5.1: Figure illustrating the accuracy problems of the previous code version. The relative error increases drastically with the number of grid cells, even though the model is left unaltered.

must be applied after Backus' formula in order to get true effective properties. Since both groups come with analytical solutions to the homogenization problem, they are certainly well suited for accuracy inspection. The third and fourth group, however, contains models that have irregular grid designs and general geometries. While the third group consists of models with high-contrast elastic material properties, the last and fourth group is limited to one single reservoir model, with more or less realistic material input. The reason for including the last group in the test is to examine the method's behavior in the case of a "real" model, which actually represents those to be used later. As known by now, one cannot compute analytical upscaling solutions for complex geometries. Accordingly, there is no exact way of telling whether OPM-Upscaling is accurate or not for the two last model groups. The best one can do is to constrain the true solution with bounds, such as the ones provided by Reuss and Voigt (see section 3.2), and compare the upscaled properties to these. The validity of the upscaling method is therefore generally evaluated on the basis of plots that display both bounds and upscaled tensors simultaneously. For this, the illustration technique presented in section 4.1 will be used.

As opposed to the previous test, the models are upscaled with both the iterative *and* the direct linear solver. Owing to the fact that reservoir models get really large in this thesis (10^6 cells), the upscaling times may increase significantly. Because of this, one is forced to consider, not only accuracy, but also duration. The iterative solver is known to be faster than the direct solver on larger grids, and it is hence interesting to see how much time one can save by choosing the one solver above the other. Additionally, it is intriguing to find out what one must sacrifice in terms of accuracy to lower the upscaling time. When it comes to the boundary couplings, the default mortar method was used on

all occasions. Similarly, the relative error tolerance was assigned the default value 10^{-8}. A couple of models were also upscaled with even lower tolerances, but no differences could be seen in the resulting elastic moduli. The upscaling time, however, increased with lower tolerance.

5.1 Horizontal layers

The first couple of models that were upscaled and evaluated during this test are shown in figure 5.2. They are both composed of two materials arranged in ten alternating layers, and have 400 cells in the horizontal plane. From the illustrations it is hard to notice the difference between the two models, but model 5.2a has 30 vertical cells and model 5.2b has 40. The materials that constitute the models have isotropic symmetry and are described elastically by

$$\begin{array}{rclrcl} \lambda_1 & = & 5/3 & \mu_1 & = & 5 \\ \lambda_2 & = & 10 & \mu_2 & = & 30 \end{array} \qquad (5.1)$$

where λ is Lamé's first parameter and μ is the shear modulus. The values assigned to the elastic parameters are so-called "dummy" values, which have no physical meaning. They are simply chosen to create large elastic contrasts between layers, so that the upscaled moduli are far from isotropic.
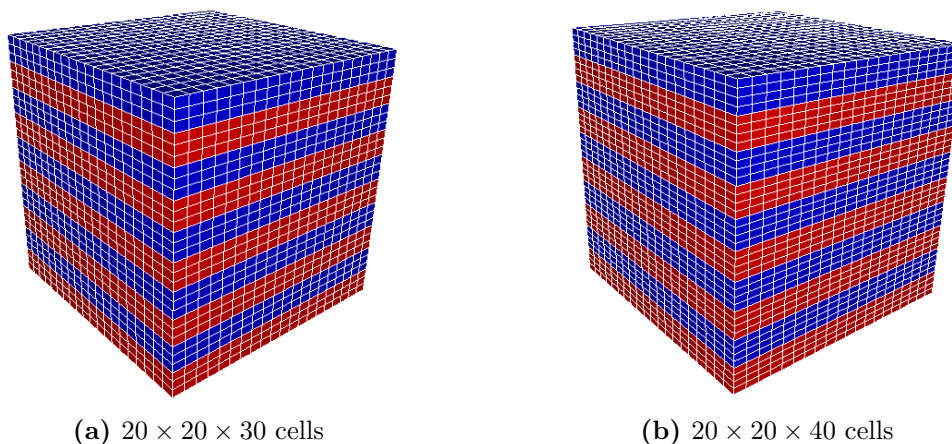

(a) $20 \times 20 \times 30$ cells   **(b)** $20 \times 20 \times 40$ cells

Figure 5.2: Perfectly periodic models with horizontal layering. (a) shows a variant with 30 cells in the z-direction and 20 cells in x- and y-directions, while variant (b) consists of 40 cells vertically. They are both fulfilling the requirements of Backus' formula.

Effective elastic moduli computed with Backus' theory depend only on the elastic properties of the constituting materials and their individual volume fractions. Since the two models in 5.2 are identical in composition, they must necessarily have the same analytical solution. By utilizing the isotropic version of Backus' formula given in equation

(3.1), five effective elastic coefficients can be obtained. In this case, they are given by

$$
\begin{aligned}
A &= \left\langle \frac{4\mu(\lambda+\mu)}{\lambda+2\mu} \right\rangle + \left\langle \frac{1}{\lambda+2\mu} \right\rangle^{-1} \left\langle \frac{\lambda}{\lambda+2\mu} \right\rangle^{2} &&= 40.4082 \\
B &= \left\langle \frac{1}{\lambda+2\mu} \right\rangle^{-1} \left\langle \frac{\lambda}{\lambda+2\mu} \right\rangle &&= 2.8571 \\
C &= \left\langle \frac{1}{\lambda+2\mu} \right\rangle^{-1} &&= 20.0000 \\
D &= \left\langle \frac{1}{\mu} \right\rangle^{-1} &&= 8.5714 \\
E &= \langle \mu \rangle &&= 17.5000 \quad .
\end{aligned}
$$

Together, the five independent coefficients fully describe a transverse isotropic and homogeneous material which elasticity-wise is equivalent to the rock compositions given in figure 5.2 in the static limit. Arranging them in tensor form yield

$$
\boldsymbol{C}_{analytical} = \begin{pmatrix}
40.4082 & 5.4082 & 2.8571 & 0.0000 & 0.0000 & 0.0000 \\
5.4082 & 40.4082 & 2.8571 & 0.0000 & 0.0000 & 0.0000 \\
2.8571 & 2.8571 & 20.0000 & 0.0000 & 0.0000 & 0.0000 \\
0.0000 & 0.0000 & 0.0000 & 8.5714 & 0.0000 & 0.0000 \\
0.0000 & 0.0000 & 0.0000 & 0.0000 & 8.5714 & 0.0000 \\
0.0000 & 0.0000 & 0.0000 & 0.0000 & 0.0000 & 17.5000
\end{pmatrix} \quad . \tag{5.2}
$$

Since the matrix above is the exact solution to the upscaling problem, it is used as a basis of comparison to the moduli that are generated by OPM-Upscaling. In the case of model 5.2a for example, the general method produces

$$
\boldsymbol{C}_{Upscaled} = \begin{pmatrix}
37.3810 & 4.7277 & 2.8563 & 0.0000 & 0.0000 & 0.0000 \\
4.7277 & 37.3810 & 2.8563 & 0.0000 & 0.0000 & 0.0000 \\
2.8563 & 2.8563 & 19.9999 & 0.0000 & 0.0000 & 0.0000 \\
0.0000 & 0.0000 & 0.0000 & 8.5705 & 0.0000 & 0.0000 \\
0.0000 & 0.0000 & 0.0000 & 0.0000 & 8.5705 & 0.0000 \\
00000 & 0.0000 & 0.0000 & 0.0000 & 0.0000 & 16.0742
\end{pmatrix} \quad , \tag{5.3}
$$

when the iterative solver is selected. By comparing the above modulus to the analytical solution given in (5.2), one can clearly see the inaccuracy of the code. To quantify this inaccuracy, a relative error term is computed by

$$
e = \frac{\|\boldsymbol{C}_{Upscaled} - \boldsymbol{C}_{Analytical}\|}{\|\boldsymbol{C}_{Analytical}\|} \tag{5.4}
$$

where $\|\cdot\|$ is the Frobenius norm,

$$
\|\boldsymbol{C}\| = \sqrt{\sum_{j=1}^{n}\sum_{k=1}^{n} c_{jk}^{2}} \quad .
$$

According to the definition above, the iterative upscaling solution to model 5.2a has an error of the order $O(10^{-2})$, or to be more precise $7.1107 \cdot 10^{-2}$. Similar calculations can naturally also be performed on the effective tensor obtained with the direct linear solver, and on the ones generated for model 5.2b. The relative error terms, with their corresponding upscaling times, are displayed in table 5.1.

Model	Cells	Iterative		Direct	
		Error	Time [sec]	Error	Time [sec]
5.2a	12000	$7.1107 \cdot 10^{-2}$	87.0193	$7.1107 \cdot 10^{-2}$	332.4850
5.2b	16000	$7.4575 \cdot 10^{-2}$	109.524	$7.4575 \cdot 10^{-2}$	46844.2000

Table 5.1: Relative errors and upscaling times associated with models in test group 1.

The first thing to notice is that the relative errors are all quite large. In fact, values of the order $O(10^{-2})$ look very pessimistic in terms of the general upscaling validity. Nevertheless, they are still not regarded as particularly disquieting. The code is actually known to be sensitive to large elastic contrasts. Since the two models of interest are created with a pronounced degree of that precise characteristic, some level of inaccuracy is expected. Luckily, the contrasts in a real reservoir are much smaller, and should not induce incorrectness like this. It is interesting though to see how "poor" results can get for relatively simple models like the ones illustrated in figure 5.2. The user should therefore always assess his/her material properties before truly accepting the general method's output.

Table 5.1 also demonstrates that the iterative linear solver, with a relative error tolerance of 10^{-8} or less, is just as accurate as the direct one for both models 5.2a and 5.2b. In addition, the duration of the upscaling process is much lower with the iterative solver. The latter actually turns out to be 3.8 and shockingly 428 times faster than the direct solver in the case of model 5.2a and model 5.2b, respectively. Before ultimately deciding which solver to use in later work, however, results from more test models should be evaluated.

5.2 Rotated layers

The two models shown in figure 5.3 represent, geometrically, the most general configuration of materials which is provided with an exact, analytical homogenization solution. Due to this fact, they are essential to any test that aims to verify an upscaling method that deals with general geometries. As one can see in figure 5.3, the models are not fancy at all, they are really just rotated versions of the ones presented in the previous section, with twenty and sixteen layers instead on ten. From left to right, the models are rotated 30.964 degrees clockwise and 26.656 degrees counter-clockwise, yielding different layer

inclination angles. Additionally, they are composed of materials with differing elastic properties. While model 5.3a is saturated with the isotropic parameters given in (5.1), the materials constituting model 5.3b are characterized by

$$
\begin{array}{rclrcl}
K_1 & = & 8 & \mu_1 & = & 2 \\
K_2 & = & 24 & \mu_2 & = & 6
\end{array}
$$

with K being the familiar bulk modulus. These values are definitely more realistic than those provided in (5.1), but still they portray two materials with a stiffness contrast so large, that it will rarely occur in the nature. For the purpose of the test, however, the values are more than good enough, and are included to create variations in the elastic input.

(a) $\gamma = 30.964°$ (b) $\gamma = -26.656°$
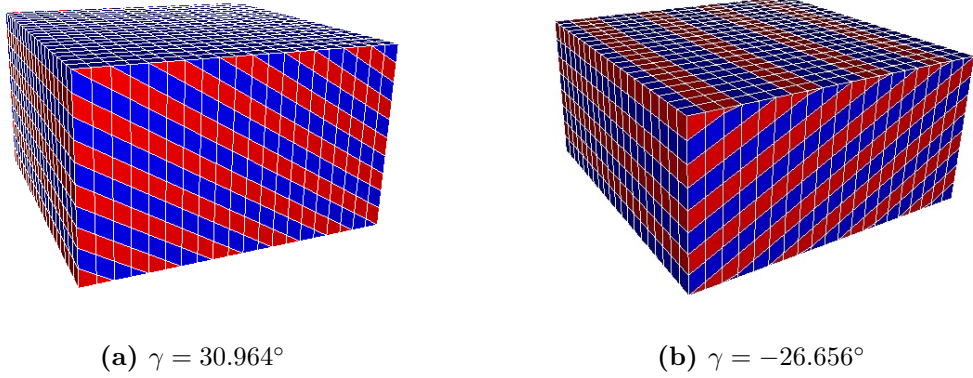
Figure 5.3: Periodic models with angled layering. They are both analogous to horizontally layered models which are rotated through coordinate transformations. (a) is rotated 30.964 degrees clockwise, while (b) is rotated 26.656 degrees counter-clockwise.

Analytical solutions, and hence measures of accuracy, can be found for each of the two models in figure 5.3 when periodic boundary conditions are employed. By appreciating this feature, one can see that both models have properties that fulfill the requirements of the Backus theory - if the coordinate systems are chosen to align with the inclination angles. As a consequence, one can simply calculate Backus averages for corresponding zero-angled models, and then apply coordinate transformations (see section 2.5), in order to change tensor basis and get true upscaling solutions. Model 5.3a, for example, is composed of the same materials as the ones illustrated in 5.2, with matching volume fractions. This means that an exact and effective modulus for the tilted model can be obtained by transforming the tensor given in (5.2). To get it, the coordinate system must be rotated 30.966 degrees counter-clockwise about the y-axis. In agreement with the theory presented in section 2.5, the tensor rotation is done by utilizing formula (2.34),

with a transformation matrix given as

$$
\boldsymbol{a} = \begin{pmatrix} cos\,(\gamma) & 0 & sin\,(\gamma) \\ 0 & 1 & 0 \\ -sin\,(\gamma) & 0 & cos\,(\gamma) \end{pmatrix} = \begin{pmatrix} 0.8575 & 0 & 0.5145 \\ 0 & 1 & 0 \\ -0.5145 & 0 & 0.8575 \end{pmatrix} \quad .
$$

The analytical solution to the homogenization of model 5.3a is hence found to be

$$
\boldsymbol{C}_{Analytical} = \begin{pmatrix} 31.03383 & 4.73289 & 6.82932 & 0.00000 & 6.62030 & 0.00000 \\ 4.73289 & 40.40816 & 3.53241 & 0.00000 & 1.12545 & 0.00000 \\ 6.82932 & 3.53241 & 21.42998 & 0.00000 & 2.38331 & 0.00000 \\ 0.00000 & 0.00000 & 0.00000 & 10.93487 & 0.00000 & 3.93908 \\ 6.62030 & 1.12545 & 2.38331 & 0.00000 & 12.54361 & 0.00000 \\ 0.00000 & 0.00000 & 0.00000 & 3.93908 & 0.00000 & 15.13655 \end{pmatrix} \quad .
$$

OPM-Upscaling, on the other hand, gives an effective tensor of

$$
\boldsymbol{C}_{Upscaled} = \begin{pmatrix} 31.02770 & 4.72655 & 6.82795 & 0.00000 & 6.61839 & 0.00000 \\ 4.72655 & 40.31910 & 3.52932 & 0.00000 & 1.12129 & 0.00000 \\ 6.82795 & 3.52932 & 21.42960 & 0.00000 & 2.38278 & 0.00000 \\ 0.00000 & 0.00000 & 0.00000 & 10.93000 & 0.00000 & 3.93172 \\ 6.61839 & 1.12129 & 2.38278 & 0.00000 & 12.54220 & 0.00000 \\ 0.00000 & 0.00000 & 0.00000 & 3.93172 & 0.00000 & 15.12370 \end{pmatrix}
$$

for both the iterative and direct linear solver. The relative upscaling errors associated with the tilted models, obtained from equation (5.4), are shown in table 5.2 together with the upscaling durations. Once more, the table is divided into two blocks; one for the direct and one for the iterative linear solver.

Model	Cells	Iterative		Direct	
		Error	Time [sec]	Error	Time [sec]
5.3a	3760	$8.7176 \cdot 10^{-4}$	39.1321	$8.7176 \cdot 10^{-4}$	15.1761
5.3b	4400	$1.4771 \cdot 10^{-3}$	30.3878	$1.4771 \cdot 10^{-3}$	19.7708

Table 5.2: Relative errors and upscaling times associated with models in test group 2.

As with the horizontally layered models, it turns out that the results of the general upscaling method do not depend on the type of linear solver chosen to address the homogenization of models 5.3a and 5.3b. Since the latter grids are much smaller, the upscaling times are a lot smaller too. A more interesting realization, however, is that the iterative linear solver works slower than the direct one. From table 5.2 one can see that the upscaling process endures approximately twice as long with the iterative solver. It is perhaps also worth noticing that model 5.3a gives a larger upscaling time with the

iterative solver than model 5.3b, even though it has fewer active cells. Consequently, the times cannot only be determined by the size of the grids. Beyond this, the relative errors are quite similar for the two tilted models, one being slightly larger than the other. An observant eye can see that model 5.3b is not hundred percent periodic. This is believed to be the main cause of its higher error term. Although the elastic contrasts between the materials are still very large, the accuracy is really not that bad for the tilted models. Now it remains to see how the code will handle irregularities and way bigger grids.

5.3 Complex geometries

All three models displayed in figure 5.4 are composed in ways that break the basic assumptions behind Backus' theory. Of this reason, they do not come with analytical solutions, and must hence be upscaled numerically with general methods such as the one described in this thesis. In contrast to the previous test models, which are very simple and unnaturally composed, the grids in this section and the next are much more representative to the ones actually used in reservoir modeling. Model 5.4a, however, is admittedly not very realistic in terms of outlining the subsurface, but is included for thoroughness. This particular design has created problems for earlier versions of the code, making it interesting to survey. Both model 5.4b and model 5.4c describe true facies, the first with a total number of cells much lower than the last. Again, the rigidities of the constituting materials are chosen to vary greatly in all models, to really put the general method to the test. The parameters which determine the elastic behavior of model 5.4a are this time given by

$$\begin{array}{llllll} K_1 & = & 8 & \mu_1 & = & 2 \\ K_2 & = & 96 & \mu_2 & = & 24 \\ K_3 & = & 96 & \mu_3 & = & 24 \end{array} \quad ,$$

while the equivalent elastic input to model 5.4b and model 5.4c yield

$$\begin{array}{llllll} K_1 = K_2 & = & 8 & \mu_1 = \mu_2 & = & 2 \\ K_3 = K_4 & = & 24 & \mu_3 = \mu_4 & = & 6 \\ K_5 = K_6 & = & 24 & \mu_5 = \mu_6 & = & 6 \end{array} \quad .$$

All materials constituting the models shown in figure 5.4 are set to have a density of 3 g/cm^3.

Since neither of the above models has an effective modulus that can be found analytically, no quantitative measures of accuracy can be calculated. Instead, the method's stability must be evaluated on the basis of bounds and common sense. The Voigt and Reuss bounds, presented in section 3.2, provide upper and lower limits to the true effective tensor and velocities. If the generated output is outside the bounds, one knows for a fact that the code is erroneous. If not, the upscaled tensor is somewhat correct, but with an uncertain accuracy. As long as the effective parameters stay within the limits, the
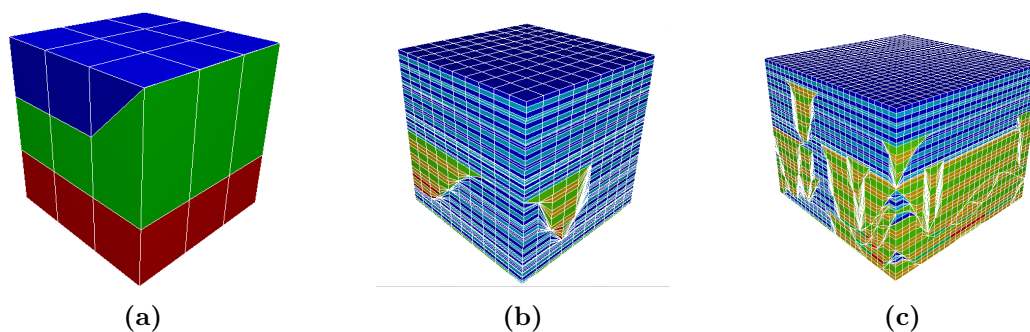
(a)   **(b)**   **(c)**

Figure 5.4: Models with general geometries and irregular grid designs. While (a) is simple and unrealistic model, (b) and (c) are parts of facies models that portray the subsurface.

reliability of the output can be determined by the distance between the Voigt and Reuss bounds. The narrower the gap, the more certain one can be that the method provides good solutions. With the technique introduced in chapter 4, the upscaled tensors of model group 3 and their corresponding Voigt and Reuss bounds are plotted together in figure 5.5. Modulus 5.5*a*, 5.5*b* and 5.5*c* belong to grid 5.4*a*, 5.4*b* and 5.4*c*, respectively.

When it comes to upscaling durations, the iterative solver is faster than the direct solver for both models 5.4*b* and 5.4*c*, but slower for model 5.4*a*. All times, except one, can be found in table 5.3. The upscaling of model 5.4*c*, with the direct linear solver, turned out to be too time consuming, and was therefore aborted. The table cell associated with this process is left blank. Finally, it should also be mentioned that the two linear solvers yield exactly the same effective moduli.

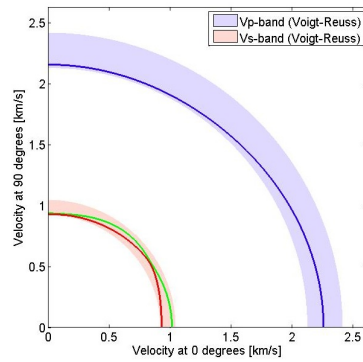| Model	Cells	Iterative		Direct	
		Error	Time [sec]	Error	Time [sec]
5.4*a*	27	–	0.1731	–	0.0199
5.4*b*	7104	–	175.6470	–	398.1230
5.4*c*	43252	–	1780.6000	–	–

Table 5.3: Relative errors and upscaling times associated with models in group 3.
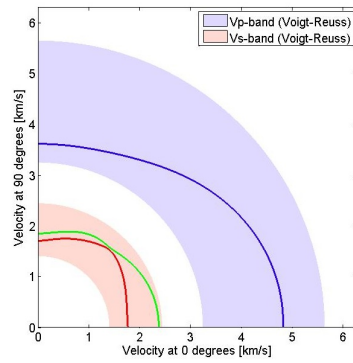
(a)
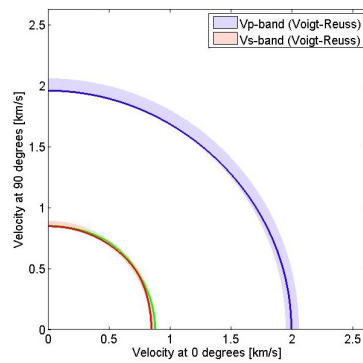
(b)

(c)

Figure 5.5: Pictorial representations of the effective tensors obtained for the models displayed in figure 5.4. The pale blue and pink areas are Voigt-Reuss bands that confine the tensor's corresponding P- and S-wave velocities, respectively. (a) visualizes the upscaled moduli of model 5.4*a*, (b) model 5.4*b* and (c) model 5.4*c*.

5.4 Applicable reservoir model

The final grid included in this upscaling test is special in the way that it is a chop of a model which actually will be utilized in later work, as a part contributing to the complete reservoir model that is to be generated for the topical field. In terms of the grid design, the facies model shown in figure 5.6 is not very different from those that are presented in the previous section. They are obviously all representative for the grids employed in the branch of reservoir modeling. However, at this stage of the analysis, the elastic parameters are given more or less realistic values. This brings the final test model much closer to the ones that are to be upscaled in the remaining study of this thesis. It is therefore essential, now more than ever, that the method behaves properly. At the time of the testing, data on some important rock properties was yet to be found. Of this reason, the elastic input given to model 5.6 is close, but not entirely equal to the input which is employed later. The elastic parameters and densities utilized in this final test case are hence computed through porosity data only, in a way that is carefully explained in chapter 7. The physical properties assigned to the twelve isotropic rock types constituting model 5.6 are given i table 5.4.

Rock#	K [GPa]	μ [GPa]	ρ [g/cm^3]
1	19.960925	12.976771	2.315707
2	26.442177	18.511858	2.475708
3	15.313523	9.194773	2.179267
4	21.150827	13.972976	2.347329
5	17.950642	11.317943	2.259451
6	22.703470	15.287361	2.386937
7	19.330120	12.452842	2.298456
8	21.523124	14.286694	2.356991
9	15.125953	9.046339	2.173243
10	28.312623	20.152864	2.517123
11	25.153301	17.391428	2.446068
12	17.037974	10.575857	2.232594

Table 5.4: Elasticity and density data associated with the different rock types in facies model 5.6.

The upscaled tensor, visualized in figure 5.7, is both within and closely restrained by the upper Voigt and lower Reuss bounds. Accordingly, the code appears to have produced an accurate effective modulus for model 5.6. This is indeed a very promising result in terms of the method's usability. However, with the bounds located so close to each other, one may wonder whether it is necessary to geologically model elastic properties at all - especially when the elasticity contrasts are small. In the case of model 5.6, it seems

like a volume weighted upscaling (e.g. Voigt-Reuss-Hill) would have been more than adequate. After all, one of the bounds could have been used as an upscaling solution, with maximum possible P- and S-wave velocity errors yielding $V_P^V - V_P^R = 0,0413\ km/s$ and $V_S^V - V_S^R = 0.0308\ km/s$, respectively. This question, however, is not for this thesis to answer.
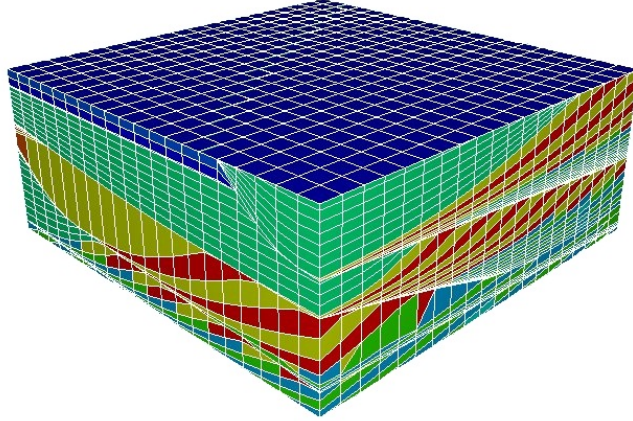

Figure 5.6: A piece of a facies model that is to be used in the later work. It depicts a part of a channel belt that can be found in the reservoir of interest.

As expected by now, the iterative and direct solvers propose identical solutions to the homogenization of model 5.6, with the latter being the slowest. From table 5.5, it can be seen that the iterative solver finishes approximately twice as fast as the direct one. The upscaling durations themselves, however, are not very representative for the models utilized later in this thesis. Since model 5.6 is only a small chop, or piece, of a full facies model, it is expected to be upscaled in a much shorter time. While the size of model 5.6 is approximately 8 MB, a full facies model can easily reach 500 MB. This will obviously affect the run time of the method greatly.

Model	Cells	Iterative		Direct	
		Error	Time [sec]	Error	Time [sec]
5.6	14007	–	222.62	–	468.998

Table 5.5: Relative errors and upscaling times associated with the model in group 4.

Given all the satisfying results associated with the above analysis, it appears appropriate to report the general upscaling method fit for duty. Even though some of the simple material compositions caused the code to produce output errors of orders up to $O(10^{-2})$,

the inaccuracy was never alarming. The code is, as pointed out, sensitive to major elasticity contrasts. With physical properties fluctuating widely from layer to layer, the first models were anticipated to give some error. For practical purposes, relative upscaling errors of the orders $O(10^{-3})$ and $O(10^{-4})$ are of little relevance, as the uncertainty of for example seismic data or velocity measurements are likely to be greater. Complementing the quantitative information on accuracy obtained from the Backus-supported models, the tensor visualizations of all the irregular and lifelike grids do neither indicate any evident flaws in the code. In fact, after comparing the upscaled elastic moduli to the Voigt and Reuss bounds, the output from the general method looks even more reliable. The upscaling code is consequently considered safe to use throughout this thesis and in future work involving geological modeling of elasticity.

On the issue regarding which linear solver to employ, the test is relatively clear. In all eight cases, the direct and iterative (with a tolerance of 10^{-8}) linear solvers give identical effective moduli. There is hence no reason to pick one over the other in terms of accuracy. The main difference between the two, however, lies in the time (and memory) consumption. As proven by the various upscalings, the iterative solver is much faster than the direct one on large grids, while slower on the small. The choice should therefore always reflect the size of the grids. Since all feasible reservoir models are huge compared to the ones benefiting from the direct way of solving linear systems, the iterative solver is preferred in the entire study. Although this option will reduce the upscaling times drastically, they will by all means remain large. Some of the facies models will undoubtedly upscale for several days. The next chapter aims to find a method to decrease the upscaling duration further.
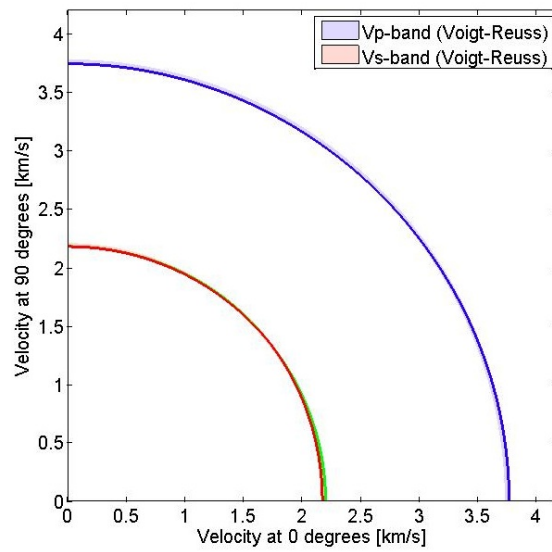
Figure 5.7: Pictorial representations of the effective tensors obtained for the model displayed in figure 5.6. The pale blue and pink areas are Voigt-Reuss bands that confine the tensor's corresponding P- and S-wave velocities, respectively.

Chapter 6

Model partitioning and run-time reduction

The run times of different upscaling jobs can sometimes be unbearable. In most cases, at any given scale, the grids to be homogenized are either huge, come in great numbers, or are both large and many at the same time. The latter situation is certainly the most common. Take for example the main upscaling process of this study. The goal is to eventually construct a complete model of the reservoir in question by applying upscaled facies models as building bricks. There are 62 of these models and each of them is typically upscaled in a day or two, depending on the grid size. Since the total time usage exceeds weeks, it would be nice to have a way of reducing it. The basic idea is therefore to chop the full facies models into smaller pieces, upscale them separately, and finally calculate an average effective modulus, which in principle could be used as a substitute for the elastic tensor obtained from a full-model upscaling.
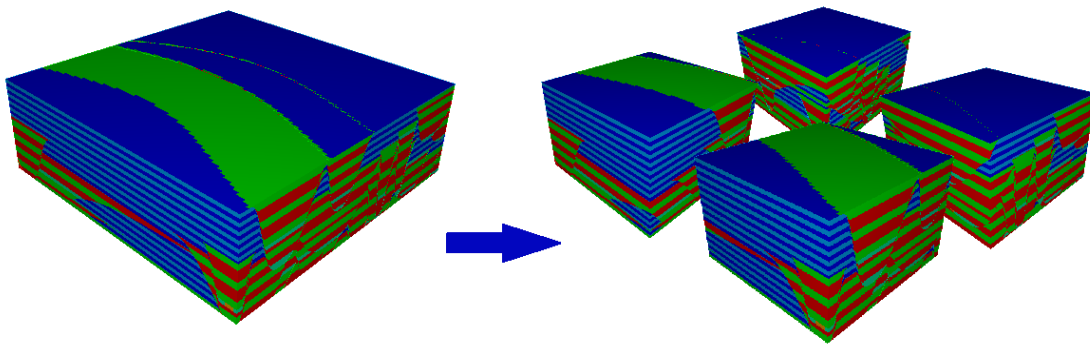
Figure 6.1: The concept of model-chopping. The idea is to lower upscaling-durations by dividing full reservoir models into pieces. These should be upscaled separately to provide effective tensors that later can be combined with simple averaging.

A problem with this approach, however, is that the chops may be poor REVs, meaning that they do not properly represent the whole model. Typically, the representativeness will decrease with both the elasticity contrasts in the input and the relative smallness of the chops. The last mentioned feature can easily be seen in figure 6.1. If the full facies model on the left hand side is to be cut into very small pieces, it is possible that some submodels will contain background materials (blue) only, while others exclusively channel rocks (red and green). These will obviously not have representative effective tensors. On the other hand, the upscaled modulus of a realistic facies model appears to depend more on relative volume weights than geometry, giving the arithmetic average a chance to balance out some of the inequalities related to the submodels. To examine the method's usability and to find out what is an appropriate number of partitions, the model shown in figure 6.1 is chopped into 4, 6, 9, 16 and 25 pieces, successively. The model is always cut like a cake (see figure 6.1), never sliced vertically. In each case, the average effective moduli are compared to the upscaled full-model modulus both in their natural matrix form and as corresponding velocities. First, however, the temporal aspect of the method is investigated.

To get an idea on how much time it is possible to save through the application of model subdivision, the upscaling times are registered for all the involved grids. With this on hand, one can easily find the total upscaling duration associated with each chop-scenario. As the upscalings were done on a single processor core, one after the other, the aggregate times are just simple summations. A plot of them is provided in figure 6.2 to increase the comparability. The blue bars represent true time usage, while the reds display expected, but fictitious, time spending connected to hepta-core (8-core) performance. At the moment, one single upscaling job cannot be executed on several cores simultaniously. There is, however, nothing that prevents one from running *multiple* upscalings at the same time. By utilizing eight cores, the total upscaling durations can in theory be reduced to approximately 13 percent of their original lengths, as long as the number of chops is larger than the number of cores. The partitions that are smaller can obviously not utilize all eight. The upscaling time of the full model for example, displayed farthest to the left in the plot, will not change at all, while the time associated with four chops is only divided by four. Finally, it must be emphasized that the red bars are only rough estimates. There is no reason to believe that the upscaling time of a model is linearly related to the grid size.

Much more important than the red bars, are the blue ones. Figure 6.2 clearly shows that the time consumption falls drastically as a consequence of chopping. By partitioning the complete facies model into four submodels, the total upscaling duration shrinks with almost 50 percent, from 486 to 253 minutes. Since the total time continues to decrease, but with a lower rate, the relationship between grid size and upscaling time can indeed not be linear. This relation, exponential or not, implies that the chopping procedure has an increasing effect with size. While the leftmost model in figure 6.1 "only" consists of 352324 active cells, some facies models might approach a million cells. With plot 6.2

in mind, it appears obvious that model subdivision can be utilized advantageously as a mean to lower time consumption in upscaling, contingent of course upon the method's validity.
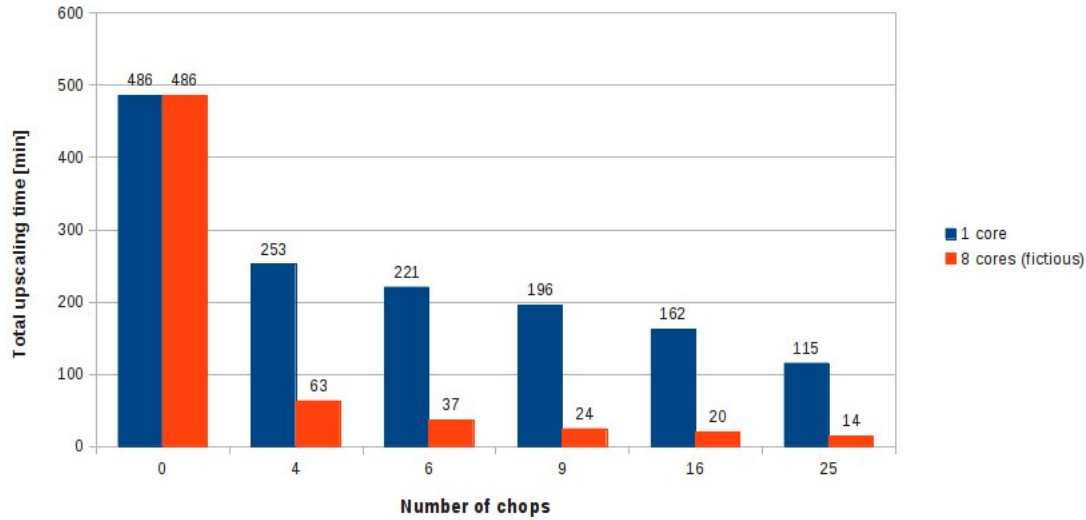

Figure 6.2: Upscaling times associated with different chop-scenarios. The blue bars represent actual run-times obtained with one CPU (subsequent upscaling). The red bars represent estimates of run-times when 8 processes are allowed to be executed simultaniously. As one can see, a lot of time can be saved both with model-partitioning and parallell execution. The leftmost bars are associated with the complete reservoir model.

Figure 6.3 displays upscaling times with respect to active cells in the submodels. Since the range of cells is limited to approximately 90000, and since the data is sparse in some areas, very little can be said for certain about the duration-size relationship. At first glance the data seems to sketch a linear curve. However, if one looks very carefully, one might see a slight increase in slope with the number of cells. This is in alignment with the above plot. According to figure 6.2, the growth rate of the slope will mainly accelerate at grids larger than the ones plotted in figure 6.3. Furthermore, the scatter in the plot suggests that there are other factors influencing the upscaling times in addition to the grid size. Especially one submodel with 40000 active cells is far off its expected value.

In agreement with the results obtained in chapter 5, all models, complete and chopped out, were upscaled with the iterative linear solver set. Beyond that, only default values were chosen.
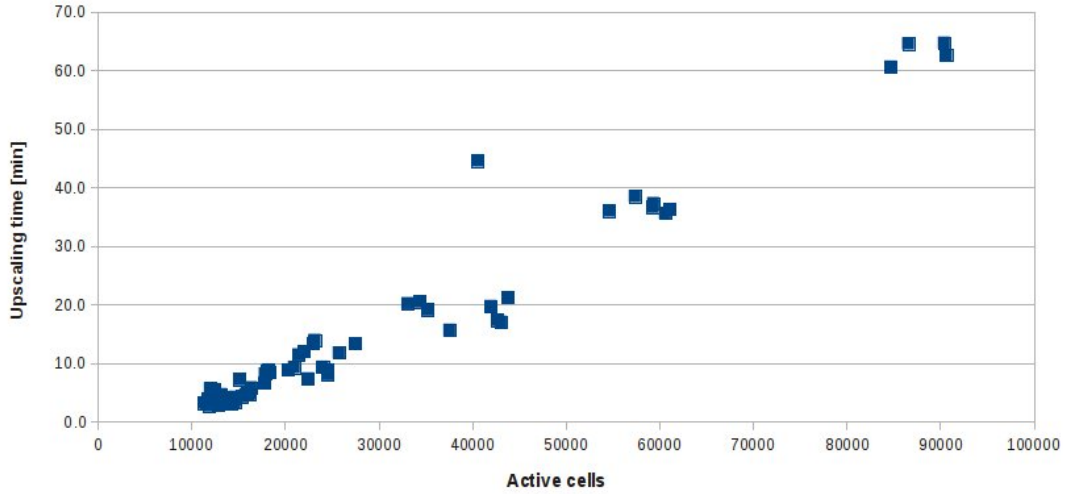
Figure 6.3: Upscaling times in minutes plotted against the number of active cells in the various submodels. The run-times increase sharply with the grid size.

Before making quantitative measures on accuracy, it is interesting to see how the effective moduli change from submodel to submodel within the different chop-scenarios. This will not only provide a deeper understanding of the average values and their origins, but also demonstrate the representativeness of each chop. As known by now, a chop is an appropriate REV merely when the discrepancy between the upscaled submodel tensor and the full-model tensor is small. To be able to examine the elastic properties of the individual partitions simultaneously, corresponding P- and S-velocities are computed and plotted as seen in figure 6.4. The blue points represent submodels that are generated from chopping the full grid into 25 pieces, the red points from chopping the full grid into 16 pieces, and so on. Additionally, V_P and V_S lines belonging to the complete model are included for reference. The number of data points in each series obviously reflects the number of model partitions, which is the reason why the data is mainly gathered towards the left part of the plots. Since the horizontal axis has no virtual meaning, the velocities could just as well have been placed anywhere else along it. In order to keep the figures simple and two-dimensional, plot 6.4a and plot 6.4b display vertical velocities only. Irrespective of this, there is really no need to show speeds in further directions. By comparing the two figures, one realizes that the full model must be very close to isotropic. The positive correlation implies that the vertical V_P/V_S-ratio is almost identical in all submodels, which in turn indicates non-directional velocities. This statement, moreover, is supported both by figure 6.5, which will be explained later, and plots similar to 6.4a and 6.4b made for horizontal velocities.

The first thing to notice in figures 6.4a and 6.4b is the prominent oscillations that appear to be amplified by the number of model partitions, or rather the size of the grids. As

58
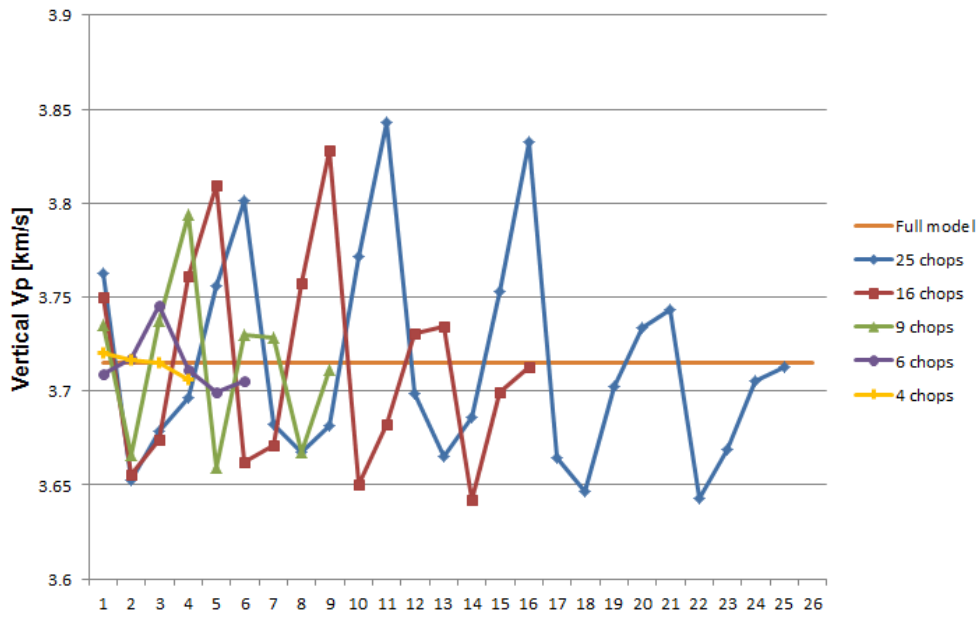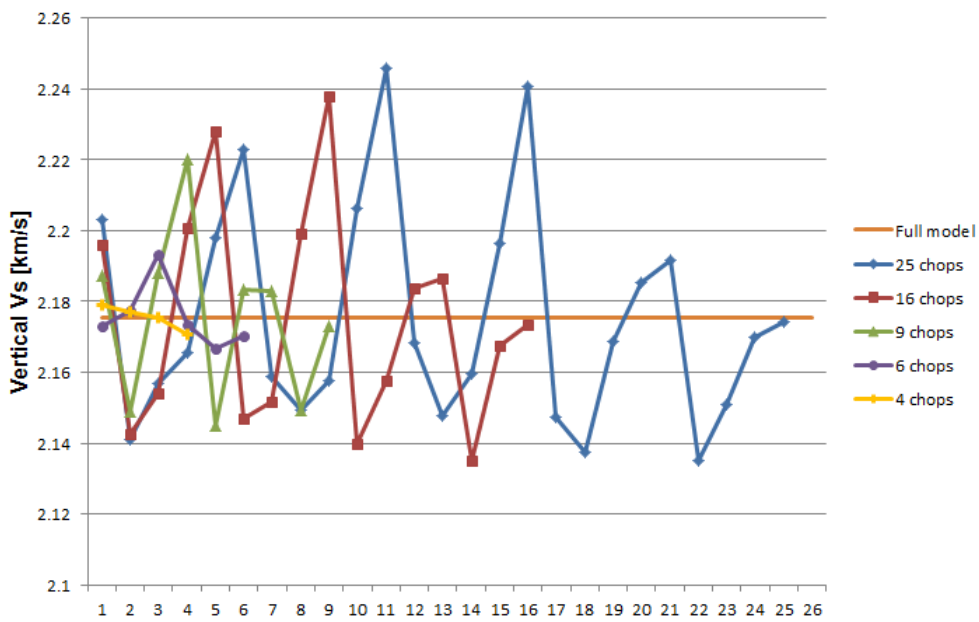
(a) P-wave velocity

(b) S-wave velocity

Figure 6.4: Vertical V_P (a) and V_S (b) plotted for the different chops. The horizontal line in each figure is associated with the full model. The velocities appear to fluctuate about the latter line. Additionally, the magnitude of the variations increase with the number of chops.

explained earlier in this chapter, the magnitude of the velocity variations, or amplitudes, are expected to increase with the smallness of the chops. When submodels get larger, they are more likely to have effective properties that resemble those of the complete model. Consequently, it is only natural that the yellow curves, which correspond to the largest grids, are flatter than the purple, the purple curves are flatter than greens, and so forth. The cyclic behavior of the data, however, is believed to be more of a coincidence than a typical model feature. As the channel belt shown in figure 6.1 winds its way through the middle of the model in roughly one direction, it is not difficult to imagine why the velocities oscillate as they do. The submodels are simply plotted in sequences that are more or less analogous with plotting successive cross-sections. The troughs correspond to chops that fetch large parts of the channel belt (in the middle of a cross-section), while the crests correspond to chops that do not. In other words, the wave-like patterns seen in figure 6.4 are attributed to the content of the complete model and the data sorting only, and are not patterns that should be anticipated for all reservoir models. Lastly, figure 6.4 shows encouraging results in terms of computing sufficiently accurate average moduli. At first sight, one immediately discovers that the full model's vertical velocities are relatively well preserved in all submodels constituting the yellow data series. Since the upscaled tensors of the four chops all appear to individually represent the complete model in a good way, the average tensor must obviously do too. The other partitions, however, vary much more in velocities. Fortunately, the velocities associated with each scenario fluctuate about the reference line. This allows the average moduli to be more or less precise, even though some of the submodels seem to be poor REVs.

To quantify the discrepancy between the effective average properties and the ones obtained for the complete model, relative differences in P-wave velocity, S-wave velocity, density and elastic modulus are computed for all cut-scenarios. With reference values provided by the full-model upscaling, the differences are given by

$$\text{Relative difference} = \frac{|p_{avg} - p_{full}|}{p_{full}}$$

for any of the scalar properties, $p = V_P, V_S, \rho$, and

$$\text{Relative difference} = \frac{\|\boldsymbol{C}_{avg} - \boldsymbol{C}_{full}\|_{Frobenius}}{\|\boldsymbol{C}_{full}\|_{Frobenius}}$$

for the elastic tensor matrices. Again, $\|\cdot\|_{Frobenius}$ is the Frobenius norm. The error terms obtained for each model partition are all given in table 6.1, along with a few extra measures. According to column, AVG is either the average V_P or V_S value, while STD is the standard deviation. The vertical P-wave velocity, the vertical S-wave velocity and the density of the complete model yield 3.7147 km/s, 2.1756 km/s and 2.2317 g/km^3, respectively.

Chops	Vertical V_P (km/s)			Vertical V_S (km/s)			$\dfrac{\|C_{avg}-C_{full}\|}{\|C_{full}\|}$	$\dfrac{|\rho_{avg}-\rho_{full}|}{\rho_{full}}$
	AVG	STD	Rel.diff	AVG	STD	Rel.diff		
4	3.7147	0.0061	4.5091e-06	2.1756	0.0036	1.6547e-05	1.0550e-04	1.4e-06
6	3.7147	0.0162	2.0953e-05	2.1758	0.0092	7.1704e-05	1.5150e-04	3.8e-05
9	3.7142	0.0437	1.1821e-04	2.1754	0.0243	1.0654e-04	7.3640e-04	3.1e-06
16	3.7139	0.0567	2.1694e-04	2.1751	0.0313	2.2319e-04	1.3908e-03	2.4e-06
25	3.7139	0.0563	2.0925e-04	2.1752	0.0310	1.9568e-04	1.3020e-03	6.5e-06

**Table 6.1:** Statistics regarding the accuracy of the various model partitions.

The quantitative results shown in table 6.1 are truly sensational. Not only does the method work relatively well on the largest chops, as predicted, it actually provides incredibly accurate tensors, velocities and densities for all the different scenarios. Even with the variations displayed in figure 6.4, the relative errors in average vertical V_P and V_S do never exceed $O(10^{-4})$. As the uncertainties connected to model input, upscaling and acoustic measurements are large compared to this, the average velocities are more than acceptable. Furthermore, one can observe a strong correlation between accuracy and standard deviation. Since the latter is a quantitative measure of the fluctuations seen in figure 6.4, the error terms expectedly increase with the number of chops. The relative difference between the average and the full-model tensor must necessarily also be very small for each partition, in order to generate such accurate mean velocities. Ranging from the orders $O(10^{-4})$ to $O(10^{-3})$, the errors of the average moduli prove that it is possible to substitute the original tensor without losing a lot of generality.

To support the data given in table 6.1, the tensors are all visualized and plotted together in figure 6.5, according to section 4.1. As the moduli are really close to isotropic and also virtually identical, the corresponding P- and S-wave velocities are this time displayed in two separate plots. Without looking any further, one can easily be fooled into thinking that the velocity graphs are very curvaceous. This, however, is simply an artifact created by the scale. If the velocities were to be plotted normally, in one figure, they would appear almost completely flat and reveal nothing but the isotropic nature of the tensors. Instead, it is now possible to compare the various average moduli with each other, and examine the directionality of their precisions. In both figures 6.5a and 6.5b the colored lines belong to the various average tensors, while the two black ones are associated with the full-model moduli. Consequently, the relative differences shown in table 6.1's eight column reflect how well the different averages mimic the black lines over all propagation angles. As discussed in chapter 4, the tensor representation below shows corresponding velocities only in one azimuthal plane. One will therefore not be able to fully envision the tensors. In this particular case, however, the shape of the curves suggests some kind of weak horizontal layering in the model. This feature is of course drowning in the much more prominent isotropic symmetry, but will give more or less equal velocity plots for all vertical cross-sections (azimuths).

Since the curves follow each other closely in figure 6.5a, the method's accuracy associated with the P-wave velocity is only marginally affected by the number of upscaled chops entering into the corresponding average tensor. Additionally, the magnitude of the relative differences in V_P provided by table 6.1 looks fairly representative for all kinds of wave propagations, not merely the vertical. The relative V_P-errors are hence likely to remain below $O(10^{-4})$ regardless of direction. If one takes a closer look at the plot, one will certainly discover that the green line (4 chops) is not always the one closest to the black. Horizontally, at 90 degrees, the average tensors obtained for 6 and 9 submodels give greater accuracy than the one obtained for 4. Owing to this fact, the relative differences will somewhat change with measuring angle. Unlike table 6.1, which only considers the primary S-wave, figure 6.5b displays both V_{SH} and V_{SV} as functions of propagation angle. Because the horizontally polarized S-wave moves at speeds determined by the curve with one peak, it is obviously the type of wave that provides the greatest amount of inaccuracy to the chopping-method. This makes sense when one realize that the space between the reference line and especially the lines corresponding to the three largest model partitions is much more conspicuous in V_{SH} than in V_P or V_{SV}. When it comes to the vertically polarized shear waves, however, the directional velocities seem to line up pretty well with the full-model obtained velocity. Similar to V_P and V_{SH}, the V_{SV}-accuracy associated with the different scenarios falls just a little bit near the extrema, but not as significant. Since the relative differences in shear wave velocity are computed with the first arriving S-waves, their values will depend on the wave propagation direction. As seen in figure 6.5b, the precisions will be lower between 55 and 125 degrees, where V_{SH} is the chosen S-wave velocity. Nonetheless, the scales in both plot 6.5a and plot 6.5b are extremely small, making the inaccuracies imperceptible to a great extent.

Considering the great accuracy provided by the average tensors, the chopping-method in question appears to be applicable. It turns out that a complete facies model, with realistic input, can be cut into as much as 25 pieces and still, after averaging the separate upscaling results, yield an effective tensor remarkably close to the original one. By doing this, it is possible to save a lot of time on large upscaling projects, including this study. As both the accuracy and the time consumption drops with the number of model partitions, one has to find some sort of balance. The results show that the benefit related to time-saving gradually decreases as the number of chops grows. Consequently, it may be wise to stick to a modest number, like 4 or 6. As mentioned earlier, also the model input and geometry is likely to affect the accuracy of the method. With huge elasticity contrasts, the averages might break down as representative tensors. In that case, one can try to rebuild the complete model with much larger cells, each corresponding to a homogenized partition, and then finally upscale the entire unit in one process. Since this approach only has one extra upscaling, it will certainly shorten the time usage too. The latter method, however, is neither tested nor employed in this study. Irrespective of the method's apparent accuracy, one should always aspire to perform upscaling on

full models. By averaging elastic tensors obtained for chops, one loses both geometrical information and control over the final output. Model partitioning is consequently only regarded as a backup plan.
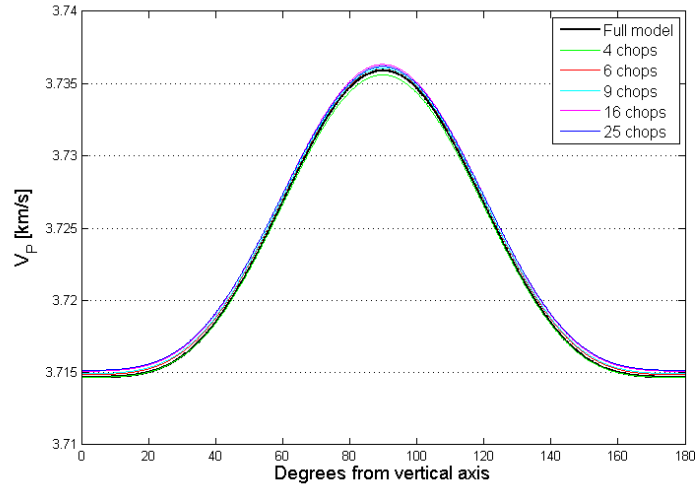
(a) P-wave velocity
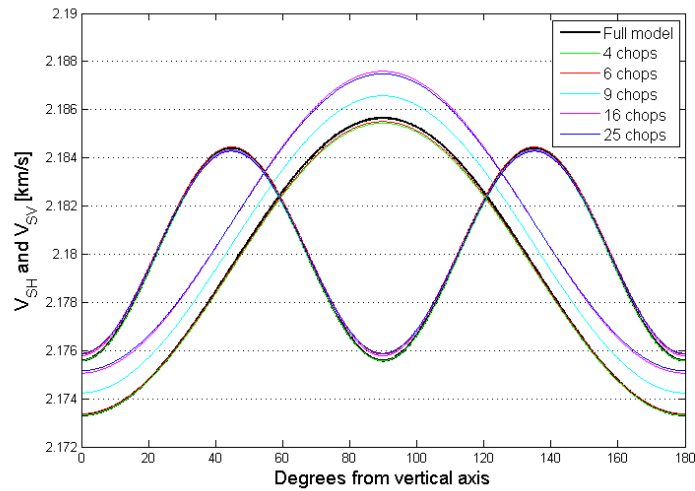
(b) S-wave velocities

Figure 6.5: Visualization of the average tensors. Both V_P (a) and V_S (b) are plotted against angle from the vertical z-axis. The curves with only one peak in plot (b) are associated with V_{SH}, while the ones with two are associated with V_{SV}. The black curves represent the full model tensor. As one can see, the average tensors are very accurate.

Chapter 7

Empirical elastic properties

A very important and time consuming part of this study has been to find realistic and suitable elastic input to the reservoir models. In order to appropriately compare real seismic data and well measurements to corresponding data generated from upscaling, it is absolutely crucial to get elastic properties right. Ideally, accurate elastic measurements on all constituents of the entire reservoir, with their in situ conditions, should be on hand. This, however, is far from the reality. Simplified elastic input, which one can only hope represent the complex ground respectably, must be derived from limited sources of information, such as well logs, core samples and/or forward modeling. In this thesis, the basis of the main upscaling process consists of several models similar to the one illustrated in figure 7.1. This particular grid is $13m$ high and $500m$ wide, and describes a channel belt. While the green and red cells form the reservoir sands, the light and dark blue constitute the background material. Each cell corresponds to a lithofacies model with a given elastic characteristic, which is theoretically described by parameters that must be rightfully determined and given to the larger model as input. As a consequence of elastic parameter deficiency, the material in each cell is forced to be both isotropic and homogeneous. The upcoming chapter will therefore address the problem of finding *isotropic* parameters, or corresponding velocities, that accurately describe the various lithofacies in the reservoir.

The number one reasonable thing to do when in need of model input, is to look at laboratory measurements performed on the actual reservoir of interest. Core samples, which are gathered during drilling, often provide data on V_P, V_S, density, porosity, clay content and many other properties. However, there is no guarantee that the data is representative for the reservoir and the different rock types. In the course of its journey from the deep subsurface to the laboratory work top, a sample may experience drastic changes in composition that cannot be reversed by reapplying reservoir conditions in experiments. Additionally, badly executed measurements can ruin parts of the data too. As a consequence, the core plug data should always be carefully examined before put to use. For the reservoir of interest, however, the issue is not bad data, but shortage of it. As it turns out, laboratory data is not available in this study.
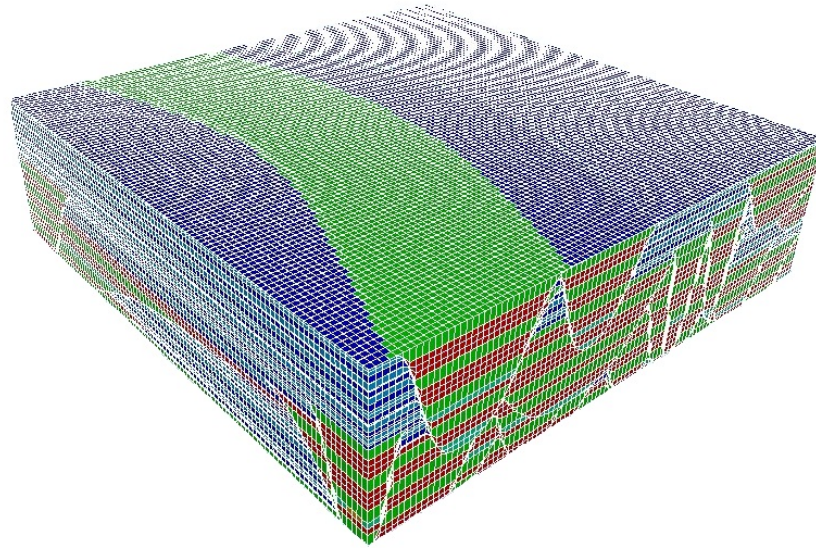
Figure 7.1: Model of a channel belt. Each cell has to be assigned elastic parameters.

In the absence of sufficient core data from the reservoir, acoustic data representing the various lithofacies in the subsurface must be found elsewhere. One obvious solution is to employ core measurements and velocity relations that have been gathered and computed for other purposes and at other locations. As long as lithology and conditions correspond tolerably to that of the reservoir, it should not be a problem to utilize this kind of "stand-in" data. The nature, however, is not always as tractable as one wants it to be. Accordingly, one can, if unfortunate, end up searching a long time for decent input. In this chapter, three different and approved velocity models, supported by their own datasets of rock samples, are presented. Which model is the most representative for the reservoir, if any, is examined in chapter 9.

7.1 Han's acoustic data on sedimentary rocks

In 1986, Han set up a comprehensive experiment examining the effects of porosity and clay content on acoustic properties in sandstones and unconsolidated sediments. By measuring ultrasonic compressional and shear velocities of 80 rock samples, he gathered one of the largest collections of acoustic data on sedimentary rocks that are available for public use today. In accordance with Han's objective, a wide range of sandstones, with varying clay content and porosity, were investigated in a controlled laboratory environment. Of the total number of samples, thirty-five were borehole cores with various degrees of consolidation, thirty-five were well-consolidated samples from quarries with various degrees of clay content, and ten were tight gas sandstones with low porosities.

Consequently, the porosity in Han's data ranges from 2 to 30 percent and the clay content by volume fraction from 0 to 50 percent. All samples were rinsed, kept at least a month in room-dry conditions, and vacuum oven-dried prior to the measuring. The acoustic experiments were then carried out in dry state, and later repeated with full water saturation. Apparently, water was substituted with brine in some samples with high clay content. This, however, did not change velocities. In the laboratory, the confining pressure and the pore pressure can be controlled separately during the tests to simulate proper reservoir conditions. The pore pressure was limited to 1 MPa by Han, while the confining pressure, which corresponds to the overburden pressure in a reservoir, was altered throughout the experiment. V_P, V_S and porosity data exist for several confining pressures between 5 MPa and 40 MPa - the largest corresponding to pressure conditions at depths greater than $2000m$. All of this, and more on the experiment setup, can be found in [16].

Since the reservoir of current interest is located at depths between $2300m$ and $2900m$, it is only natural to use Han data gathered at a confining pressure of 40 MPa in this study. Wave velocities of rocks tend to increase with the overburden pressure, until a certain pressure point is reached. At higher pressures, the velocity curves typically flatten out, giving more or less constant acoustic data. By choosing a confining pressure of 40 MPa, the "pressure independent" velocity level is hopefully found. This will presumably increase the reliability of the data. A velocity plot of two arbitrary samples, with respect to confining pressure, can be seen in figure 7.2. It should also be mentioned that the Han measurements selected for employment in this thesis are the ones done on water saturated rocks with a pore pressure of 1 MPa.
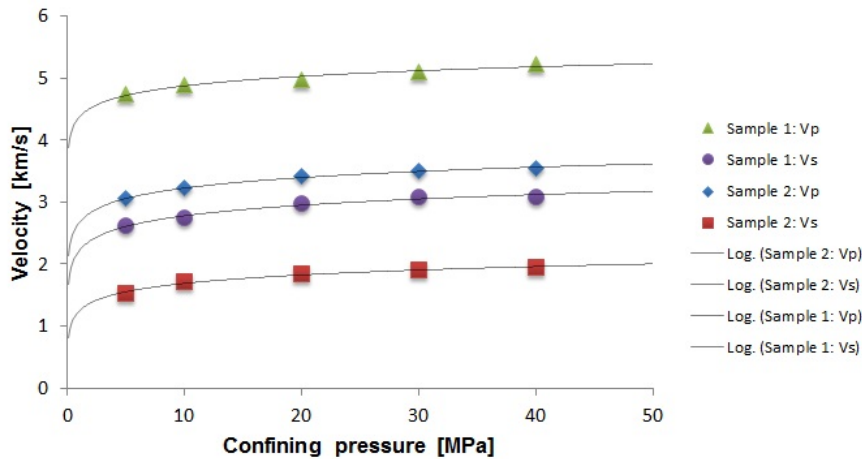

Figure 7.2: Velocities (V_P and V_S) versus confining pressure for two arbitrary Han samples. The black curves, which illustrate conceptual velocity functions, are logarithmic regressions of the measurements.

In the quest of finding good input parameters to the reservoir models, the acoustic Han data is plotted with respect to porosity, and eventually also to clay content. There are three well-connected reasons for this: (1) The elastic measurements done on core samples are not sufficiently many in number. (2) Han's research concludes that wave velocities depend strongly on the porosity and clay content of the sandstones. In fact, Han's study suggests that porosity is the main factor determining velocities, and that the effects of clay content on velocities are approximately 30 percent of the porosity effect on V_P and 40 percent on V_S. (3) Representative porosity and clay content data already exist for the various lithofacies assumed present in the reservoir. As mentioned before, the large-scale properties of sedimentary rocks are determined by geological features at even the smallest scale, and hence information from the smallest levels must be accounted for in order to produce useable model input. Up until now, there has unfortunately been no acceptable way of upscaling elastic properties from the pore scale to the lithofacies (core) scale and further. Consequently, without decent laboratory measurements, good velocity data representative for the reservoir's lithofacies could not be obtained. However, one has been able to upscale other properties, such as porosity and clay content, for a while. This means that the upscaled porosity and clay content parameters, which originate from the smallest scale, are much more reliable. With this in mind, Statoil has gathered effective porosity and clay content data on the field's lithofacies. The main idea is therefor to utilize Han's acoustic measurements, or similar data, to estimate velocities and densities from the known porosities and clay contents. This will provide elastic input to the reservoir models.

The plots provided in figure 7.3 show how P- and S-wave velocities in Han's samples relate to porosity, irrespective of clay content. To supplement the real data, linear trend lines with their equations and correlation factors are displayed on both charts. The correlation term, R^2, which actually is the square of the correlation coefficient, serves as a measure of the fit between the line and the experimental data. A value close to zero attributes to an inaccurate data description by the trend line, while a value close to one attributes to an accurate description. Of this reason, a value near one is desirable.

From the looks of figure 7.3, it is quite clear that V_P and V_S are strongly affected by the porosity, and that they both *decrease* linearly with the amount of pore space. This is because lower porosities yield stiffer rocks. At the time of the upscaling-code testing, clay content data on the reservoir's lithofacies was still not found, leaving porosity the only established model input. Owing to the fact that a couple of tests had to be done on more or less realistic models, a way of transforming porosity data to elastic data, without taking other parameters into account, was needed. The equations displayed in figure 7.3 were hence directly utilized to generate test data. As seen in the figure, the correlation between trend lines and actual data is without doubt conspicuous, but has also room for improvement. Although linear V_P and V_S functions, with respective correlation factors of 0.6076 and 0.4614, are good enough for tests, they will be inadequate to the real experiment in this thesis. It is therefore necessary to introduce the other

mentioned velocity determinant - clay content - when plotting. This will surely heighten the correlation coefficients and ensure better quality input to the reservoir models.
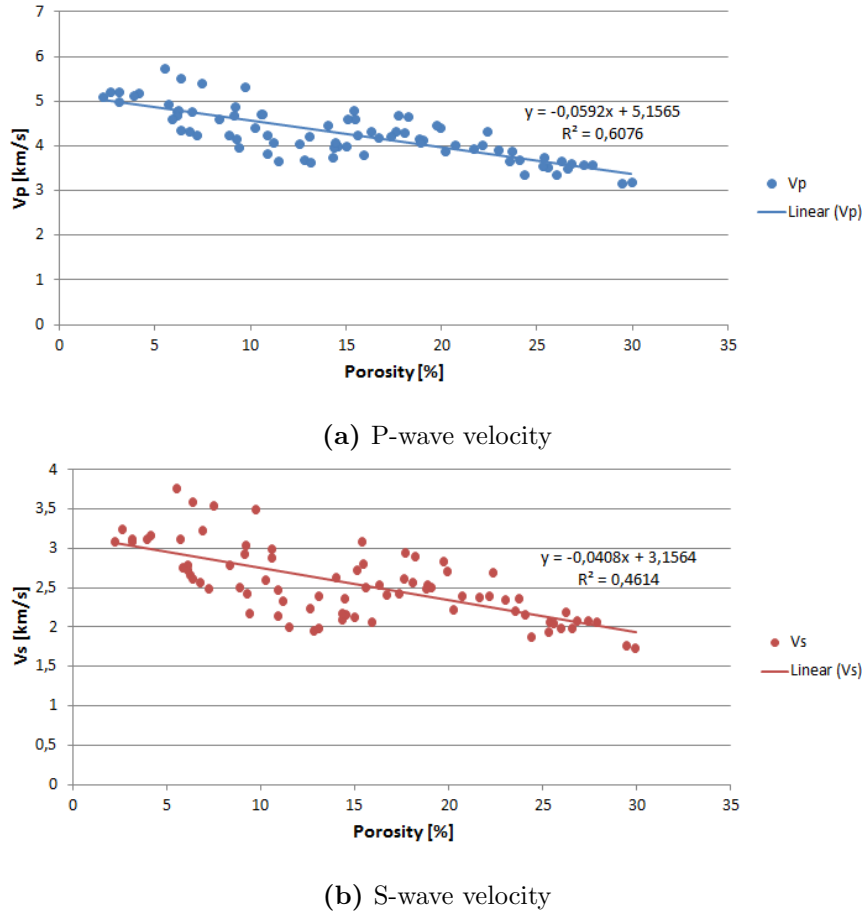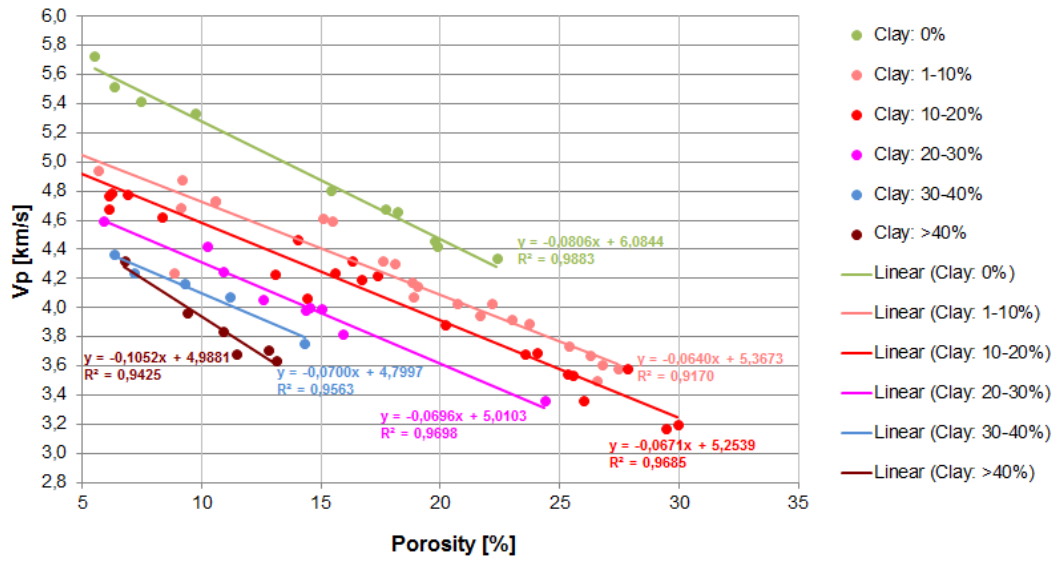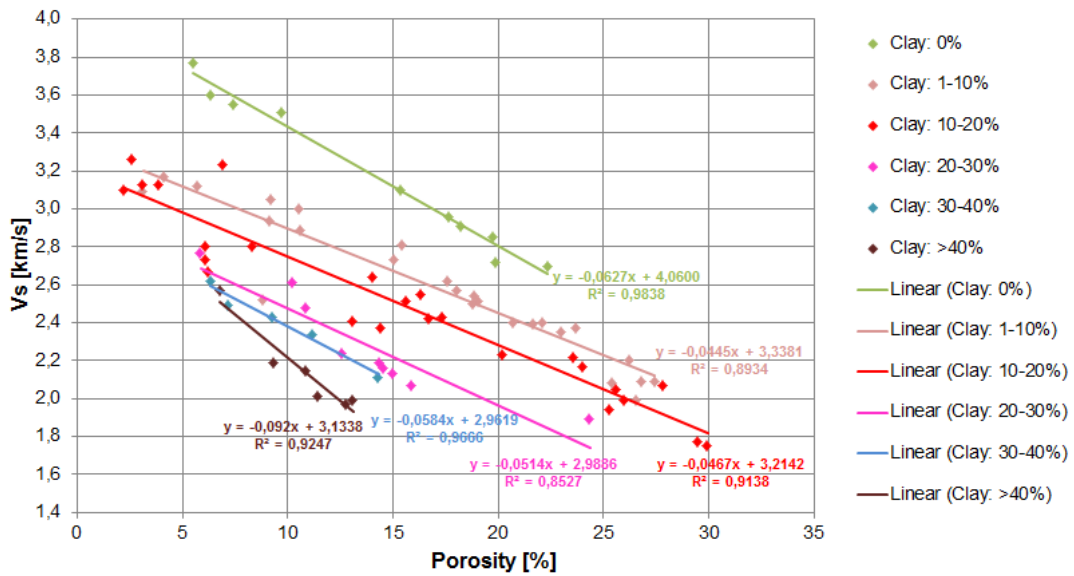

(a) P-wave velocity

(b) S-wave velocity

Figure 7.3: Han's V_P (a) and V_S (b) measurements plotted against sample porosities. Linear trend lines, with corresponding equations and correlation coefficients, are added to the charts.

According to Han's research, the correlation between velocity and clay volume fraction is approximately linear, just like velocity and porosity. To make sure that both dependencies enter into the final velocity model, the acoustic Han data is first sorted with respect to clay content, and then divided into several clay-limited data series, which are plotted separately against porosity. As a result, one get many velocity functions of porosity that is only valid and useable for sandstones containing clay fractions that fall within a specified range. Plots of the clay-sorted V_P and V_S data are provided in figure 7.4a and figure 7.4b, respectively.

(a) P-wave velocity

(b) S-wave velocity

Figure 7.4: Han's V_P (a) and V_S (b) measurements plotted against sample porosities and sorted with respect to clay volume fraction. Linear trend lines, with corresponding equations and correlation coefficients, are added to the data series.

Again, linear trend lines, with their equations and correlation coefficients, are drawn on top of the measurements. The green lines in both plots represent empirical velocity models for clean sandstones with zero clay content. Similarly, the pink, red, purple and blue lines are applicable for clay volume fractions ranging from 1 to 10 percent, 10 to 20 percent, 20 to 30 percent and 30 to 40 percent, respectively. The brown lines are representative for shaly sandstones/shales with clay content above 40 percent. From the correlation coefficients in figure 7.4, one can clearly see the improvement in the linear trend lines, after clay content is introduced as a parameter. All values, except one, are above 0.9. The scatter in figure 7.3 must therefore to a large extent be caused by the clay content effect. This is very reassuring in terms of the credibility of using porosity and clay content data to estimate velocities.

The clay content, i.e. the volume percentage of clay in a rock, decreases both the P- and S-wave velocity, as seen in figure 7.4. This phenomenon is most commonly explained to be a consequence of matrix clay, which is the kind of clay mixed with quartz that constitutes a part of the total matrix in a shaly sandstone. Matrix clay has lower elastic moduli than sand grains, and hence it will soften the rock matrix. Another clay effect on velocities, called the bound clay effect, must not be mixed with the clay content, or matrix clay, effect. The former, which is caused by tiny clay particles situated between grain boundaries, softens the boundary contacts and cements, and thereby decreases the velocities. Since the bound clay is limited to certain minor locations, its *volume fraction* is assumed negligible to the total clay content effect. However, it is very important when the clay volume fraction is just a few percent. A small portion of bound clay tends to decrease the velocities of a clean sandstone drastically, and is actually the main reason why the green (0 percent clay) and the pink (1-10 percent clay) lines are so far apart in figure 7.4. Besides clay and porosity effects, also other factors, such as pore geometry, clay type, clay distribution, grain packing, mineral composition and cementation, may affect the wave velocities in rocks. Luckily, these sensations seem to be suppressed at high pressures. They do, nevertheless, have some impact of second order, and are hence assumed the cause of the remaining scatter in the data series plotted in figure 7.4.

Naturally, also the density depends on the porosity of a rock. Since density is a measure of weight per unit volume, the amount of pore space has to be the main density controlling factor. The densities of Han's 80 samples were therefore plotted against porosities, in order to get a relation between the two. Figure 7.5 reveals that also the density is linearly decreasing with porosity. In addition, the high correlation coefficient of 0.9402 implies that other geological effects are less important to the density.

As a consequence of solid correlation, it is expected that accurate density data can be estimated with the density-porosity relation obtained from Han's dataset. For any rock in the reservoir, with a given porosity ϕ in percent, the density can be found by

$$\rho = 2.6595 - 0.0178\phi \quad , \tag{7.1}$$

which is the equation corresponding to the trend line drawn in figure 7.5. By applying this formula to the given porosity data, representative densities should hopefully be secured for the field.
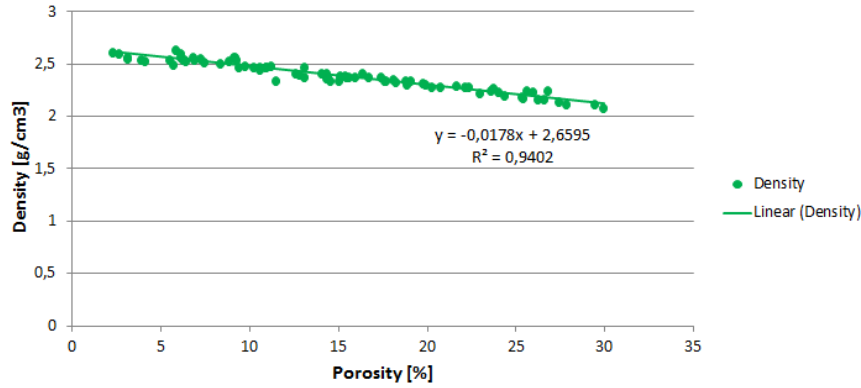

Figure 7.5: Han's density measurements plotted against sample porosities. A linear trend line, with the corresponding equation and correlation coefficient, is added to the chart.

When it comes to velocities, Han's acoustic data shows an encouraging dependency towards porosity and clay content. Since the velocity models presented in table 7.1 appear both satisfying and robust, they will provide one possible way of generating elastic input from Han's data. In addition, P- and S-wave velocities seem to be not only proportional, but linearly proportional to porosity and clay volume. As a consequence, V_P and V_S can easily be expressed as functions of both properties at the same time. Han found [16] that the best least-square fit to his velocity data is given by

$$V_P = 5.59 - 0.0693\phi - 0.0218C$$
$$V_S = 3.52 - 0.0491\phi - 0.0189C$$

(7.2)

where V_P and V_S are measured in km/s, while porosity, ϕ, and clay volume, C, are in percent. It turns out that the samples deviate from these trend lines only with 3 and 5 percent for P-wave velocity and S-wave velocity, respectively. As the above equations basically combine the ones shown in table 7.1, they should produce more or less the same input.

Clay content [%]	V_P [km/s]	V_S [km/s]
~ 0	$6.0844 - 0.0806\phi$	$4.0600 - 0.0627\phi$
1-10	$5.3673 - 0.0640\phi$	$3.3381 - 0.0445\phi$
10-20	$5.2539 - 0.0671\phi$	$3.2142 - 0.0467\phi$
20-30	$5.0103 - 0.0696\phi$	$2.9886 - 0.0514\phi$
30-40	$4.7997 - 0.0700\phi$	$2.9619 - 0.0584\phi$
>40	$4.9881 - 0.1052\phi$	$3.1338 - 0.0920\phi$

Table 7.1: Velocity equations generated with data from Han. The application of each equation is limited to the respective clay volume fraction range. ϕ is the porosity.

7.2 Other empirical velocity relations

Although Han's study on core-plugs probably is the most extensive one available out there, he is not the only scientist who has devoted a great deal of time to examine velocities in rocks, and their dependencies to porosity and clay content. By measuring seismic velocities in different samples, others have successfully been able to produce alternative velocity-porosity-clay models that are similar, but yet differ slightly from the one provided by Han. A common denominator, however, seems to be that V_P and V_S more or less always correlate linearly with both porosity and clay volume. In 1982, a duo consisting of Tosaya and Nur [17] came up with two linear velocity relations expressed as

$$V_P = 5.8 - 0.086\phi - 0.024C$$
$$V_S = 3.7 - 0.063\phi - 0.021C \quad . \tag{7.3}$$

Again, velocity, porosity and clay volume are given in km/s, percent and percent, respectively. These equations, like the equivalent ones obtained by Han, are results of multiple linear regressions that have been performed on acoustic data collected from various rock samples at ultrasonic frequencies. Despite the great resemblance between Tosaya/Nur's and Han's experimental setup and implementation, there are, however, a couple of important differences that should not be overlooked. First of all, Tosaya and Nur have concentrated their research on detrital silicate rocks characterized by pores with low aspect-ratios. Additionally, the empirical expressions given in equation (7.3) are derived at higher pore and confining pressures, respectively yielding 40 MPa and 80 MPa. A quick look at formula (7.3) and (7.2) reveals that Han-predicted velocities are less sensitive to both porosity and clay volume changes. As the acoustic data obtained by Tosaya and Nur deviates from velocity relation (7.2) only by approximately 2 percent, their model provides yet another plausible way of estimating elastic input.

Later, in 1985, a guy named Castagna [18] followed the footsteps of Tosaya and Nur and formed his own empirical velocity relation from a formation of the Gulf Coast of Texas. The Frio formation, which it is called, is dominated by series of deltaic and marginal-marine unconsolidated sands [19]. As the reservoir of interest consists of fluvial rocks, also with a low degree of consolidation, it is not beyond the realm of possibility that Castagna's velocity-porosity-clay relation is the one that best suits the field in question. The formulas for V_P and V_S, given by water saturated Frio-samples, yield

$$
\begin{aligned}
V_P &= 5.81 - 0.0942\phi - 0.0221C \\
V_S &= 3.89 - 0.0707\phi - 0.0204C \quad .
\end{aligned}
\tag{7.4}
$$

Both these relationships have a correlation term, R^2, equal to 0.92. Even though it is not clearly stated in [18], Castagna and his co-writers did presumably follow the exact same experiment procedure as Tosaya and Nur.

The density and velocity models given so far in this chapter are all derived from rock samples that are saturated with water (and sometimes brine). As water will not pass as the present pore fluid in the entire reservoir, their representativeness will naturally be lowered. The estimated data can therefore advantageously go through a fluid substitution formula before being applied to reservoir models as input. Prior to making a well-considered decision on which velocity relation to employ, a method to compensate for fluid properties is hence introduced.

Chapter 8

Gassmann's fluid substitution

In a reservoir, the pore space of rocks is always completely saturated with fluid. Water, oil, natural gas, or very often mixtures of the three, occupy the room between the grains and add to the long list of ingredients that determines the properties of the in situ rocks. Since different fluids have different compressibilities and densities, the wave velocities of reservoir rocks depend on the type of fluid present in the reservoir. In agreement with the theory presented in section 2.2, seismic waves will produce bulk-volume deformations in the rocks while passing by. This will obviously change the volume of the pores, increasing the pressure in the pore fluid. As the fluid pressure grows, the rock frame stiffens and the bulk modulus increases. Shear deformations, however, do not generate pore-volume changes, and consequently shear modulus is more or less independent of fluid properties. There are other fluid effects, such as chemical boundary reactions between the fluid and the grains, that may alter the shear modulus, but these are assumed second order effects and can often be ignored. From the isotropic P- and S-wave velocity equations,

$$
\begin{aligned}
V_P &= \sqrt{\frac{K + \frac{4}{3}\mu}{\rho}} \\
V_S &= \sqrt{\frac{\mu}{\rho}}
\end{aligned}
\tag{8.1}
$$

one can clearly see that shear wave velocities are only affected by fluid saturation through density changes, while pressure wave velocities are affected by both density and bulk modulus alternations.

In many reservoir disciplines, such as time-lapse monitoring of reservoirs, amplitude variations with offset and analysis of direct hydrocarbon indicators, fluid effects on velocities and seismic data are major concerns. Furthermore, acoustic measurements in laboratories are frequently done on core plugs that are completely dry, or saturated with brine, water or some kind of alcohol. Since these datasets, like Han's, do not represent the actual reservoir fluid conditions, they can be somewhat improved before utilized as input to reservoir models. Given these challenges, models that are able to predict changes in

elastic parameters and densities caused by fluid substitution are utilized time and again. Especially one model - Gassmann's fluid substitution model - stands out amongst the others. It has clear physical meaning, it is fairly simple and it has been proven quite accurate for a large number of rocks. The relations derived by Fritz Gassmann in 1951, are most commonly written as

$$K_{sat} = K_{dry} + \frac{\left(1 - \dfrac{K_{dry}}{K_{min}}\right)^2}{\dfrac{\phi}{K_{fl}} + \dfrac{1-\phi}{K_{min}} - \dfrac{K_{dry}}{K_{min}^2}} \tag{8.2}$$

$$\mu_{sat} = \mu_{dry} \tag{8.3}$$

where K_{sat}, K_{dry}, K_{min} and K_{fl} are the bulk moduli of the saturated rock, the dry rock (frame), the forming minerals and the fluid, respectively. In addition, ϕ is the porosity, while μ_{dry} and μ_{sat} are the shear moduli of the dry and fluid-saturated rock. Since all of these variables can be measured directly or are easily constrained, the formula above is very often the preferred choice when effects of fluid substitution are to be estimated.

The fluid effects on bulk density can easily be predicted by the fractional difference in density before and after pore fluid substitution. The density after pore fluid exchange, subscripted 2, is related to the initial density, subscripted 1, by

$$\rho_{sat,2} = \rho_{sat,1} - \phi\left(\rho_{fl,1} - \rho_{fl,2}\right) \quad . \tag{8.4}$$

Gassmann's bulk modulus equation (8.2) can be formulated in many ways. The expression given in (8.2) is obviously suitable for estimating bulk moduli of fluid saturated rocks when dry rock data is known. However, if acoustic measurements are done on wet rocks, say saturated with brine, and the goal is to estimate data on the same rocks with alternative pore fluids, other forms are possibly better. In the latter case, one can rather apply

$$K_{sat,2} = \frac{K_{min}}{\left[\dfrac{K_{sat,1}}{K_{min} - K_{sat,1}} - \dfrac{K_{fl,1}}{\phi\left(K_{min} - K_{fl,1}\right)} + \dfrac{K_{fl,2}}{\phi\left(K_{min} - K_{fl,2}\right)}\right]^{-1} + 1} \quad , \tag{8.5}$$

where the indices 1 and 2 once more correspond to the initial and final state of fluid saturation, respectively. Both Gassmann equations (8.2) and (8.5) are used in this study, since elastic input to the reservoir models is derived from dry and pure brine saturated core measurements. These pore conditions are obviously not representative of those in the reservoir, and hence the effects of reservoir fluids must be accounted for by Gassmann's equations in order to reproduce/simulate well logs and seismic data. Given an initial set of velocities and densities, collected from either well logs, core samples or theoretical models, the following recipe can be carried out:

1. Rearrange the isotropic velocity equations in (8.1) to find the bulk and shear moduli of the rock with initial pore saturation.

2. Apply either Gassmann equation (8.2) or (8.5) to get a bulk modulus suitable for the rock with a new pore fluid.

3. In agreement with equation (8.3), keep the shear modulus unchanged.

4. Calculate the new bulk rock density by employing equation (8.4).

5. With the equations given in (8.1), compute velocities that correspond to the new elastic properties.

There are several assumptions, application constraints and pitfalls to be aware of in order to avoid misuse of Gassmann's theory. First of all, the rock is assumed isotropic, elastic, monomineralic and homogeneous. Secondly, there should be no chemical reactions between the fluid and the rock frame, and thirdly, the pore space should be well connected and in pressure equilibrium (frequency effects are overlooked). Finally, the rock is assumed to be a closed system with no fluid movement across its boundaries [22]. Many of these assumptions are of course violated in a real reservoir. Rocks are all anisotropic in some degree, frequency effects such as dispersion will occur for waves in the seismic frequency band ($10 - 100Hz$), and reactions such as cementation and dissolution will affect the shear moduli of the rocks. Since the bound water in shale cannot move freely, Gassmann's equations are also not theoretically valid for sands containing shale [23]. In the absence of other applicable models, Gassmann substitution is still a favorite among rock physicists. A good habit, however, would be to always look at the results with critical eyes and make sure that the estimated moduli are within the limits of reason.

Another aspect to consider is the input parameters that enter into the Gassmann equations. These can either be estimated by different theories or can be obtained from examination of core samples in laboratories. The first approach will often give crude estimates, which in turn can give unrealistic fluid effects. The second approach is obviously more time-consuming and costly. In addition, there are uncertainties connected to the conditioning of samples. Core plugs that are brought up from deep, high-pressure reservoirs can easily be damaged on their way up to the low-pressure surface, and eventually give misleading data. Porosity, density and velocity are not independent, and to minimize error, they should be kept consistent and constrained [22]. It is therefore very important to be precautious when selecting input. Han and Batzle provide a study on how to constrain the input parameters, by applying Voigt-Reuss bounds and critical porosity to Gassmann's equation in article [22]. Due to the time span of this thesis, their findings have not been a priority. The inputs can rather be evaluated with experience and common sense. For example, it must be true that

$$K_{min} \geq K_{sat} \geq K_{fl} \quad ,$$

since the bulk modulus of the fluid is smaller than the bulk modulus of the mineral in a rock.

In the absence of measurements on matrix, fluid and frame properties, K_{min}, K_{dry}, K_{fl}, ρ_{sat} and ρ_{fl} must be found elsewhere, as mentioned, if one wishes to use Gassmann's substitution theory. As the problem of finding applicable values to these unknown variables are spread across several rock physics disciplines, there exist a countless number of articles and authors that try to address it either fully or partially. Batzle and Wang's study on pore fluid properties from 1992 [20], for example, provides a recognized way of determining K_{fl} and ρ_{fl} in Gassmann's equation, while Hill supplies theory that can be employed to find K_{min} [21]. To facilitate the use of Gassman's formula, a guy named Kumar has gathered all the necessary explanations, formulas and constants in *one* easy-to-follow article. In support, he has also kindly included an implementation of the theory. Accordingly, whenever there is need of a pore fluid substitution, [24] is the place to look.

Chapter 9

Determination of elastic model input

In chapter 7, three velocity relations were introduced as possible candidates to replace specific core data. Since these relations are all derived from respective sets of core plugs, with diverse origins, lithology and/or pressure conditions, they will certainly provide unequal properties. As a natural consequence, the velocity models in (7.2), (7.3) and (7.4) should represent the reservoir of interest to different extents. The aim of this chapter is therefore to find out whether any of them are suitable, to examine their correctness, and to ultimately decide which way to go in order to produce the most accurate input. In essence, this is carried out by comparing reservoir-penetrating sonic well logs to synthetic ones provided respectively by the velocity-porosity-clay relations of Han, Castagna and Tosaya/Nur. By feeding the latter equations with porosity and clay volume data from an appointed well, one will be able to calculate comparable V_P and V_S for each depth point. The artificial values can then easily be plotted on top of the actual measurements, allowing us to visually scrutinize the validity of the velocity models. Accompanying the porosity log, the clay volume log and the velocity logs, a sand indicator is provided for the given well. Since the empirical relations of Han, Castagna and Tosaya/Nur are mainly derived for shaly sandstones, it is not guaranteed that they will suit all types of rocks present in the selected reservoir. The net sand log, which roughly divides the spatial measuring intervals into sand and non-sand, can hence be useful to determine where, and for what species of rocks, the relations are applicable. In order to generate realistic *elastic* input, however, accurate velocities are not enough. One also needs trustworthy densities. Consequently, before passing judgment on the velocity models, the solitary density-porosity correlation deducted from Han's data, and given in equation (7.1), is verified.

The model for density is also examined with the aid of well logs, as exemplified by figure 9.1 . On the left hand side, the porosity data associated with the designated well is plotted against depth. As the density is assumed dependent on porosity only, the synthetic, black density log in the adjacent plot is controlled entirely by this curve. To

be able to evaluate the density relation properly, the measured data (red) is added to the figure. The rightmost net sand and clay volume logs do not impact the synthetic density log directly, but should nevertheless have some common features. They are mainly provided to illustrate that the density model's accuracy do not change a lot with different rock types. For the sake of comparability, 8 meter tall representatively chosen sections are displayed in figure 9.1.
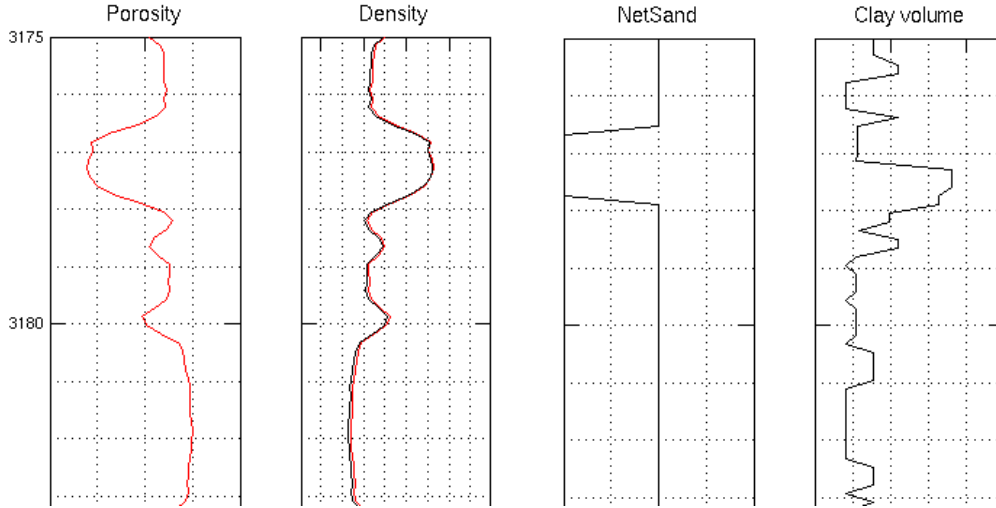

Figure 9.1: The synthetic density log (black) generated with Han's empirical denisty-porosity correlation is paractically identical to the actual well log (red), when the leftmost porosities are applied as input. This basically means that the relation is reliable.

Seeing that the synthetic density log follows the measured log intimately throughout the entire section, and does so for the remaining parts of the well, it appears that the density model derived from Han's data is not only applicable, but applicable to all kinds of rocks present in the reservoir. For practical purposes, this means that equation (7.1) can safely be employed to get reliable densities for each and every cell in the various facies models. It is also worth noticing that the measured density and porosity logs are more or less mirror images in figure 9.1. As it is a common logging procedure, this conformity is probably caused by porosities being initially computed from the density log, in a manner similar to producing synthetic data. Other than that, the logs show natural behavior. The absence of sand (net sand = 0) yields less pore space and lower porosity, which in turn increases the density, and so on.

The verification of the velocity models, however, is a bit more intricate. First of all, the synthetic velocities do not only relate to one property, but two. Secondly, the clay volume log is crudely estimated from other well measurements, causing one dependency to come with a large degree of uncertainty. When one on top of this adds the fact that measured velocities are not related to porosity and clay volume in the same immediate

and strong way as density to porosity, there is no wonder that the process of evaluating velocities is trickier. Since the latter complications heavily suggest that the fit between synthetic and authentic V_P and V_S will be poorer than that of the density, it feels natural to give more attention to the examination of the velocity models.

From left to right, figure 9.2 displays porosity, clay volume, P-wave velocity and net sand logs associated with hundred meters of rock present in the reservoir basin. As one hopefully know by now, the porosity and the clay volume logs provide input to the various velocity models. In addition, they can among other thing be used as tools to distinguish reservoir sands from surrounding background material. To assist them with that, the net sand log, which respectively is one and zero for sands and non-sands, is included on the right-hand side of the figure. The background material is recognized by little or no sand, low porosity and a significant amount of clay. Much more important, however, are the three pairs of logs located in the middle of figure 9.2. Each of these consists of the well's sonic V_P-log (red) and a synthetic one (black) obtained from one of the three given velocity relations. While the leftmost black velocity curve is computed by the use of Han's model, the two others are generated with the models provided by Castagna and Tosaya/Nur, respectively. The reliability of each empirical velocity-porosity-clay relation is reflected in the difference between synthetic and authentic data. Obviously, the corresponding S-wave velocity models should also be considered. However, as it turns out that the synthetic V_S-logs resemble those of V_P in terms accuracy, they are left out of figure 9.2. Whenever the synthetic V_P data is close to the measured, one may assume that the V_S data, associated with the same velocity model, is too. A few core plug measurements are additionally added to the velocity plots as reference points. Because figure 9.2, for visualization reasons, only shows properties at depths from 3300 to 3400 meters, merely one can be seen. It is marked as a green diamond.

The main feature to take note of in figure 9.2 is the apparent change in velocity model accuracy that arises whenever a sand zone is entered or exited. As one quickly discovers, the fit between synthetic and authentic data is quite poor in regions where the net sand log is equal to zero. Furthermore, it appears that the various velocity models all tend to overestimate the velocities in non-sandy intervals quite significantly. The red box in figure 9.2 indicates a good example. While the measured velocity in this marked section remains roughly at the same level as in the sandstone above, and sometimes even falls, the three synthetic ones immediately increase. According to the acoustic relations described in chapter 7, velocities of rocks are supposed to decrease with clay content and, to an even greater extent, porosity. Evidently, this does not apply to the non-sandy parts penetrated by the well. Although these rocks typically are rich in clay, they should by virtue of their low porosities be able to boost velocities. Since they do not, it is crystal clear that the reservoir's background material and the rock samples used to derive the models of Han, Castagna and Tosaya/Nur are of two completely different sorts. In fact, they deviate so much that the three latter velocity relations are deprived of the task of producing input to the reservoir model cells that constitute the background material.
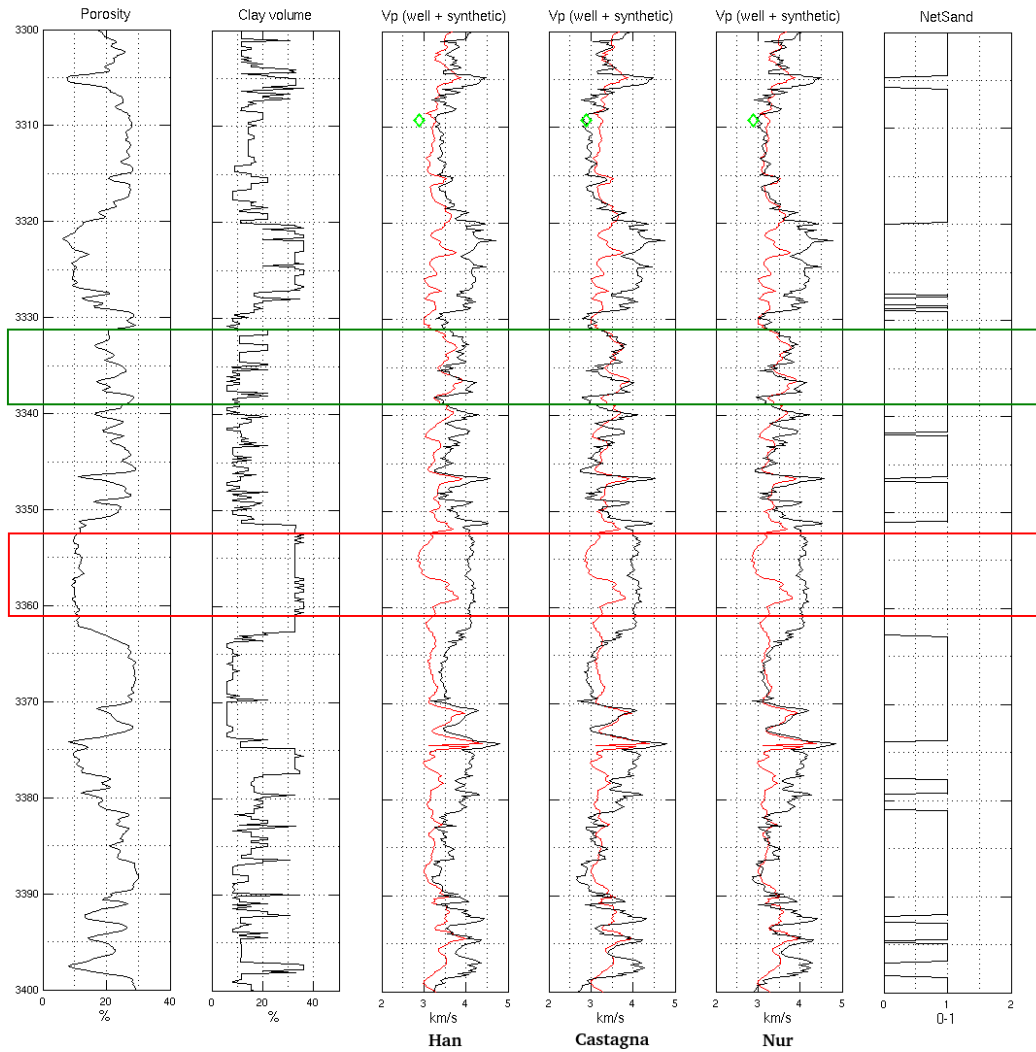
Figure 9.2: Verification of the empircal velocity-porosity-clay relations provided by Han, Castagna and Tosaya/Nur. Synthetic velocities (black) are generated with the appointed well's porosity and clay volume logs (columns 1 and 2) as input. The computed V_P data associated with each relation is plotted together with the sonic well logs (red) in columns 3, 4 and 5. On the right side, the interpreted net sand log is included. The green rectangle illustrates that the models are suitable in sandy zones, while the red rectangle implies that they are not in background areas. The green diamond represent a single core sample measurement.

For rock sections accompanied by a net sand log of one, on the other hand, the correspondence between sonic and synthetic logs is much better. To illustrate this, a green rectangle is defined around a representative interval of reservoir sands. Within the box,

each synthetic log seems to capture the main features of the authentic data rather well. There is, however, no escaping the fact that the various velocity models and their inputs come with a certain degree of inaccuracy. As one observes, the red, measured velocity curve is somewhat smoother than the black, generated ones. This is mainly due to the discontinuous nature of the clay volume log. Even though the amount of clay does not have the same impact on velocities as porosity, spikes of some size have indisputably put their mark on the synthetic data. Seeing that the generated V_P-logs largely mimic the one of porosity, the suitability of the different velocity models naturally improves wherever the sonic log also does it. As this looks to be the case in most areas with sand, causing the black curves to roughly follow the red one's highs and lows, the empirical relations of Han, Castagna and Tosaya/Nur should be sufficiently accurate to produce input to the non-background parts of the facies models. When the time is ripe to compare the models with inverted seismic data, it would be gratifying to recognize common elastic features.

With merely figure 9.2 on hand, it is difficult to determine which velocity relation is best fitted to describe the reservoir sands. Seemingly, the relation of Han is less reliable than the ones of Castagna and Tosaya/Nur. As the synthetic V_P-log associated with Han constantly, almost without exception, lies above the measured, sonic one, it is not as representative as the others. The velocity models of Castagna and Tosaya/Nur, however, are harder to separate. Although the latter empirical relation seems to produce slightly better velocities in the sandy zones of figure 9.2 compared to Castagna's, one cannot tell with absolute certainty which is the preferred choice. After all, in a figure that does not show the entire log, the two models take turns predicting the most precise velocities. To support the decision making, three cross-plots showing generated acoustic properties versus measured acoustic properties are provided and displayed in figure 9.3. The beauty of these plots is that they present the fit, or correlation, between synthetic and authentic data in a very simple and intelligible manner. In the ideal case of perfect velocity models, the three sets of data points in figure 9.3 should form straight lines with slopes and y-intercepts respectively equal to one and zero. Practically, this means that the suitability of each empirical velocity relation can be evaluated on the basis of data dispersion about the black, dotted diagonals, which are added to the plots for reference. Now that the models of Han, Castagna and Tosaya/Nur already are ruled out as input suppliers to the non-sandy parts of the reservoir, a comparison between them is only meaningful where sand is present. The velocities connected to positive net sand values are hence differentiated from the others in figure 9.3. While the blue dots reveal the correlation between synthetic and measured data in sandstones, the magenta ones do it for the background material. An attentive eye will also remark that the authentic and synthetic data sets, plotted on the x- and y-axis, respectively, are expressed as DT instead of V_P. DT, which is a measure of the P-wave transit time, relates inversely to the P-wave velocity. Accordingly, the data points situated below the diagonals are associated with overestimated velocities and the points above with underestimated velocities.
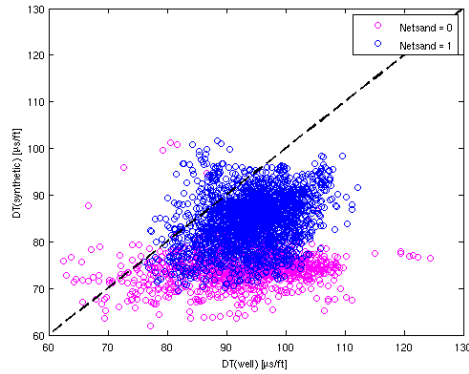
(a) Han
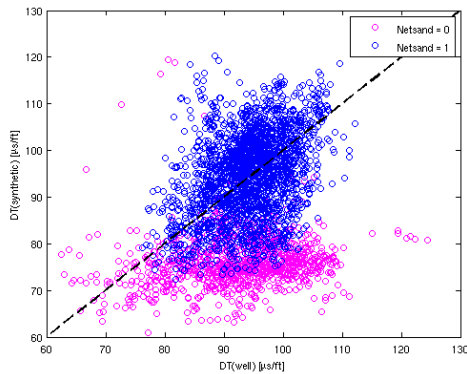
(b) Castagna
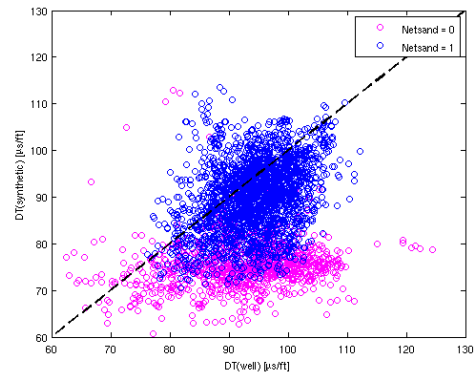
(c) Tosaya & Nur

Figure 9.3: Cross-plots of synthetic (y-axis) and measured (x-axis) transit times (DT). The blue data sets are associated with sand (net sand $= 1$), while the magenta ones are associated with background (net sand $= 0$). The data should align with the black diagonals for the velocity models of Han (a), Castagna (b) and Tosaya/Nur (c) to be reliable.

By comparing the different cross-plots in figure 9.3, one will quickly be able to confirm what has already been learned through the log examinations. As the uppermost plot clearly shows the largest imbalance of data points about the diagonal line, it must be true that Han's velocity model is the least representative of the three. Furthermore, the location of the blue, cloud-like accumulation in plot 9.3a emphasizes the latter model's tendency to predict unduly high velocities for sandy rocks. Consequently, the acoustic measurements of Han must have been performed on sandstone samples that are stiffer than the ones present in the reservoir. Probably, the low degree of consolidation in the area has a substantial impact. Without regarding the relative position, the data set associated with Han's model accumulates at least as dense as the others. This bodes well for its usability in other types of reservoirs. For this particular study, however, the empirical

relations of Castagna and Tosaya/Nur are more attractive, as illustrated in plots 9.3b and 9.3c, respectively. With these figures on hand, it is now also possible to separate the latter two models in terms of suitability. Seeing that the blue set of data printed in the bottom plot has a slight predominance towards the lower parts, while the one in the middle looks more or less balanced about the diagonal, the relation of Castagna appears to be the most reliable. Accordingly, in the absence of better alternatives, the latter velocity-porosity-clay relation is entrusted the responsibility of producing sand input to the reservoir models.

Pleasantly, also the laboratory measurements seem to speak in favor of Castagna's velocity relation. As partly illustrated in figure 9.2, the estimated velocities and the lab data correspond almost perfectly. This, however, does not necessarily have to mean anything. Given the fact that the sonic log runs past the green diamond without touching, it is likely that the laboratory data is inaccurate. Notwithstanding, one should never trust well logs uncritically. During data acquisition the logging instrument might for example be damaged or its position poorly tracked. Hence, as the model of Castagna is both acknowledged and extensively used, there is in fact a possibility that it is more dependable than the log. Whether this is true or not, is hard to say. Castagna's model is in any case the preferred choice.

Since the reservoir of interest is deposited in a fluvial environment, the background material should certainly consist of non-sandy rocks that are typical to find between channel belts, crevasse splays and other river-associated features. This, however, leaves us with a lot of options. Without going into further detail, the intermediate materials might be anything from solid and stiff bedrock to soft, lithified soil. Considering the fact that the non-sandy parts of the well log are mainly characterized by low porosities, high clay volumes and low velocities, the latter is probably true for the topical reservoir. Regardless of its origin, the background material is nevertheless a soft mudrock that cannot be described properly with either the empirical velocity-porosity-clay relation of Han, Castagna or Tosaya/Nur. Consequently, a separate way of representing the background rock is needed. The process of actually finding one, per contra, turned out to be much more difficult than expected. Initially, a whole lot of literature was sought through, hoping to come across an empirical model able to predict low velocities in compact (low porosity) rocks. This unfortunately bore no fruits. Apparently, soft mudrocks are highly understudied, making it impossible to procure tolerable relations. In order to obtain proper background input, one must hence come up with a work-around. A natural next step is to try to make a velocity relation straight from the well log measurements. By extracting the data that is associated with non-sands, and plotting V_P and V_S against porosity, one might get a correlation. Whether the data can be used as a mean to generate input to the background cells depend obviously both on the scatter, and the accuracy of the logging tools. Figure 9.4 shows, with the same color scheme as before, the relation between P-wave velocity and porosity. The points in magenta represent what is presumably background material.
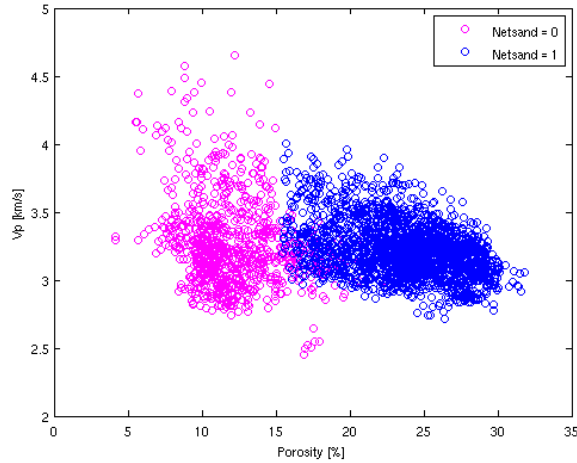
Figure 9.4: Well measurements on V_P plotted against appurtenant porosities. The blue data set is associated with sand (net sand = 1), while the magenta one is associated with background (net sand = 0). The correlation between porosity and V_P is weak in non-sandy rocks.

As inevitably seen in figure 9.4, the V_P-porosity correlation of the mudrock is virtually non-existent. Not even when one sorts the data with respect to clay volume and/or facies interpretations, the relation seems to improve. In a final attempt to strengthen the correlation, one may want to combine data from several wells located close to each other. However, as it is only two that provide S-wave data in the relevant area, the last-mentioned proposal is in this case nothing but a dead end. In principle, this means that only two alternatives remain to be chosen from. Either one can select a single value (typical the average) of V_P, V_S and density, and use that to populate all background cells, or one can, for each individual, pick properties from a distribution. Since the latter method to a greater extent considers the conspicuous variations in the background material, it is the one preferred. The histogram provided in figure 9.5 reveals roughly the shape of the V_P-distribution. For each rectangular velocity bin, the height corresponds to the number of log measurements that falls within the given range. Whereas V_P, V_S and density are not entirely isolated properties, they should be picked in triplets to prevent their mutual dependencies to disappear. By refraining to do so, the elastic behavior of the background material will be at risk of becoming unnatural. Consequently, it is only the V_P-value of each background cell that is randomly selected from the log data. The remaining two properties simply tag along, as they are the corresponding log values of V_S and density.

With Castagna's empirical velocity relation and the distribution of non-sandy well data available, one should be able to describe both the reservoir sands and the background

material in a satisfying manner. Nonetheless, there is always room for improvement. The best possible solution to the input problem is obviously to carry out a laboratory study similar to the one done by Han, only confined to the reservoir of interest. Especially the background material, which is rather complicated, should be reviewed much closer. As these rocks limit the sandy parts of the reservoir, and contribute to the reservoir characteristics, it is important to get them right. This kind of research, however, is extremely time consuming and costly. Consequently, the stipulated input appears to be as good as it gets with the time frame and resources provided.
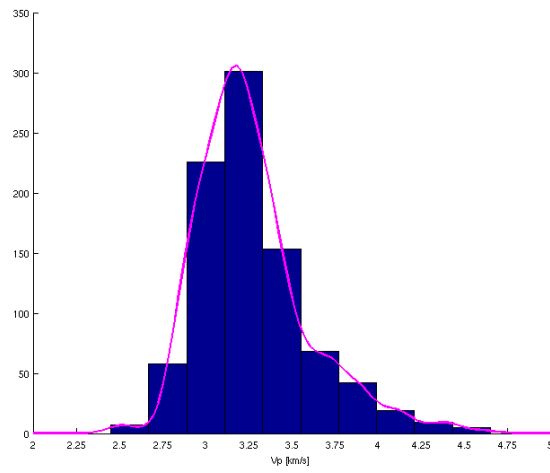

Figure 9.5: Distribution of V_P well measurements associated with background material (net sand = 0). The height of a rectangle reflects the number of observations made in a particular bin.

Chapter 10

Upscaling results

Now that one has velocity and density models for the reservoir sand, and velocity and density distributions for the background material, it is possible to assign elastic properties to the various facies models. From before, each individual grid cell has been given a number that ties it to a particular lithofacies. As the set of lithofacies correspond to smaller and already upscaled models, a handful of effective properties, like porosity, clay volume and permeability, indirectly follow. In principle, this means that certain properties are preset on the cell-level in each facies model. Whether the latter qualities can be exploited to populate grid cells with agreeing elastic properties or not, depend on the type of lithofacies. If a grid cell is associated with sand, the empirical velocity-porosity-clay relation of Castagna can be used to generate elastic parameters. If it is associated with background material, on the other hand, velocities and density should be arbitrarily picked from the respective well log distribution. Consequently, the models had to be iterated through, cell by cell, for their elastic properties to be properly determined. At each step, the cell was either checked of as one of the background lithofacies or one of the sand lithofacies. In the case of the latter, the corresponding porosity and clay volume values were extracted and fed into equations (7.4) and (7.1) to produce V_P, V_S and ρ for the given cell. Whenever not, the same properties were randomly taken from the distribution shown in figure 9.5. With velocities and densities available, a rearrangement of expression 8.1 were finally employed to assign isotropic elastic properties to each cell, in the form of bulk (K) and shear (μ) moduli. The latter values were written to the models' *.grdecl*-files as cell specified input.

Having populated the different models with elastic parameters, it is time to find their effective properties through upscaling. In a sense, this is equivalent to bringing three-dimensional knowledge about reservoir facies to the seismic scale. Due to shortage in time, the facies models had to be chopped into smaller pieces before they were upscaled. Pursuant to their lateral size (100×100 or 50×50), they were divided into 8 or 4 equally large submodels. After having been upscaled separately, the resulting tensors of the chops were averaged over each facies model. Accordingly, all models were assigned one effective modulus. In order to ease reciprocal comparison between the individual

reservoir models, corresponding velocities were computed from the elastic tensors. This was done through Christoffel equation, given in section 2.4. To make use of the latter expression, average densities must also be accessible for each model. Consequently, it is crucial to keep track of both material densities and volume weights throughout the upscaling process. As an important part of the current study is to examine anisotropy in the effective mediums, V_P and V_S were both found vertically and horizontally for each facies model. In addition, elastic tensor rotation was applied to obtain velocities at an angle of 50 degrees. This particular angle happens to be the mean deviation of the well employed in chapter 9.

The effective horizontal and vertical velocities for all 62 reservoir models are given in figure 10.1. On the left hand side, the plots are dedicated to P-wave velocities, whereas on the right they are reserved for corresponding S-wave velocities. The two bars associated with each facies model represent lateral and vertical velocities, respectively. Figure 10.2, on the other hand, displays vertical velocities together with $50°$ tilted ones. Beyond that, the latter figures are identical.

The reservoir is divided vertically into zones and subzones according to geology and depositional environment. Due to unequal conditions, facies and their properties tend to vary from zone to zone, and even from subzone to subzone throughout the reservoir. As a result, each facies model is created specifically for one subdivision. Owing to the fact that the reservoir is fluvial, the models merely attempt to describe channel belts. To take into consideration the lateral variations of the channel belts, and also the lack of detailed knowledge about the subsurface, several possible facies models are provided per subzone. These consist of slightly different geometries, volume weights and materials, and yield somewhat different elastic properties. As seen in figures 10.1 and 10.2, the various facies models are sorted and plotted pursuant to their zones and subzones. While the zones are differentiated with various bar charts, the subzones within are simply separated with colors. In this particular case, there are 4 zones and 11 subzones which models are distributed on. Since channel belts are expected to change moderately within each zone and subzone, it is interesting to see how the models' effective velocities vary in corresponding groups. This will additionally allow one to specify velocity ranges for each zone/subzone that channel belts are anticipated to reside in. By means of minimum, maximum and average effective velocities, table 10.1 gives a quantitative description of these ranges. Although it is only vertical V_P that really matters when comparing upscaled velocities with velocities obtained from inverted seismic data, the statistics for all the plotted properties are included in table 10.1. This will essentially provide an opportunity to quantitatively investigate the anisotropy of the various facies models at the seismic scale. The main function of table 10.1, however, is to supplement the bar charts.

As seen in figures 10.1 and 10.2, the homogenized facies models yield only slightly differing effective properties within each subzone. In principle, this means that the lateral

channel belt variations in the reservoir are expected to be small. Hence, if the models are representative, different channel facies in a given subzone should produce more or less equal velocities on the seismic scale. Subzone 4.2, however, is a clear exception. From the looks of figure 10.2d, the models associated with this subzone appear to describe two completely different types of channel belts. Consequently, it must be more than just minor differences in geometry and material properties that separate these. Anyhow, the velocity variance within and between zones is generally much more prominent. This is an expected feature, as significant changes in geology typically occur at larger scales.

To examine the anisotropy of the various facies models, one has to compare the lateral, vertical and angled velocities with each other. If the difference is large, the effective medium has a high degree of anisotropy, if not, it is close to isotropic. This particular property will determine whether deviated wells have to be corrected before legitimately compared or integrated with seismic data. As demonstrated by figures 10.1 and 10.2, the velocities do have a certain directionality. Moreover, it can be observed that the lateral velocities are larger than the ones measured at an angle of 50 degrees, which in turn are larger than the vertical ones. The latter feature is typical for transverse isotropic materials with vertical symmetry axes (subsection 2.3.2). Since the effective velocities change with $3 - 4\%$ at most, the anisotropies in the upscaled models are regarded as weak, but considerable. This basically means that one in fact should correct deviated data. If one refrains, one will undoubtedly introduce bias in the results. There is also reason to believe that the anisotropy will be greater at the seismic scale if the elastic input to the facies models actually consists of upscaled lithofacies. In accordance with this, it will normally be wise to adjust deviated wells before feeding them into the seismic inversion method. The correction itself is easily performed with elastic tensor rotation - described in section 2.5.

| Subzone	Orientation	V_P (km/s)			V_S (km/s)		
		Min	Max	Avg	Min	Max	Avg
1.1	Lateral	3.3305	3.3848	3.3526	1.9580	2.0007	1.9766
	Vertical	3.2868	3.3298	3.3041	1.9131	1.9489	1.9287
	Rotated	3.2961	3.3417	3.3147	1.9415	1.9820	1.9593
1.2	Lateral	3.1808	3.1861	3.1831	1.8044	1.8094	1.8062
	Vertical	3.1604	3.1651	3.1628	1.7853	1.7893	1.7876
	Rotated	3.1656	3.1702	3.1676	1.7981	1.8029	1.8002
1.3	Lateral	3.3428	3.4363	3.3834	1.9178	1.9841	1.9457
	Vertical	3.2921	3.3576	3.3213	1.8702	1.9087	1.8861
	Rotated	3.3039	3.3764	3.3359	1.9021	1.9572	1.9248
2.1	Lateral	3.4426	3.4845	3.4682	1.9858	2.0361	2.0123
	Vertical	3.4035	3.4407	3.4256	1.9289	1.9806	1.9591
	Rotated	3.4047	3.4466	3.4293	1.9674	2.0177	1.9963
2.2	Lateral	3.4648	3.4823	3.4740	2.0095	2.0226	2.0143
	Vertical	3.4232	3.4308	3.4264	1.9483	1.9636	1.9580
	Rotated	3.4291	3.4374	3.4322	1.9914	2.0033	1.9969
3.1	Lateral	3.3492	3.3514	3.3501	1.9309	1.9348	1.9330
	Vertical	3.3048	3.3101	3.3079	1.8812	1.8869	1.8847
	Rotated	3.3131	3.3172	3.3152	1.9113	1.9174	1.9156
3.2	Lateral	3.2964	3.3173	3.3078	1.8665	1.9032	1.8872
	Vertical	3.2616	3.2785	3.2686	1.8325	1.8599	1.8452
	Rotated	3.2697	3.2826	3.2765	1.8550	1.8876	1.8722
3.3	Lateral	3.4366	3.5232	3.4794	1.9925	2.1205	2.0546
	Vertical	3.4251	3.5222	3.4731	1.9588	2.1130	2.0337
	Rotated	3.4182	3.5193	3.4677	1.9824	2.1188	2.0492
3.4	Lateral	3.2096	3.2193	3.2142	1.8569	1.8630	1.8600
	Vertical	3.2012	3.2101	3.2038	1.8445	1.8520	1.8489
	Rotated	3.2025	3.2113	3.2058	1.8524	1.8593	1.8561
4.1	Lateral	3.2619	3.2778	3.2716	1.8616	1.8776	1.8714
	Vertical	3.2345	3.2459	3.2416	1.8359	1.8487	1.8437
	Rotated	3.2411	3.2541	3.2490	1.8527	1.8674	1.8617
4.2	Lateral	3.2213	3.5069	3.3659	1.8428	2.0544	1.9479
	Vertical	3.2059	3.4554	3.3315	1.8287	1.9971	1.9125
	Rotated	3.2095	3.4634	3.3376	1.8384	2.0366	1.9370

Table 10.1: Descriptive upscaling statistics. Minimum, maximum and average V_P and V_S are displayed for each subzone at different measuring orientations. The orientation called "rotated" implies a measuring angle of 50 degrees from the vertical.
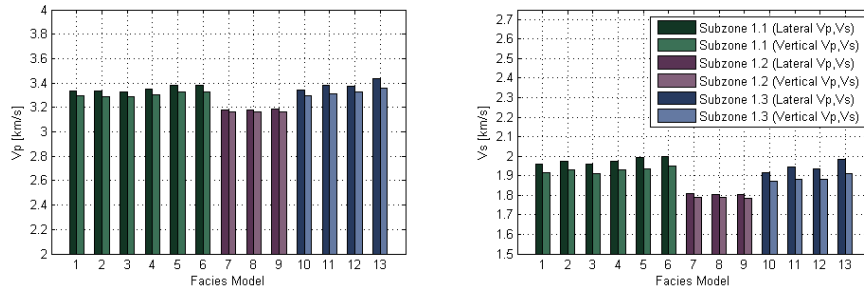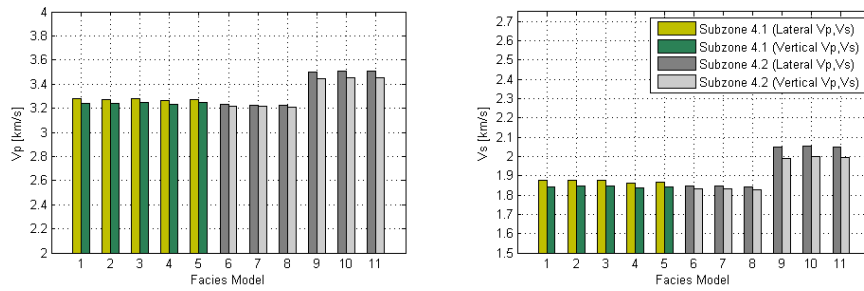
(a) Zone 1
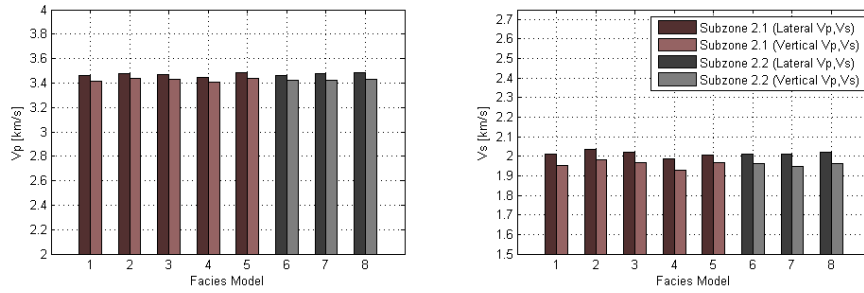
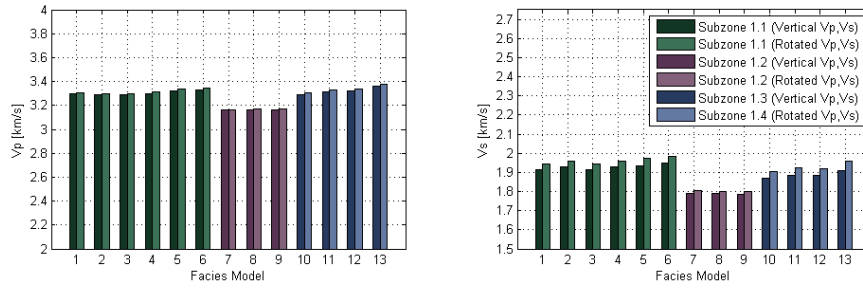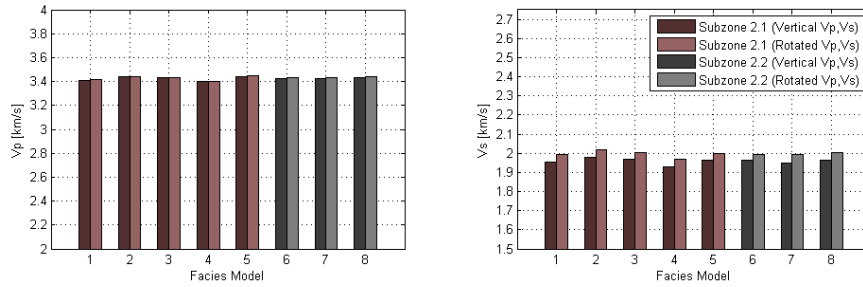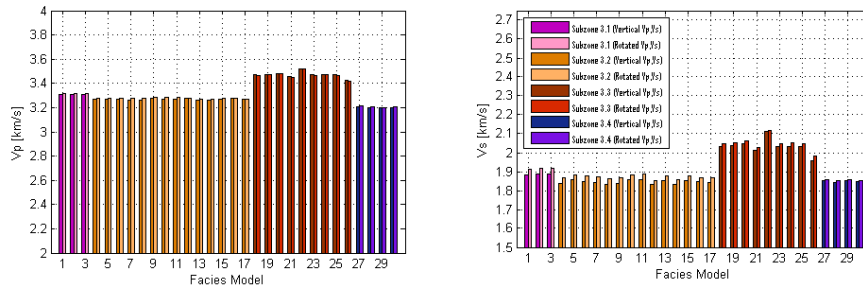**(b)** Zone 2
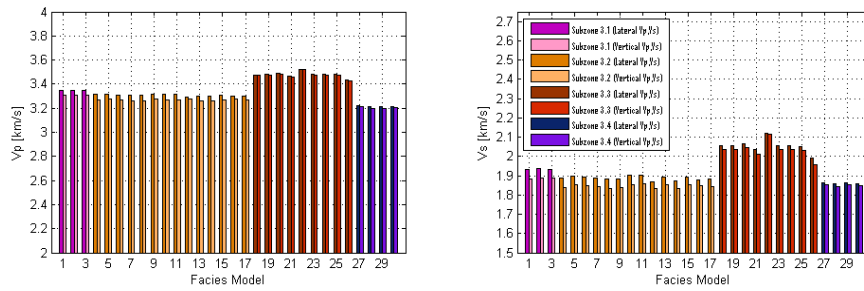
(c) Zone 3

(d) Zone 4

Figure 10.1: Resulting V_P (left column) and V_S (right column) from upscaling. Both the lateral and vertical velocities are shown for each facies model. Since each model attempts to describe channel belts within a given subzone of the reservoir, they are sorted with respect to subzone and plotted with distinct color schemes. Plot (a) shows upscaled properties associated with reservoir zone 1, plot (b) zone 2, etc.
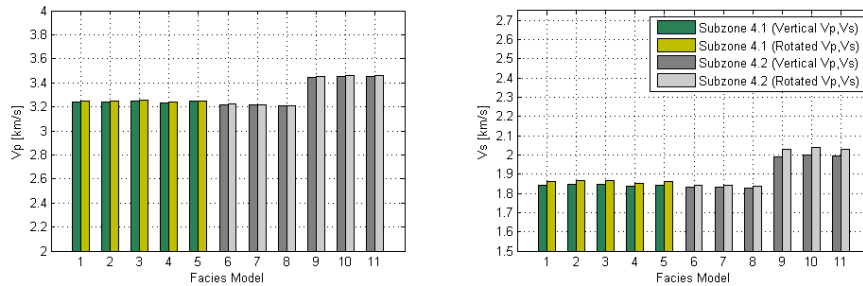
(a) Zone 1

(b) Zone 2

(c) Zone 3

(d) Zone 4

Figure 10.2: Resulting V_P (left column) and V_S (right column) from upscaling. In this plot, vertical and rotated (50 degrees from z-axis) velocities are shown for each facies model. They are sorted with respect to subzone and plotted with distinct color schemes. Plot (a) shows upscaled and rotated properties associated with reservoir zone 1, plot (b) zone 2, etc.

Chapter 11

Comparison of upscaled results with inverted seismic data

Now that reliable facies models have been upscaled with a technique that accurately takes into account their complex structure and geology, one holds what is believed to be representative channel belt properties at the seismic scale. Consequently, it will finally be possible to establish whether inverted seismic data contains information on the 3D geometry of reservoir rocks. This is basically done by comparing the upscaled channel belt properties with corresponding properties found in inverted seismic data. In order to demonstrate that the latter actually is capable of capturing 3D effects, the models and the inverted seismic data should ideally yield equivalent properties, i.e. velocities, at comparable locations. The initial idea was therefore to assemble a full scale reservoir model with the homogenized facies and do a direct comparison with the inverted seismic cube. For practical reasons, a simpler way of verifying the models has been chosen.

The main principle is to manually pick velocities from the inverted seismic cube where channel belts are present, and compare these with the effective ones obtained for the facies models. To make sure that the selected velocities represent channel belts and not background facies, they should only be taken from areas where the geology is known with high confidence. Naturally, this must be regions close to wells. Because most of the wells in the current reservoir come with interpreted channel belt logs, it is easy to distinguish channels from background in the nearby formations. Consequently, one can look through well logs to locate channels and pick representative velocities from the inverted seismic cube next to them. In order to allow a proper comparison between models and inverted seismic data, it is necessary to take note of the reservoir zones in which observations are made. As discussed in chapter 10, the channel belts are expected to vary significantly in properties from zone to zone. It is therefore essential that one compares facies models and seismic inverted data within zones and not within the reservoir as a whole.

In addition, one should always register the depth of each velocity pick. Since the depth trend in the seismic data may overshadow some of the important velocity characteristics,

it ought to be removed prior to the comparison. In the reservoir of interest, for example,
the depth trend associated with each zone is especially prominent due to compaction.
To eliminate it, a linear depth trend correction is applied to the data. The velocity cor-
rection, however, is not straightforward in this context. As the models are independent
of depth, it is hard to tell what should be the reference point of the correction. If one
settles on a very shallow depth, one might get too low velocities, while a deeper one can
give too high. Based on judgment, the reference depth is chosen to be the shallowest of
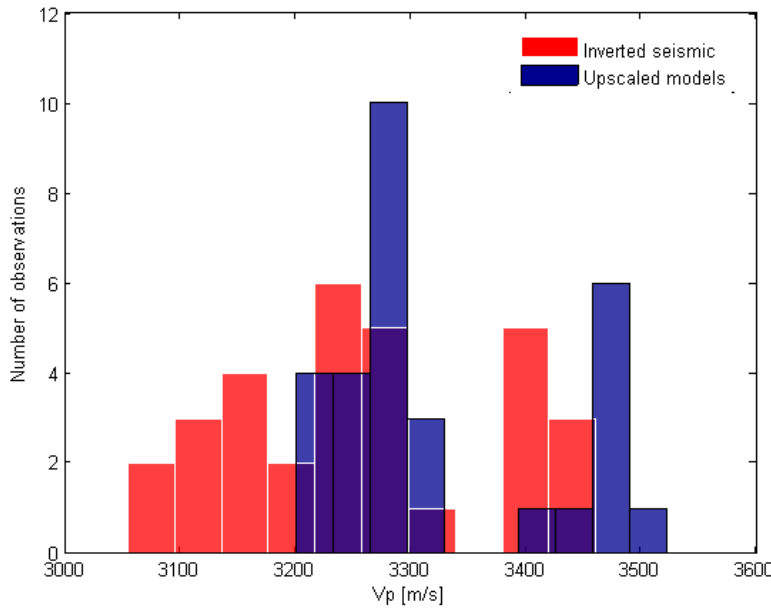the ones picked.

Figure 11.1: V_P-distributions associated with channel belt facies in reservoir zone 3.
The blue histogram belongs to the channel belt models, while the red belongs to the
seismic inverted data. The height of a rectangle reflects the number of observations
made in a particular bin.

Having gathered velocities from the inverted seismic cube, and corrected them for depth,
one certainly has a basis for validating models within each zone. By for example compar-
ing the distribution of effective V_P with the corresponding distribution provided by the
inverted seismic cube, it is possible to examine the fit between modeled and anticipated
channel belt properties. Particularly, one will be able to tell whether the models' P-wave
velocities fall inside the range stipulated by the inverted seismic data. Figure 11.1 shows
the two distributions of (vertical) channel belt V_P associated with zone 3. The blue and
red histograms represent observations made from the upscaled models and the seismic
inverted cube, respectively. Both sets of data are sorted into 10 equally spaced bins along
the x-axis between their distinctive minimum and maximum values. Bins are displayed

96

as rectangles such that the height of each rectangle indicates the number of observations in the bin. As one can notice from figure 11.1, the number of homogenized models in zone 3 is 30. This is consistent with what can be seen in figure 10.2c . The number of channel belt velocities picked out from the inverted data, on the other hand, is 31. These have been gathered nearby more than 20 different wells to take into account the lateral changes in channel belts. Due to the time frame given, the comparison in question is limited to zone 3 in this thesis. Since zone 3 is a complex zone, it has been carefully examined. Accordingly, the models associated with it are believed to be trustworthy.

As seen in figure 11.1, the predictive channel belt models produce seismic velocities that are very close to those found in the inverted seismic data. Quantitatively, the vertical V_P of the different facies models range from $3210m/s$ to $3522m/s$ with an average of $3325m/s$, while the ones selected from the inverted data range from $3055m/s$ to $3460m/s$ with an average of $3255m/s$. Consequently, the two distributions do not cover exactly the same velocity spread. Irrespective of this, they are undoubtedly similar and in line with each other. The most important feature that the histograms have in common is clearly the identical notch visible at approximately $3350m/s$. Apparently, there are two main groups of channel belt facies associated with zone 3. In agreement with figure 11.1, both the upscaled reservoir models and the inverted seismic data are able to capture their unequal qualities. Since the estimated channel belt velocities are assumed to be representative, this strongly suggests that the inverted seismic data is capable of capturing geological and geometrical information on facies and reservoir rocks. Accordingly, there is a good chance that facies can be differentiated on inverted seismic data using predictive modeling and elastic upscaling. The fit between the two distributions also proves what has been assumed in this chapter - namely that the channel belt models are realistic. In the future one should perhaps try to put an effort into making a full reservoir model of upscaled facies. A direct comparison with the inverted seismic cube will probably be even more accurate and intuitive. However, this will probably only reinforce the perception that inverted seismic data contains information on the 3D geometry of rocks.

Chapter 12

Conclusion

In order to enhance hydrocarbon recovery, one should continually strive to increase the detail level of the reservoir description. Since seismic surveys provide the only approved way of imaging the subsurface, it is crucial that one exploits their full potential. Accordingly, seismic data is combined with other sources of information, such as well logs, to produce quantitative estimates on the rock properties of the reservoir. From the inverted seismic data set, one would ideally like to distinguish sand from background and good sand from poor sand, so that wells can be placed optimally. The ultimate goal is therefore to be able to upscale elastic properties of predictive models and use them to differentiate various reservoir facies in the inverted seismic data. For this to be attainable, however, it is crucial that both the seismic data and the upscaling method capture the 3D geometry of reservoir rocks. Additionally, it is important that the facies models are reliable. The main objective of this thesis has therefore been to address all the necessary aspects of bringing predictive facies (3D) information to the seismic scale. This includes presenting and verifying the upscaling method, finding and validating model input, upscaling elastic properties, and comparing results with inverted seismic data. The study was carried out on numerous facies models that each describes a feasible channel belt in an actual, mature reservoir.

Up until now, it has not been possible to accurately upscale elastic properties in compositions with complex geometries and symmetries. Without exceptions, the former methods (e.g. Backus, Voigt and Reuss averages) take only limited or no geological information into account. This basically means that the numerical method provided by the OPM project is the first of its kind to upscale three-dimensional elastic information in a consistent manner. Whereas elastic properties depend on geological features at all scales, the latter implementation must be regarded as a substantial contribution to the discipline of reservoir modeling. Owing to the fact that the general upscaling method is relatively new and untried, it had to be thoroughly examined and tested before put into use. Consequently, several test models with different characteristics and grid size were upscaled, and their results evaluated. The output associated with the simplest models could be quantitatively compared with exact, analytical solutions provided by

Backus averaging, while the ones belonging to more complex models had to be assessed by Voigt and Reuss bounds. Since the latter two constrain the true effective modulus of any model, it was possible to roughly determine the code's response to complex geology even without a solution on hand. Neither of the test cases, simple or complex, turned out to give alarming results. Accordingly, the general upscaling method can be assumed both functional and accurate for all kinds of models, including large and intricate ones of facies. As the upscaling code is computationally heavy, the run-time, however, can sometimes pose problems if the number and size of grids to upscale are large. To reduce the total duration, it was shown that a model can be chopped into smaller pieces. By separately upscaling the submodels and averaging their effective properties, a fairly decent substitute for the full model elastic tensor can be obtained in a much shorter time. The accuracy (usability) of the method depends on the size of the partitions, the material properties and the geometry of the complete model. Hence, it should only be used as a last resort when time actually is an issue. To save additional time, one should always make sure that the upscaling method's default linear solver is set, as this was proven to operate the fastest on larger grids.

For the various facies models to be predictive of the reservoir's in situ channel belts, they obviously had to be populated with reliable elastic cell properties. In agreement with the modeling workflow, the cells of each facies model corresponded to upscaled lithofacies, connected to effective porosities and clay volumes among other properties. However, as it was previously impossible to upscale elastic information, physical parameters on elasticity lacked. Of this reason, three acknowledged empirical velocity-porosity-clay relations (and one density-porosity relation) were introduced as possible tools to generate consistent isotropic properties. To check their usability, synthetic velocity logs were created and compared with sonic well measurements. From this, it was found that all three relations fail to predict velocities in background material, but generally succeed in reservoir sand. Consequently, if one ever needs representative sandstone properties, the velocity models of Han [16], Tosaya/Nur [17] and Castagna [18] are obviously applicable. Since the latter relation stood out as the most suitable one for the reservoir of interest, it was given the task of linking velocities to the various sand-associated lithofacies. Combined with reliable empirical densities obtained from Han's measurements on sedimentary rocks, these provided the elastic properties of the model sands. As the available relations proved to overestimate non-sandy rock velocities, each individual cell associated with background material had to be populated with well data instead. This was carried out by randomly picking triplets of V_P, V_S and density from a distribution consisting of only non-sandy well log measurements. Although Castagna's model and the said distribution are believed to give adequately realistic input, there is always room for improvement. For example, one may want to "place" facies models in depth, so that pore fluid and compaction features can be accounted for. In future reservoir modeling, however, one will hopefully not have to determine elastic properties in the same manner. With the general upscaling method on hand, elastic information should be passed from the pore scale and up, to increase model accuracy.

After having verified that the upscaling method behaves correctly, and that the elastic input is trustworthy, the different facies models were upscaled to provide prognostic channel belt properties at the seismic scale. Since the resulting effective tensors are supposed to be descriptive of the reservoir's elastic behavior, they are expected to contain valid information about the seismic anisotropy. To best examine the significance of the latter quality, V_P and V_S were found for three different measuring angles. The results showed that velocities have a small but considerable degree of directionality. In principle, this means that deviated well logs should be corrected for angle before they are utilized in seismic inversion. Future inversion methods would consequently benefit greatly from having an implementation that applies orthogonal tensor rotation to wells. As this theoretically will allow them to cope with deviated data, large quantities of information that previously had to be put aside are suddenly unlocked. With more knowledge available, the description of the reservoir would most definitely improve.

The main reasons for upscaling the channel belt models, however, were to examine their representativeness and to find out whether seismic inverted data can be predicted with elastic 3D modeling. To do this, the facies models' effective P-wave velocities had to be compared with corresponding channel belt velocities observed on inverted seismic data. Since the anticipated and the measured properties turned out to match relatively well, the models are assumed reliable - at least on the seismic scale. If one considers the facts that the general upscaling method is accurate and the models are realistic, simple reasoning suggests that inverted seismic data is able to capture information on the 3D geometry of rocks. The facies models appear nevertheless to be predictive of the channel belt properties seen on inverted seismic data.

Future research on this topic should include a similar study on background facies. By comparing modeled background properties with equivalent measured ones observed on inverted seismic data, one will be able to tell whether background material can be predicted or not. If it can, and the velocity distribution of the background facies is somewhat shifted relative to that of the channel belts, one will have a way of separating the latter two on inverted seismic data. To tell by likelihood which facies an inverted velocity is associated with, one should simply consult the distributions. Ideally, this will allow one to pinpoint good reservoir sands, so that much fewer wells have to be drilled. In addition, if it is valid, the process can be applied to other reservoirs. A variety of predictive facies models must then be generated and upscaled to provide representative background and sand distributions that inverted seismic data can be compared with.

Bibliography

[1] A. B. Lindblad, *Elastic Tensors and Homogenization.* Norwegian University of Science and Technology, 2012

[2] B.A. Auld, *Acoustic Fields and Waves in Solids.* John Wiley and Sons, Vol. 1, 1973.

[3] R. E. Sheriff and L. P. Geldart, *Exploration Seismology.* Cambridge University Press, 2nd edition, 1995.

[4] Wai-Fah Chen and Da-Jian Han, *Plasticity for Structural Engineers.* J. Ross Publishing, 2007.

[5] U. Briegel and W. Xiao, *Paradoxes in Geology.* Elsevier Science B.V., 2001.

[6] G. Dresen, A. Zang and O. Stephansson, *Rock Damage and Fluid Transport.* Birkhäuser Verlag, Part 1, 2006.

[7] G. E. Backus, *Long-wave Elastic Anisotropy Produced by Horizontal Layering.* Journal of Geophysical Research, Vol. 62, 1962.

[8] K. Børset, *Multiscale Modelling of Elastic Parameters.* Norwegian University of Science and Technology, 2008.

[9] P. Avseth, T, Mukerji and G. Mavko, *Quantitative Seismic Interpretation: Applying Rock Physics Tools to Reduce Interpretation Risk.* Cambridge University Press, 2005.

[10] L. V. Gibiansky, *Bounds on the Effective Moduli of Composite Materials.* Princeton University, 1993.

[11] L. Thomsen, *Weak Elastic Anisotropy.* Geophysics, Vol. 51, 1986.

[12] M. Duarte, C. Piedrahita, T. Salinas, H. Altamar and K. Pachano, *Slowness Surface Calculation for Different Media Using the Symbolic Mathematics Language Maple.* Instituto Colombiano de Petróleos, 2004.

[13] W. Zijl, M. A. N. Hendriks and C. M. P. 't Hart, *Numerical Homogenization of the Rigidity Tensor in Hooke's Law Using the Node-Based Finitie Element Method.* Mathematical Geology, 2002.

[14] R. B. Latimer, R. Davison and P. van Riel, *An Interpreter's Guide to Understanding and Working with Seismic-Derived Acoustic Impedance Data.* The Leading Edge, 2000.

[15] Henry Petroski, *Invention by Design: How Engineers Get from Thought to Thing.* Harvard University Press, 1996.

[16] De-hua Han, A. Nur and D. Morgan, *Effects of Porosity and Clay Content on Wave Velocities in Sandstones.* Geophysics, Vol. 51, 1986.

[17] C. Tosaya and A. Nur, *Effects of Diagenesis and Clays on Compressional Velocities in Rocks.* Geophysical Research Letters, Vol. 9, 1982.

[18] J. P. Castagna, M. L. Batzle and R. L. Eastwood, *Relationships Between Compressional-wave and Shear-wave Velocities in Clastic Silicate Rocks.* Geophysics, Vol. 50, 1985.

[19] W. S. Phillips, J. T. Rutledge, L. S. House and M. C. Fehler, *Induced Microearthquake Patterns in Hydrocarbon and Geothermal Reservoirs: A Review.* Pure Appl. Geophysics, 2001.

[20] M. L. Batzle and Z. Wang, *Seismic Properties of Pore fluids.* Geophysics, Vol. 64, 1992.

[21] R. Hill, *The Elastic Behavior of a Crystalline Aggregate.* Proceedings of the Physical Society, Section A, Vol. 65, 1952.

[22] D. Han og M. L. Batzle, *Gassmann's Equation and Fluid-Saturation Effects on Seismic Velocities.* Geophysics, Vol. 69, 2004.

[23] R. Simm, *Practical Gassmann Fluid Substitution in Sand/Shale Sequences.* First Break, Vol. 25, 2007.

[24] D. Kumar, *A Tutorial on Gassmann Fluid Substitution: Formulation, Algorithm and Matlab Code.* Geohorizons, 2006.

[25] Wikipedia: Hooke's Law. http://en.wikipedia.org/wiki/Hooke's_law#cite_note-2.

[26] Wikipedia: Elastic Modulus. http://en.wikipedia.org/wiki/Elastic_modulus.

[27] OPM at GitHub: https://github.com/OPM

[28] The open porous media interactive: Dune elasticity upscale. http://www.opm-project.org/wiki/index.php/Dune-elasticity-upscale